Local Topographic and Electronic Structure of Mixed Surface Alloys: Anderson Localization of Electronic States

Dissertation zur Erlangung des akademischen Grades
eines Doktors der Naturwissenschaften (Dr.rer.nat.)

vorgelegt von
Fabian Zinser

an der

Universität
Konstanz

Fachbereich Physik

Konstanz, 2012

Zusammenfassung

Diese Arbeit befasst sich mit der Untersuchung der atomaren und elektronischen Struktur von gemischten Oberflächenlegierungen mittels eines Rastertunnelmikroskops mit variabler Temperatur. Die in dieser Arbeit untersuchte Klasse von Oberflächenlegierungen entstehen durch die Substitution von jedem dritten Atom einer Ag(111) Oberfläche durch die Elemente Bi, Pb oder Sb. Während die reinen Oberflächenlegierungen nur ein einzelnen Substituenten beinhalten, können in gemischte Oberflächenlegierungen verschiedene Substituenten in beliebigem Mischungverhältnis vorkommen.

In den gemischten Oberflächenlegierungen kann durch Vergleich der topographischen und den dazugehörigen elektronischen Strukturen erstmals die Lokalisierung von elektronsichen Zuständen aufgrund atomarer Unordnung (Anderson-Lokalisierung) lokal aufgelöst gezeigt werden. Mit Hilfe eines Tight-Binding Modells für ungeordnete Gitterstrukturen werden die experimentellen Messungen in Simulationen direkt reproduziert.

Die topographischen Untersuchungen der gemischten Oberflächenlegierungen zeigen, dass die je nach Element unterschiedliche Relaxation der einzelnen Substituenten auch im gemischten Fall erhalten bleibt, und so eine Analyse der chemischen Zusammensetzung der Oberfläche mit atomarer Auflösung ermöglicht. Die statistische Verteilung der einzelnen Substituenten in den gemischten Oberflächenlegierungen ist ungeordnet, aber nicht ganz zufällig. Eine kleine, attraktive effektive Paarwechselwirkung zwischen substitutionellen Atomen des selben Elements wird durch den Vergleich mit Monte-Carlo Simulationen gezeigt.

Für die Entstehung der Monolagenphase im Falle eines Überschusses an Substituenten kann ein deutlicher Unterschied im Verhalten zwischen den untersuchten Oberflächenlegierungen gezeigt werden. Für das Wachstum der reinen Oberflächenlegierung Bi/Ag auf einem dünnen, heteroepitaktischen Ag/Pt(111) Film, kann wird gezeigt, dass die Anwesenheit des Bismuths das Wachstum des Ag/Pt(111) Films stark beinflusst.

Die Auswahl an reinen Oberflächenlegierungen mit individuellen elektronischen Eigenschaften, die in beliebigem Verhältnis in den gemischten Oberflächenlegierungen kombiniert werden können, ermöglicht es die experimentelle Untersuchung der Anderson-Lokalisierung von elektronischen Zuständen auf einen weiten Raum von Parametern auszudehnen und den Einfluss unterschiedlicher Effekte wie zum Beispiel Spin-Bahn Wechselwirkung zu studieren.

Abstract

In this work, the atomic and electronic structure of mixed surface alloys is studied using a scanning tunneling microscope with variable temperature. The examined class of surface alloys is formed by substitution of every third atom of a Ag(111) surface with the elements Bi, Pb or Sb. While the pure surface alloys consist of only one substituent, mixed surface alloys consist of several substituents with an arbitrary ratio.

For the mixed surface alloys it is possible for the first time to demonstrate the localization of electronic states due to atomic disorder (Anderson localization) on a local scale by comparing topographic and corresponding electronic structures. Using a tight-binding model for disordered lattice structures, the experimental results can be directly reproduced in simulations.

The topographic studies of the mixed surface alloys reveal that the particular substituents retain their individual relaxation even when different substituents are mixed, and so an analysis of the chemical composition of the surface with atomic resolution is possible. The statistical distribution of the particular substituents in the mixed surface alloys is disordered but not fully random. A small, attractive effective pair interaction between substitutional atoms of the same element is demonstrated by a comparison with Monte-Carlo simulations.

A distinct difference in the behavior of the examined mixed surface alloys can be demonstrated for the development of the monolayer phase in the case of an excess of substituents. It can be shown for the growth of the pure surface alloy Bi/Ag on a thin, heteroepitaxial Ag/Pt(111) film, that the presence of bismuth strongly influences the growth of the Ag/Pt(111) film.

The variety of pure surface alloys with individual electronic properties, which can be combined with arbitrary ratio into mixed surface alloys, makes it possible to extend experimental studies of the Anderson localization of electronic states to a wide range of parameters and to examine the influence of of different effects, such as spin-orbit interaction.

Contents

Chapter 1

Introduction

With the discovery of bronze about 5000 years ago, alloys are one of the oldest technological discoveries of mankind and in the modern times, alloys play an important role for the technological advancement in science and engineering . Alloying allows to create materials with new and specific properties, ranging from the increased hardness of steel to the tailored electronic properties of semiconductors to the enhanced Rashba effect in surface alloys.

Many alloys exhibit a disordered atomic distribution of their components. These disordered structures do not exhibit translation invariance, making it impossible to describe these alloys using simple pictures such as Bloch waves, which are normally used to describe the properties of solids and are taught in basic physic courses. For the theoretical description of these alloys, averaging methods like the virtual crystal approximation [1] or the coherent potential approximation [2] are used to restore the translational invariance. However, these descriptions overlook properties of the alloys that are related to the disorder.

In 1958, P. W. Anderson theoretically described the influence of disorder on the diffusion of spin or charge carriers [3]. The limited diffusion described by his model is nowadays known as Anderson localization. It took more than 30 years until disorder localization of waves could be experimentally observed [4]. To date, disorder localization has been found for a variety of waves such as acoustic waves [4,5], electromagnetic waves [6–8] and matter waves [9–11]. Localization of electronic waves has been studied indirectly in transport measurements in the form of a metal-insulator transition in doped semiconductors, but a clear distinction between Mott localization due to electron-electron interaction and Anderson localization was not possible for these materials [12]. Only recently, this transition could be attributed to disorder in the phase-change material $GeSb_2Te_4$ [13].

Until now, there are no direct observations of electronic wavefunctions localized due to disorder. The ideal tool for such a study is the scanning tunneling microscope. Scanning tunneling microscopy allows to study surface topographies with atomic [14] and even chemical resolution [15–17]. Simultaneously, it allows to study the electronic structure of surfaces on the same length scale [18].

A material system ideal for the study of a disordered atomic structure and the correlated electronic states are the pseudobinary mixed surface alloys such as $\mathrm{Bi}_x\mathrm{Pb}_{1-x}$/Ag(111) [19] and $\mathrm{Bi}_x\mathrm{Sb}_{1-x}$/Ag(111) [20]. Surface alloys are made of elements that are immiscible in the bulk, but are miscible in the surface layer, forming a two dimensional alloy. Surface alloys such as Bi/Ag(111) [21] have sparked great interest in the past years, as they exhibit states confined mostly in the surface layer which show a giant Rashba-type spin-splitting [22]. The pseudobinary nature of the mixed surface alloy allows the continuous tuning of their electronic properties. The limitation of the atomic as well as the electronic structure to the surface makes the mixed surface alloys a perfect material system for studies with surface sensitive techniques such as scanning tunneling microscopy and spectroscopy, and allows a direct correlation of the topographic and electronic structures.

This thesis is structured in the following way: The basic principles of scanning tunneling microscopy and spectroscopy, the experimental techniques applied in this work, are described in chapter 2. In chapter 3, the scientific background of the examined material system, surface alloys with Rashba-type spin-splitting, the Anderson model for localization of waves and Monte-Carlo simulations of alloys are explained in detail. Chapter 4 describes technical details of the UHV-system with the variable temperature STM as well as the preparation of the samples and the STM tip. The remaining chapters deal with the experimental results and the discussion of these results. Chapter 5 covers the growth and topographic structure of the mixed surface alloys and compares this with results of Monte-Carlo simulations. In Chapter 6 the local electronic structure of the mixed surface alloys is examined and, using the Anderson model of localization, the correlation between the disordered atomic structure and the local variations of the electronic structure is demonstrated. In chapter 7, the growth and influence of the Bi/Ag surface alloy on a thin, heteroepitaxial Ag/Pt(111) film and dealloying of the mixed surface alloys are studied.

Chapter 2

Scanning Tunneling Microscopy and Spectroscopy

2.1 Basic Principle of STM

Scanning tunneling microscopy (STM) is an experimental technique for spatially localized measurements of topographic [14] and electronic properties [18] of metal and semiconductor surfaces, exploiting the purely quantum mechanical principle of electron tunneling. The basic principle of STM is illustrated in Fig. 2.1. For electron tunneling to occur, a metallic tip is brought into close range (of the order of a few Å) of the surface of interest. While there is no direct electric contact, the electron wave functions decay exponentially into the region between tip and sample and overlap there at small enough distances, allowing a transition from the state of one side into the state of the other side. In the case of a potential difference due to an applied bias voltage between the two sides, electrons can tunnel from the higher energy side into the empty states of the other side. This is illustrated in Fig. 2.2. The exponential decay of the wave functions leads to an exponential dependance of the tunneling probability and the resulting tunneling current on the distance between tip and sample surface. This allows to measure changes in this distance with a high resolution ($\sim 1\,\mathrm{pm}$). In the case of an ideal tip terminated by a single atom, most of the tunneling current will go through this atom as all other tip atoms are further away from the surface, resulting in a high spatial resolution.

Images of the surface topography can be acquired by scanning the tip over the sample surface while measuring changes in the tunneling current. There are to different operating modes for scanning: The ”constant hight” mode is simpler one, for which the tip is kept

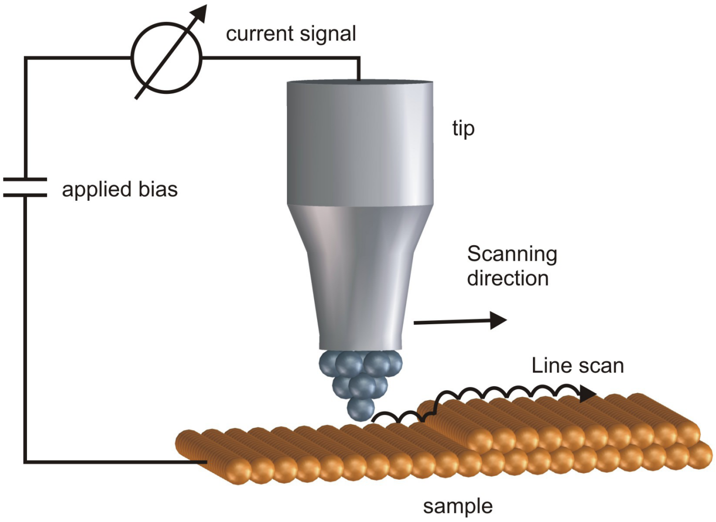

Figure 2.1: Illustration of the basic principle of scanning tunneling microscopy. A metallic tip is brought into close contact of a conducting surface until a tunneling current is detected. Scanning the tip over the surface, while recording the variations in the current signal, gives a representation of the topography of the surface.

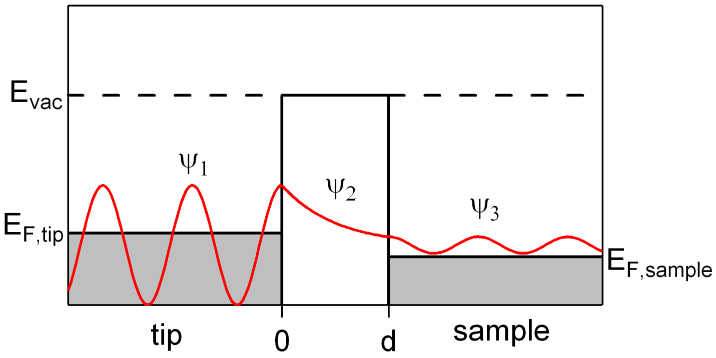

Figure 2.2: Illustrations of electron wave functions before (ψ_1), during (ψ_2) and after (ψ_3) tunneling through the vacuum barrier between tip and sample. In the energetically allowed regions of the tip and the sample, the wave functions have a sinus form, while in the forbidden region of the vacuum barrier the wave function decays exponentially. The different amplitudes of ψ_1 and ψ_3 can be explained with finite probability of ψ_1 being reflected at the vacuum barrier.

at constant height (z-position relative to the base of the tip positioning system, not to the sample surface) and changes in the current correspond directly to changes in the surface height. This mode is simpler to implement and allows faster scanning, but requires flat surfaces to avoid contact between tip and sample or loosing the tunneling contact. The second mode is the ”constant current” mode which is normally used. A closed feedback loop measuring the tunneling current is used to adjust the z-position of the tip so that the tunneling current is kept at a preset value. The z-position of the tip is then directly used as height for the topography.

Scanning tunneling spectroscopy (STS) measurements of the surface electronic structure can be performed by keeping the tip at a lateral and vertical fixed position (feedback loop is open), while measuring the conductance for a bias voltage ramp. As these spectroscopic measurements are spatially localized, measuring at different positions on the sample surface allows to identify local variations in the electronic structure.

2.2 Theory of Scanning Tunneling Microscopy

2.2.1 Bardeen Theory of Tunneling

Bardeen developed his theory of electron tunneling [23] to explain the experimental findings of Giaever [24] as well as Nicol *et al.* [25] for superconductor-insulator-superconductor tunneling experiments. The derivation starts with two electrodes A and B far away from each other, with potentials U_A and U_B and stationary wave functions ψ_μ and χ_ν respectively. Bringing the two electrodes close to each other, the wave function ψ_μ has now a probability to transfer from the region A into states given by the wave function χ_ν in region B and the time dependent solution can be described by linear combination of the initial state ψ_μ and the possible final states χ_ν

$$\Psi = \psi_\mu e^{-\frac{i}{\hbar}E_\mu t} + \sum_{\nu=1}^{\infty} c_\nu(t)\chi_\nu e^{-\frac{i}{\hbar}E_\nu t} \tag{2.1}$$

With the tunneling matrix element $M_{\mu\nu}$ the probability for a transition is given by

$$p_{\mu\nu} = |c_\nu(t)^2| = |M_{\mu\nu}|^2 \frac{4\sin^2[\frac{1}{2\hbar}(E_\mu - E_\nu)t]}{(E_\mu - E_\nu)^2} \tag{2.2}$$

The behavior of the fraction on the right side is plotted in Fig. 2.3 as a function of the

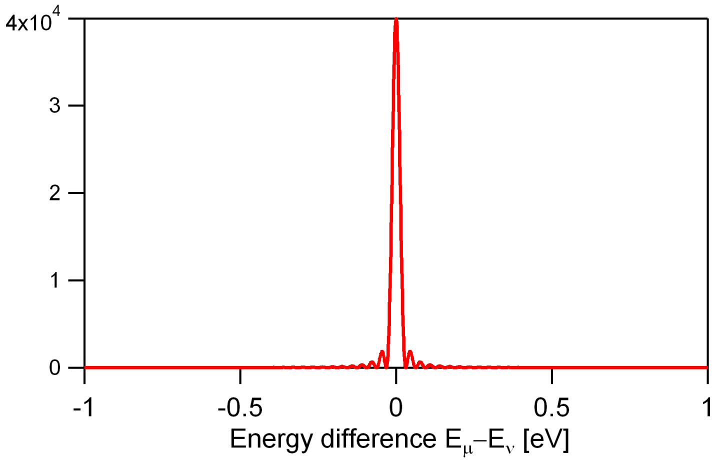

Figure 2.3: Graph of the fraction on the right side of Eq. 2.2 as a function of the energy difference $E_\mu - E_\nu$ with $\frac{t}{2\hbar} = 100\,\mathrm{eV}^{-1}$. The function has its maximum at $E_\mu = E_\nu$ and drops quickly to 0 if $E_\mu \neq E_\nu$ implying the preference of elastic tunneling.

energy difference $E_\mu - E_\nu$. The fraction has its maximum for $E_\mu = E_\nu$ and drops quickly to 0 for $E_\mu \neq E_\nu$, implying that the initial and the final state of the tunneling process have the same energy. The process is then called elastic tunneling. In contrast to this is the case when the electron loses energy during the tunneling process due to some interaction (e.g. a spin flip in the presence of a magnetic field). This process is then called inelastic tunneling and will not be treated here any further.

To calculate the tunneling current, one has to take the density of states $\rho(E)$ of both electrodes into account. For elastic tunneling, the number of states an electron in electrode A at some energy E can tunnel into (if they are empty) is given by the density of states $\rho_B(E)$ of the electrode B. On the other hand, the number of such electrons is given by $\rho_A(E)$. In the case of an applied bias voltage V, electrons in the energy interval $[E_F, E_F + eV]$ can tunnel into the empty states above E_F in the other electrode. With the approximation of a constant density of states near the Fermi energy, the tunneling current I for small voltages V is given by

$$I = \frac{2\pi e^2}{\hbar} |M_{\mu\nu}|^2 \rho_B(E_F) \rho_A(E_F) V \tag{2.3}$$

For a more general result, the temperature has to be taken into account. The effects of a finite temperature T on the occupation of states is given by the Fermi-Dirac statistic

$$f(E,T) = \frac{1}{e^{\frac{1}{k_B T}(E-E_F)} + 1} \tag{2.4}$$

Dropping also the assumption of a constant density of states $\rho(E)$, this gives the following result for the tunneling current:

$$I = \frac{2\pi e}{\hbar} \int\limits_{-\infty}^{+\infty} \left(f(E-eV,T) - f(E,T)\right) |M_{\mu\nu}(E,d)|^2 \rho_A(E)\rho_B(E)dE \tag{2.5}$$

The tunneling matrix element $M_{\mu\nu}$ can be calculated from the overlap of the two wave functions ψ_μ and χ_ν at an arbitrary surface in between the two electrodes

$$M_{\mu\nu} = \frac{\hbar^2}{2m} \int \psi_\mu \frac{\partial \chi_\nu^*}{\partial z} - \chi_\nu^* \frac{\partial \psi_\mu}{\partial z} dxdy \tag{2.6}$$

The dependence of the matrix element on the Energy E and the distance d between the electrodes from the exponential decay of the wave functions inside the barrier is given by

$$\psi_\mu(z) = \psi_\mu(0)e^{-\kappa_\mu z} \tag{2.7}$$

$$\chi_\nu(z) = \chi_\nu(0)e^{-\kappa_\nu (d-z)} \tag{2.8}$$

In the case of elastic tunneling the the decay constants κ_μ and κ_ν are identical and can be written as

$$\kappa = \frac{1}{\hbar}\sqrt{2m(\overline{\Phi} - E)} \tag{2.9}$$

with $\overline{\Phi}$ as the average height of the barrier given by the work functions of the two electrodes.

2.2.2 Tersoff-Hamann Model

For the calculation of the tunneling current in Eq. 2.3 with the tunneling matrix element of Eq. 2.6, knowledge of the tip and sample wave functions is necessary. However, the structure of the tip and its wave functions are generally not known, and have to be approximated with a model. A very prominent model was developed by Tersoff and Hamann [26]. In their model, the tip is approximated as a spherical apex with radius R and its center at $\vec{r}_0 = (0, 0, z_0)$ above the surface. Outside the tip in the vacuum region, the spherical tip state is given by

$$\chi(\vec{r}) \propto \frac{1}{|\vec{r}-\vec{r}_0|} e^{\kappa|\vec{r}-\vec{r}_0|} \tag{2.10}$$

In general, the sample wave function can be described by a Fourier expansion in the direction parallel to the surface. In the vacuum region, this is gives

$$\psi(\vec{r}) \propto \int a(\vec{q}) e^{-\sqrt{\vec{q}^2+\kappa^2}z+i\vec{q}\vec{x}} d^2\vec{q} \tag{2.11}$$

with $\vec{x}$ and $\vec{q}$ as the in-plane position vector and momentum vector respectively. The electronic structure of the surface is defined by the expansion coefficients $a(\vec{q})$. Using this wave function and the Fourier transformation of the tip wave function (Eq. 2.10) to calculate the tunneling matrix element Eq. 2.6, one finds $M \propto \psi(\vec{r}_0)$. With Eq. 2.3 and only one tip state, this leads to a tunneling current

$$I \propto |\psi(\vec{r}_0)|^2 \rho_S(E_F) V \propto \rho_S(E_F, \vec{r}_0) V \tag{2.12}$$

This means, that for small voltages the conductance $\frac{I}{V}$ is proportional to the density of states of the sample at the position of the tip. So, in STM, it is not really the atomic structure that is measured, but the LDOS ρ generated by the atomic structure. A limitation of the Tersoff-Hamann model is that the s-wave approximation is only true for surface features with a size much larger then approximately 0.3 nm. If there are smaller features, other tip states with higher angular momentum cannot be neglected anymore for the tunneling matrix element. Especially for atomic resolution on metal surfaces, states like the p_z or d_{z^2} state have to be taken into account.

2.3 Chemical Resolution on Alloy Surfaces

Even though chemical contrast of alloy surfaces is not an intrinsic feature of a STM, such contrast was achieved on a variety of alloys [17] and surfaces alloys [15, 16]. In binary alloys, the chemical contrast manifests itself in two different corrugations of the surface atoms. The difference can arise from several effects: When one element is larger then the other or relaxes out of the surface plane, there is a real height difference between the atoms of different elements (Fig. 2.4 a)). An example for such a contrast are surface alloys like Pb/Cu(111) [15] or Bi/Ag(111) [27], for which the larger Pb and Bi atoms were found as protursions. On the other hand, the tunneling current depends on the local density

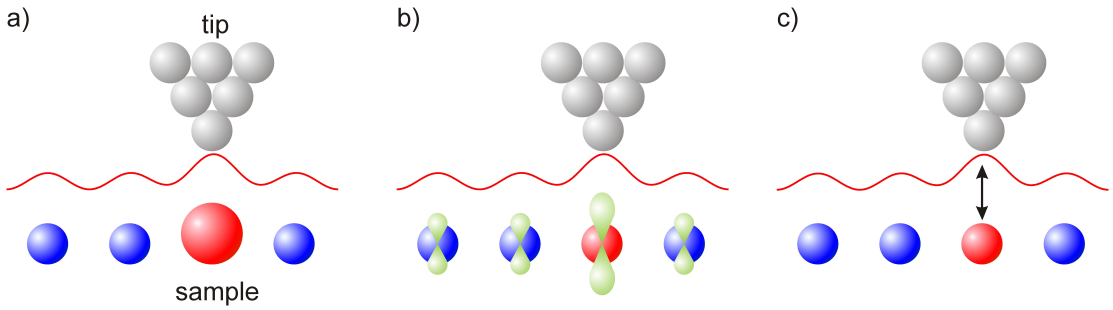

Figure 2.4: Different effects leading to chemical contrast in STM measurements: a) Height and/or size difference, b) difference in the LDOS and c) difference in the interaction between tip and surface atoms.

of states of the sample near the Fermi energy as it was demonstrated in section 2.2, so different LDOS of the alloy atoms lead to an apparent height difference as illustrated in Fig. 2.4 b). An example for this are alloys of a noble metal and and a transition metal with its partially filled *d* shell like the PdAg alloy [28]. In contrast to the *sp*-band of the noble metal, the *d*-band is localized around the Fermi energy, giving rise to a high LDOS at this energy range. Finally, different interactions between the tip (or an adatom on the tip) and the surface atoms [29] can also lead to a different apparent height (Fig. 2.4 c)). The combination of these effects can make it difficult to correctly assign the different corrugation to the respective elements. For example in the Au/Ni(110) surface alloy, the Au atoms appear as shallow holes in the Ni surface, even though the Au atoms are larger and sit slightly higher then the Ni atoms [30]. In such cases the surface concentration of the alloy elements must be known (from the sample preparation or e.g. XPS measurements) to assign the different atoms correctly.

2.4 dI/dV-Spectroscopy

In the simplified picture of the Tersoff-Hamann model given by Eq. 2.12, one can see that the local density of states of the sample $\rho_S(E, \vec{r}_0)$ is directly accessible by measuring the derivative of the tunneling current at the energy $E = E_F + eV$

$$\left(\frac{dI}{dU}\right)_{U=V} \propto \rho_S(E_F + eV, \vec{r}_0) \tag{2.13}$$

However, the density of states of the tip $\rho_T(E)$ and the tunneling matrix element $M(E)$ are usually not constant and have to be taken into account using the Bardeen formalism. The

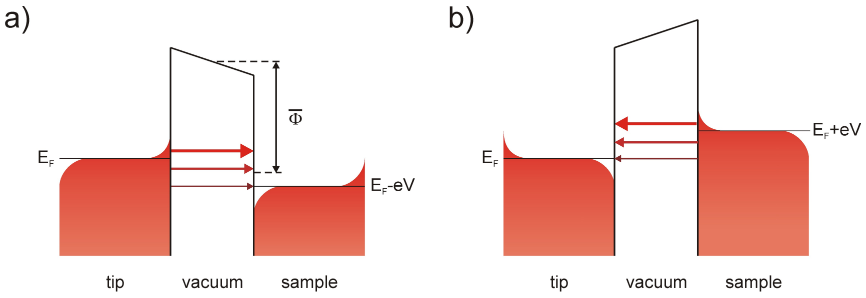

Figure 2.5: Asymmetry in the tunneling spectrum for the bias voltage applied to the sample. a) Tunneling from the tip into the occupied states of the sample for negative bias voltage. b) Tunneling from the unoccupied states of the sample into the tip for positive bias voltage. The width of the arrows represents the increased tunneling probability for states with higher energy

energy dependence of $M(E)$, given by the decay constant Eq. 2.9, can be approximated for $E \ll \overline{\Phi}$ (which is usually the case in STS measurements), using $\sqrt{1-\frac{E}{\overline{\Phi}}} \approx 1 - \frac{1}{2}\frac{E}{\overline{\Phi}}$:

$$M(E) = M(0)e^{\kappa_0 \frac{E}{2\overline{\Phi}} d} \tag{2.14}$$

with $\kappa_0 = \frac{1}{\hbar}\sqrt{2m\overline{\Phi}}$. This simply states the fact, that states with higher energy see a lower vacuum barrier for the tunneling process and thus have a higher probability to tunnel through the barrier to the other side (see Fig. 2.5). This means that mainly the unoccupied states of the tip and the sample can be probed by STS while for the occupied states, one is limited to energies near the Fermi energy [31, 32].

To perform a dI/dV measurement, the tip is positioned at the location of interest and stabilized at a certain feedback setpoint for the tunneling current. The feedback loop is opened and the bias voltage is ramped through the voltage range (i.e. energy range) of interest, while the tunneling current is recorded. Usually dI/dV measurements are performed by using a Lock-In amplifier, adding a small modulation voltage $V_{mod}\cos(\omega t)$ to the bias voltage V which has two advantages. First it increases the signal-to-noise ratio as the amplifier filters out any signal which is not modulated with a frequency ω and second, one can directly measures the signal of the first or higher derivatives: Expanding the modulated current signal $I(V + V_{mod}\cos(\omega t))$ into a Taylor series at voltage V gives

$$I(V + V_{mod}\cos(\omega t)) \approx I(V) + \frac{dI}{dV}V_{mod}\cos(\omega t) + \frac{1}{2}\frac{d^2I}{dV^2}V_{mod}^2\cos^2(\omega t) + \dots \tag{2.15}$$

One can see, that by detecting only the signal that varies with frequency ω, one gets

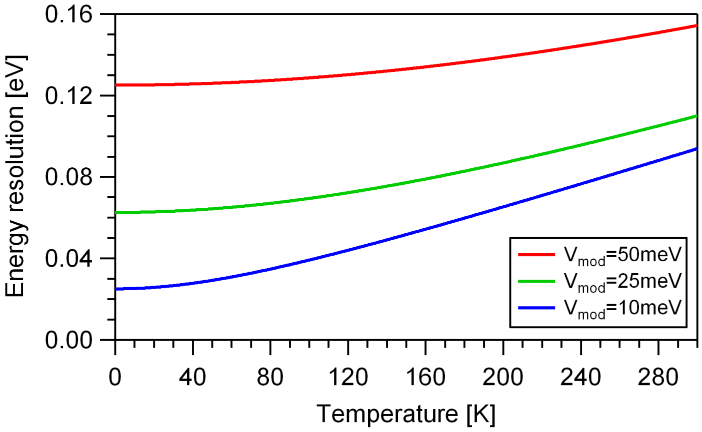

Figure 2.6: Lower limit of energy resolution in dI/dV measurements as function of temperature T for different Lock-In modulation voltages V_{mod}.

directly the first derivative $\frac{dI}{dV}$, while the equality $\cos^2(\omega t) = \frac{1}{2} + \frac{1}{2}\cos(2\omega t)$ shows, that the second derivative can be measured by using only the signal of the second harmonic.

Limiting factors for the energy resolution ΔE in STS measurements are the temperature T and the Lock-In modulation V_{mod} given by [33]

$$\Delta E = \sqrt{\Delta E_{therm}^2 + \Delta E_{mod}^2} \approx \sqrt{(3.5k_BT)^2 + (2.5eV_{mod})^2} \tag{2.16}$$

The temperature is a technical limitation of the measurement system design and the exact limitation can have a variety reasons like heat transport through cables or simply the limit of temperature that can be reached with the respective coolant (for example 4.2 K for liquid He^4 without pumping the coolant). In the case of a flow cryostat as it is used here, there is the trade-off between temperature and the mechanical noise induced by the circulating coolant. On the other hand, the Lock-In modulation is limited by the desired signal-to-noise ratio, which drops with decreasing V_{mod}. The energy resolution ΔE as function of temperature is plotted for different modulation voltages in Fig. 2.6.

Chapter 3

Scientific background

3.1 General properties of alloys

3.1.1 Ordering in binary alloys

The simplest form of alloys are substitutional solid solutions. Here, in a crystal of element A, some atoms are replaced by a second element B without changing the lattice structure. Which lattice sites the substitutional atoms occupy is a statistical process and depends on the interaction between the atoms that form the alloy. Ordering in such an alloy can be described by the short range order parameters $\alpha(i)$ introduced by Cowley [34]

$$\alpha_A(i) = 1 - \frac{x_B(i)}{x_B n_i} \tag{3.1}$$

for a central atom of the element A, with $x_B(i)$ the average ratio of B atoms in the ith neighbor shell ($i = 1$ for the nearest neighbors, $i = 2$ for the next nearest neighbors), x_B the overall ratio of B atoms and n_i the number of lattice sites in the ith neighbor shell. An order parameter larger (smaller) than 0 represents a preference for atoms of the same (different) kind in the respective neighbor shell, while an order parameter of 0 implies no preference and the occupation of that shell is given on average by the overall ratio.

In Fig. 3.1 different types of possible ordering for a $A_{0.33}B_{0.67}$ alloy, random distribution, long range ordering in form of a periodic structure and short range order in form of segregation are illustrated. The corresponding order parameters up to the 50th neighbor order are displayed in Fig. 3.2. For a truly random distribution, order parameter α_i is 0 for all neighbor orders i. For short range order in form of segregation, α_i becomes small

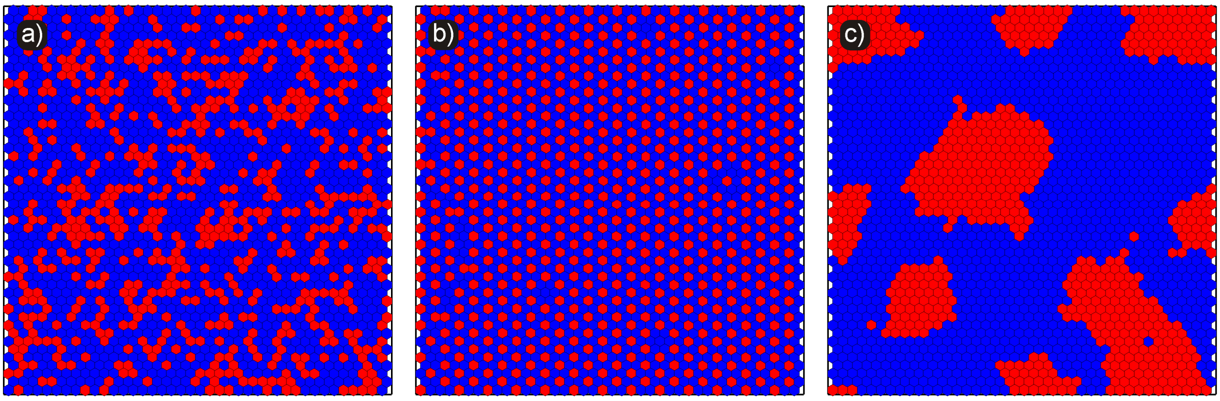

Figure 3.1: Illustration of different distributions of atoms in an two dimensional alloy: random distribution (a), periodic (long range) ordered alloy (b) and short range ordered alloy with strong segregation (c). The alloys b) and c) were created using Monte-Carlo simulations with $\Delta E < 0$ and $\Delta E > 0$ respectively (see section 3.4).

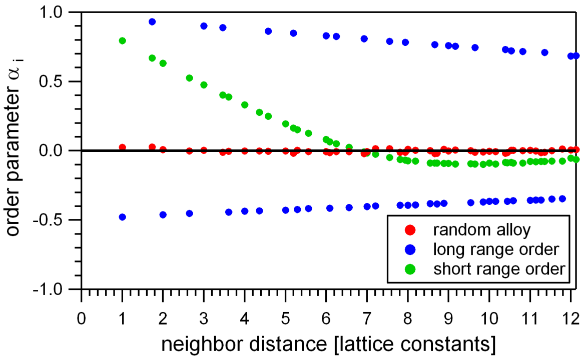

Figure 3.2: Order parameters $\alpha(R)$ as a function of the neighbor distance R (in lattice constants) instead of the neighbor order i for the alloys displayed in Fig. 3.1.

very quickly. The range on which the sign of α_i changes is a measurement for the averaged size of the segregated areas. The averaging includes the areas of both kinds of atoms, A and B. Long range order, signalized by a non vanishing order parameter even for large distances, can only form for alloy ratios which allow a periodic pattern of the alloy atoms in the lattice structure. The alternating of A and B atoms in the lattice is reflected by the jumps of the order parameter between two values, for a perfect $\sqrt{3} \times \sqrt{3}$ lattice between 1 and -0.5. Alloys with no or only short range order also called "disordered alloys" in contrast to "ordered alloys" with a periodic structure.

3.1.2 Electronics properties of binary alloys

The lattice constant in binary (A_xB_{1-x}) and pseudobinary alloys ($A_xB_{1-x}N$) can be approximately interpolated between the pure phases A and B or AN and BN respectively (this is known as Vegard's Law) [35]. For the electronic properties, the linear interpolation has often to be complemented by a nonlinear part known as bowing which is attributed to the composition disorder in the alloy [36]. For example the evolution of the band gap energy E_g with the ratio x in semiconductors is described by

$$E_g(x) = xE_g(\mathrm{AN}) + (1-x)E_g(\mathrm{BN}) - bx(1-x) \tag{3.2}$$

with b as the empirical bowing parameter and $E_g(\mathrm{AN})$ ($E_g(\mathrm{BN})$) the band gap in the pure AN (BN) phase. ARPES measurements on Ag/Au(111) [37] demonstrated that in an AgAu alloy the electronic properties of the surface state like binding energy or Rashba parameter (see section 3.2.2) are also intermediate values depending on the proportion of Au atoms the surface state probes. In contrast, it was demonstrated that in the segregated case (a thin submonolayer film of Ag on the Au surface) there is a coexistence of two different bands, one in the Ag areas and in the Au ares, indicating a localization of the band structure in the respective surfaces. A similar linear interpolated behavior was found for the pseudobinary mixed surface alloy $\mathrm{Bi}_x\mathrm{Pb}_{1-x}$/Ag(111) [19], while for the related $\mathrm{Bi}_x\mathrm{Sb}_{1-x}$/Ag(111) a strong non-linear behavior was found, with a band onset shifting even beyond the boundaries set by the pure surface alloys Bi/Ag(111) and Sb/Ag(111) [20] (see section 3.2.4).

In addition to the shift of the binding energy with concentration (chemical shift), a broadening of core level peaks was found in XPS measurements of metal alloys like $\mathrm{Cu}_x\mathrm{Pd}_{1-x}$, which was attributed to the disorder in the alloy [38]. This was described in a simple model with the aid of a Madelung potential V_M^i in addition to the intra-atomic potential V_{ia}^i at the lattice site i:

$$V^i = V_{ia}^i + V_M^i = \frac{Q_i}{r} + \sum_{j\neq i} \frac{Q_j}{r_{ij}} \tag{3.3}$$

with r as the effective radius of atom i. The charges Q_i and Q_j at lattice sites i and j depend only on the nearest neighbors as defined by Magri's linear charge model [39]

$$Q = 2S_0\lambda_1 N_1 \tag{3.4}$$

Here, S_0 is the sign of the charge at the lattice site, λ_1 is an empirical parameter setting the scale of the charges and N_1 is the number of nearest unlike neighbors. The average potential for one kind of atom in a random alloy, defining the chemical shift, can thus be written as [40]

$$\langle V \rangle = \frac{2\lambda_1 S_0}{R} \langle N_1 \rangle \tag{3.5}$$

with the variation due to the local disorder

$$\sigma_V^2 = \frac{4\lambda_1^2}{R^2} x(1-x) \sum_{\alpha_1}^{\infty} f_\alpha^2(1) Z_\alpha \propto x(1-x) \tag{3.6}$$

x is the alloy ratio and f_α are a series of constants for different neighbor shells α depending only on the general structure of the lattice. The Madelung potential model is applicable for electrons strongly bound to the atom and not very useful to describe the more delocalized valence and conduction states. Still it demonstrates how a chemically disordered surrounding can have an influence on the electronic structure.

In general, binary alloys allow to create materials with new electronic properties which depend on the composition. But this dependence is not necessarily linear, and the new electronic properties must not even lie in between the pure components. These electronic properties can be further modified by local disorder and except for special compositions, alloys are disordered systems. STM allows to directly probe the effect of the disorder, which is only indirectly accessible for non-local techniques as ARPES or XPS. To study the correlation between the local disorder and the electronic structure, a two dimensional disordered alloy system with an defined electronic structure is necessary as only the topmost surface layer is accessible to STM. Candidates for these measurements are the pseudobinary surface alloys $\mathrm{Bi}_x\mathrm{Pb}_{1-x}$/Ag(111) and $\mathrm{Bi}_x\mathrm{Sb}_{1-x}$/Ag(111)which, so far, have only been studied with ARPES.

3.2 Surface alloys

A surface alloy is a phase which can form when, by depositing submonolayer amounts of a material A onto a metallic substrate B, a fraction of the substrate atoms from the topmost layer are replaced by the deposited atoms. Surface alloys differ from normal alloys as their components are generally not miscible in the bulk. Nowadays there is a wide range of such material combinations known to form surface alloys such as Au/Ni [30], Ag/Cu [16] or

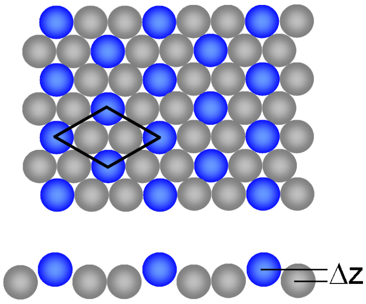

Figure 3.3: Topographic structure of the top most layer of the pure surface alloys. The black diamond in the top view shows the unit cell of the $\sqrt{3} \times \sqrt{3}\,\mathrm{R}30°$surface reconstruction. The side view shows the relaxation Δz of the atoms (not to scale).

Pb/Cu [15]. Due to the immiscibility, there is no alloying in the subsurface layers so that a purely 2D alloy is formed. Surface alloys form a great variety of different structures and a compilation of these can be found in [41]. The following section will concentrate on a class of surface alloys with the (111)-surfaces of silver (Ag) and copper (Cu) as substrates and bismuth (Bi), lead (Pb) and antimony (Sb) as substituents. Even though these systems are substitutional alloys, their limitation to the surface layer and to the ordered $\sqrt{3} \times \sqrt{3}\,\mathrm{R}30°$ phase generates a completely new two dimensional electronic structure, which can not be deduced from the pure phases of the components.

3.2.1 Topographic structure of the surface alloys

The surface alloys created from the Cu(111) and Ag(111) surfaces as substrates and Bi, Pb, and Sb as substitutional atoms form all the same $\sqrt{3} \times \sqrt{3}\,\mathrm{R}30°$ reconstruction at a coverage of $1/3$ monolayer (ML), where every third substrate atom is replaced by an substitutional atom [15, 27, 42–45]. A model of this reconstruction is illustrated in Fig. 3.3. For surface alloys on the Ag(111) surface the new lattice constant due to the reconstruction is $a = \sqrt{3} \cdot 2.88\,\text{Å} = 5.0\,\text{Å}$. This reconstruction reduces the tensile stress of the surface [46] which is in general on metal surfaces a result of the different charge distribution compared to the ideal bulk distribution [47]. Sb/Ag(111) presents an exception to the rule of immiscibility as Sb is smaller then Ag and they can form bulk alloys for small compositions up to 26.6 at.% Sb [48]. STM measurements of Bi/Ag(111) [49] and Pb/Ag(111) [50] and XRD measurments of Bi/Cu(111) [42] show that for alloy atom coverages$< 1/3\,$ML a disordered alloy is formed, while for coverages $> 1/3\,$ML dealloying takes place and an overlayer is formed. Relaxations of the alloy atoms out of the Ag surface layer have been determined for the alloys on Ag(111) using IV-LEED measurements [51]. The relaxations Δz are $0.65 \pm 0.10\,\text{Å}$ for Bi/Ag(111), $0.46 \pm 0.06\,\text{Å}$ for Pb/Ag(111) and $0.10 \pm 0.02\,\text{Å}$ for the fcc top layer stacking phase of Sb/Ag(111).

3.2.2 Electronic structure of surface alloys

The electronic structure of the surface alloys is of special interest, as these systems exhibit Rashba spin-splitting, which is a result of spin-orbit interaction. The size of the splitting that is found in some of these systems is extremely large compared to other systems with Rashba spin-splitting such as pure metal surfaces or interfaces of semiconductor heterostructures.

Spin-orbit interaction

Spin orbit interaction is a relativistic effect that can be derived in a simple, classical way: Assume an electron that moves with a velocity $\vec{v}$ relative to the spherical electrostatic field $\vec{E}(\vec{r}) = -\frac{1}{e}\vec{\nabla}V(\vec{r}) = -\frac{1}{e}\frac{\partial V(\vec{r})}{\partial r}\frac{\vec{r}}{r}$ of a positively charged nucleus with $V(\vec{r})$ as the potential energy. In its rest frame, the electron sees a magnetic field $\vec{B}$ given by the Lorentz transformation

$$\vec{B}' = \gamma\left(\vec{B} - \frac{1}{c}\left(\vec{\beta}\times\vec{E}\right)\right) - \frac{\gamma^2}{\gamma+1}\vec{\beta}\left(\vec{\beta}\cdot\vec{B}\right) \tag{3.7}$$

with the Lorentz factor $\gamma = \frac{1}{\sqrt{1-\beta^2}}$ and $\vec{\beta} = \frac{\vec{v}}{c}$. In the non-relativistic limit $v \ll c$ ($\gamma \approx 1$) and for $\vec{B} = 0$ the transformation can be simplified to

$$\vec{B}' \approx -\frac{1}{c^2}\left(\vec{v}\times\vec{E}\right) \tag{3.8}$$

The interaction of the electron spin $\vec{s}$ with this magnetic field is given by $\mathcal{H} = -\vec{\mu}\vec{B}'$, with the magnetic moment $\vec{\mu} = -\frac{g_e\mu_B}{\hbar}\vec{s}$ of the electron and the Landé factor $g_e \approx 2$. So the interaction can be written as

$$\mathcal{H} = -\frac{2\mu_B}{\hbar m_e c^2}\frac{1}{r}\frac{\partial V(\vec{r})}{\partial r}(\vec{r}\times\vec{p})\vec{s} \tag{3.9}$$

With the Bohr magneton $\mu_B = \frac{e\hbar}{2m_e}$ and the angular momentum $\vec{l} = \vec{r}\times\vec{p}$, one can see that this is indeed an interaction bewteen spin and the orbital angular momentum of the electron

$$\mathcal{H}_{\text{SOI}} = -\frac{1}{m_e^2c^2}\frac{1}{r}\frac{\partial V(\vec{r})}{\partial r}\left(\vec{l}\cdot\vec{s}\right) \tag{3.10}$$

In the correct quantum mechanical derivation, The spin orbit interaction is derived from the Dirac equation, which is the relativistic form of the Schrödinger equation

$$\left[c\vec{\alpha}\vec{p} + \beta m_e c^2 + V(\vec{r})\right]|\Psi\rangle = E|\Psi\rangle \tag{3.11}$$

with $\vec{\alpha}$ given by the Pauli spin matrices $\vec{\sigma} = (\sigma_x, \sigma_y, \sigma_z)$ and β given by the (2×2) unity matrix $\mathbb{1}$

$$\vec{\alpha} = \begin{pmatrix} 0 & \vec{\sigma} \\ \vec{\sigma} & 0 \end{pmatrix};\ \beta = \begin{pmatrix} \mathbb{1} & 0 \\ 0 & -\mathbb{1} \end{pmatrix} \tag{3.12}$$

so $|\Psi\rangle = (|\Psi_A\rangle, |\Psi_B\rangle)$ itself is a four component Dirac-spinor. With this, the Dirac equation can be divided into two equations

$$\begin{aligned} c\vec{\sigma}\vec{p}|\Psi_B\rangle &= \left(E - m_e c^2 - V(\vec{r})\right)|\Psi_A\rangle & (3.13)\\ c\vec{\sigma}\vec{p}|\Psi_A\rangle &= \left(E + m_e c^2 - V(\vec{r})\right)|\Psi_B\rangle & (3.14)\end{aligned}$$

$|\Psi_B\rangle = \frac{c\vec{\sigma}\vec{p}}{E+m_e c^2 - V(\vec{r})}|\Psi_A\rangle$ can be eliminated and in a non-relativistic approximation including terms of the order of $(\frac{v^2}{c^2})$ [52] one obtains the nonrelativistic Dirac equation

$$\left[m_e c^2 + \frac{\vec{p}^2}{2m_e} - \frac{\vec{p}^4}{8m_e^3c^2} - V(\vec{r}) - \frac{\hbar^2}{8m_e^2c^2}\Delta V(\vec{r}) - \frac{\hbar}{4m_e^2c^2}\left(\vec{\nabla}V(\vec{r}) \times \vec{p}\right)\vec{\sigma}\right]|\Psi_A\rangle = E|\Psi_A\rangle \tag{3.15}$$

The last term describes the the spin orbit interaction and with $\vec{s} = \frac{\hbar}{2}\vec{\sigma}$ it can, similar to Eq. 3.10, be written as

$$\mathcal{H}_{\text{SOI}} = -\frac{1}{2me_e^2c^2}\frac{1}{r}\frac{\partial V(\vec{r})}{\partial r}\left(\vec{l}\cdot\vec{s}\right) \tag{3.16}$$

The missing factor $\frac{1}{2}$ in the classical spin-orbit interaction given by Eq. 3.10 is a result of the fact, that the rest frame of the electron is not an inertial frame, and the Lorentz transformation requires inertial systems. For bound electrons the potential gradient $\frac{\partial V(\vec{r})}{\partial r}$ is determined by the core charge Z which means, that the strength of the spin-orbit coupling becomes larger for heavy elements with increasing Z.

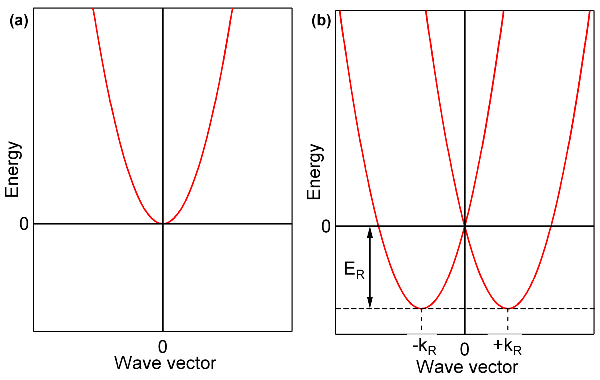

Figure 3.4: $E(k)$ dispersion of a free electron gas given by equation 3.4 without spin-orbit interaction (a) and with Rashba spin-orbit interaction (b)

The Rashba effect in surface alloys

It is known from calculations that the surface states are mostly localized in topmost surface layer they form a two dimensional electron gas which is free in x- and y-direction, but confined in the z-direction perpendicular to the surface [21]. In a simple, non-magnetic bulk system, the combination of inversion symmetry $(E(\vec{k},\downarrow) = E(-\vec{k},\downarrow))$ and time reversal symmetry $(E(\vec{k},\uparrow) = E(-\vec{k},\downarrow))$ assures the degeneracy of the spins $E(\vec{k},\downarrow) = E(\vec{k},\uparrow)$ (Kramer's degeneracy), and only if one of the symmetries is broken, the spin degeneracy can be lifted. Besides the breaking of time reversal symmetry by magnetic fields, breaking of the structural inversion symmetry can be observed, for example, at interfaces of semiconductor heterostructures due to the asymmetric confinement potential or at surfaces of metals. Such a splitting has been first measured in GaAs-Al$_x$Ga$_{1-x}As$ heterostructures [53, 54] and has been theoretically described by Bychkov and Rashba as a result of spin-orbit interaction [22].

The Rashba model can be deduced from the spin-orbit interaction term in Eq. 3.15

$$\mathcal{H}_{\mathrm{SOI}} = -\frac{\hbar}{4m_e^2c^2}\left(\vec{\nabla}V(\vec{r})\times\vec{p}\right)\vec{\sigma} \tag{3.17}$$

With only a potential gradient perpendicular to the surface $\vec{\nabla}V = \frac{\partial V(z)}{\partial z}\vec{e}_z$ and the movement of the electrons confined in a plane parallel to the surface $\vec{p} = \hbar\vec{k}_{\|} = \hbar\left(k_x, k_y, 0\right)$ this can be written as

$$\mathcal{H}_{\mathrm{SOI}} = \alpha_R\left(\vec{k}_{\|}\times\vec{e}_z\right)\vec{\sigma} \tag{3.18}$$

with the Rashba parameter $\alpha_R \propto \frac{\partial V(z)}{\partial z}$ giving the strength of the spin-orbit interaction.

Solving the Schrödinger equation including this spin-orbit interaction term leads to the energy dispersion

$$E(k_\parallel) = \frac{\hbar^2 k_\parallel^2}{2m^*} \pm \alpha_R k_\parallel = \frac{\hbar^2}{2m^*} \left(k_\parallel \pm k_R\right)^2 - E_R \tag{3.19}$$

with the electron effective mass m^*, the momentum splitting $k_R = \alpha_R \frac{m^*}{\hbar^2}$ and the corresponding Rashba energy $E_R = \frac{\hbar^2 k_R^2}{2m^*}$. In real systems, there will be an additional energy shift E_0 not included in Eq. 3.19, which gives the position of the band onset relative to the Fermi energy normally used as reference energy. The dispersion relation $E(k_\parallel)$ is illustrated in Fig. 3.4 a) for $\alpha_R = 0$ (no spin-orbit interaction) and b) for $\alpha_R > 0$. For the latter case, Eq. 3.19 describes two parabolas which are shifted in k-direction away from $k = 0$ by $\pm k_R$, which lifts the degeneracy of the states with different eigenvalues of $\vec{\sigma}$. The parabolas have to cross a the Γ point ($k_\parallel = 0$) since at this point the degeneracy cannot be lifted by inversion symmetry.

The first observation of the Rashba spin-orbit interaction on metal surfaces was on Au(111) [55], but a much larger splitting was found for the surface alloys Bi/Ag(111) ($k_R = 0.13\,\text{Å}^{-1}$) [21] and Pb/Ag(111) ($k_R = 0.03\,\text{Å}^{-1}$) [27]. An overview of the characteristic parameters α_R, k_R and E_R for the different surface alloys and noble metal (111) surfaces can be found in [51]. The difference in the band structure of Bi/Ag(111) with the band onset in the occupied states and Pb/Ag(111) where the band onset lies in the unocuppied states can be explained by the additional valence electron of Bi ($6s^2 6p^3$) compared to Pb ($6s^2 6p^2$) [27]. As the atomic number of Bi ($Z = 83$) and Pb ($Z = 82$) is very similar, the difference in the Rashba splitting was attributed to the orbital character of the surface state which is mostly sp_z but with a larger fraction of $p_{(x,y)}$ contribution for Bi/Ag(111) than for Pb/Ag(111) [19]. An additional contribution is the larger outward relaxation of Bi atoms compared to the Pb atoms.

The large size of the splitting was unexpected as the splitting in the Ag(111) and Bi(111) surface states is much smaller. To account for the large splitting found in these systems, besides the contribution of the atomic spin-orbit interaction and the potential gradient $\frac{\partial V}{\partial z}$ perpendicular to the surface plane [56], the model can be extended to include in-plane potential gradients $\frac{\partial V}{\partial r_\parallel}$ resulting from in-plane inversion symmetry breaking [57].

The Rashba model has its limitations as it calculates the strength of the splitting as a function of an effective potential gradient which the two dimensional electron gas sees, but cannot give the origin of the splitting. For example, it was found for the surface alloys, that the outward relaxation of the alloy atoms out of the substrate surface layer has a great influence on the Rashba parameter α_R and consequently on the splitting k_R and the

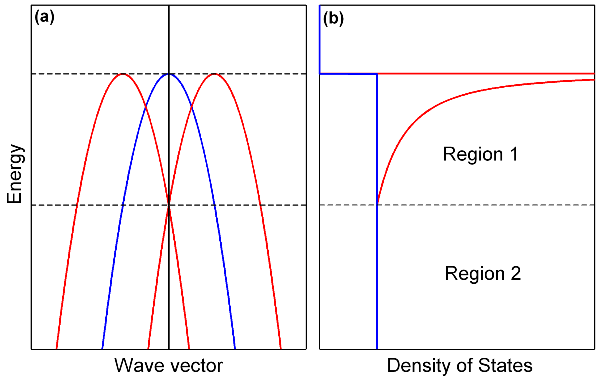

Figure 3.5: Comparison of the energy dispersion (a) and the density of states (b) of a two dimension electron gas with negative effective mass m^* as found for the surface alloys. The distribution and the density of states are illustrated without (blue) and with spin-orbit interaction (red). In the latter case, the density of states has a different behavior above and below the crossing point of the bands at $k = 0$.

Rashba energy E_R [51].

3.2.3 Electronic structure of surface alloys measured with STS

While the majority of the measurements of the electronic structure of the surface alloys were performed using ARPES, a non-local technique but able to directly measure the energy dispersion $E(\vec{k}_{\parallel})$, local measurements using STS are rare. Such measurements which were able to measure the effect of the splitting were performed on the surface alloys Bi/Ag(111) and Pb/Ag(111) [27]. For a two dimensional electron gas, the energy dispersion and the corresponding density of states (DOS) $D(E)$, which is measured in STS experiments, are illustrated in figure 3.5 a) and b) respectively. In contrast to the case without spin-orbit interaction, for which the band onset gives rise to a step in the DOS, with spin-orbit interaction, the DOS can be divided on the into two energy regions 1 and 2

$$D(E) = \begin{cases} \frac{|m^*|}{\pi\hbar^2}\sqrt{\frac{E_R}{E-E_0}} & \text{region I} \\ \\ \frac{|m^*|}{\pi\hbar^2} = \text{const.} & \text{region II} \end{cases} \tag{3.20}$$

with E_0 as the energy of the band onset. In region I, between the band onset and the crossing point of the parabolic bands, the DOS behaves similar to a one dimensional electron gas with a van Hove singularity at the band onset. In contrast to that, the DOS in the region II has the form for a a normal two dimensional electron gas with a constant DOS. In real STS measurements, the singularity will be smeared out into an asymmetric peak due to finite life time and experimental broadening effects like finite temperature and lock-in modulation amplitude, as it has been demonstrated in [27]. In addition, calculations show that disorder scattering, for example at impurities, can also have a broadening effect on electronic features in such two dimensional electron gases [58]. Nonetheless, such a peak at a step edge is a signature of the Rashba splitting and the estimation of the size of region I from the STS measurements can give a measure of the size of the splitting, which can be compared to results from ARPES measurements.

In reference [59] the standing wave interference patterns of scattered electrons of the two dimensional electron gas of Bi/Ag(111) was measured in dI/dV-maps for different bias voltages. From the different standing wave patterns the respective wave vectors and so the energy dispersion was deduced, but the information of the splitting is lost in the interference as predicted by [56]. Standing wave patterns were only found in the energy region II of the band structure, as back-scattering processes in region I would only be possible in combination with a spin flip.

3.2.4 Modifying the electronic structure in pseudobinary surface alloys

The pure surface alloys Bi/Ag(111), Pb/Ag(111) and Sb/Ag(111) form an ideal basis for pseudobinary alloys due to their similar geometric structure. All three alloys form the same $\sqrt{3} \times \sqrt{3}\,\mathrm{R}30^\circ$ reconstruction with a periodicity of 5 Å, and differ only in the outward relaxation of the alloy atoms out of the Ag(111) surface plane. Experimental measurements as well as theoretical calculations for $\mathrm{Bi}_x\mathrm{Pb}_{1-x}$/Ag(111) [19] and $\mathrm{Bi}_x\mathrm{Sb}_{1-x}$/Ag(111) [20] found a continuous evolution of the electronic structure based on the properties of the pure surface alloys as given by Eq. 3.2. While for $\mathrm{Bi}_x\mathrm{Pb}_{1-x}$/Ag(111) the interpolation follows a linear evolution, $\mathrm{Bi}_x\mathrm{Sb}_{1-x}$/Ag(111) shows a strong deviation from the linear behavior especially for the energy offset E_0, similar to the bowing effect in semiconductor alloys. With the difference in the valence electrons between Bi (or the isoelectric Sb) and Pb on the one hand and the similar atomic number of Bi and Pb compared to lighter Sb on the other hand, a combination of all three into a pseudotrinary surface alloy $\mathrm{Bi}_x\mathrm{Pb}_y\mathrm{Sb}_{1-x-y}$/Ag(111) allows a almost independent tuning of both the Fermi energy and the Rashba splitting [20, 60] within the boundaries set by the pure surface alloys.

Not surprisingly, the formation the $\sqrt{3} \times \sqrt{3}\,\mathrm{R}30^\circ$ reconstruction has been confirmed for

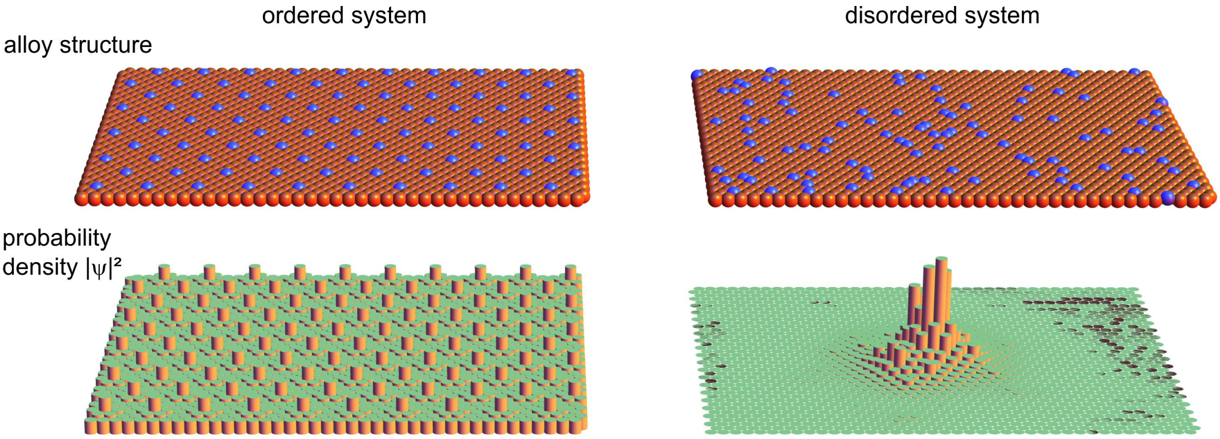

Figure 3.6: Illustration of Anderson localization. In case of an ordered system, the probability density of the wave function extends over the whole system and can be described by a periodic Bloch wave. In the case of disorder, the wave function is localized and the probability density drops exponentially to zero.

the mixed surface alloys by LEED measurements [19]. However, nothing more is known of the topographic structure and distribution of the alloy atoms in the $\sqrt{3} \times \sqrt{3}\,\mathrm{R}30^\circ$ lattice. In the first principle calculations of the mixed surface alloys using coherent potential approximation, local disorder is ignored and the relaxation of the alloy atoms is assumed to be uniform and is interpolated between the pure surface alloys. But the broadening of the bands found in the ARPES measurements is a similar indicator for local disorder as the broadening found in core level XPS measurements (see section 3.1.2). I-V-LEED measurements show a continuous evolution of the structure from one pure surface alloy to the other but there is no comparison with structural models.

This continuous evolution of the of the chemical composition and electronic structure similar to bulk alloys in combination with their localization in the topmost surface layer as a two dimensional system accessible to STM makes these systems a unique opportunity to study the electronic structure of disordered alloys on a local scale.

3.3 Anderson Localization

3.3.1 Basic principle of Anderson localization

The normal description of electronic states using infinitely extended Bloch waves fails in disordered media because the condition of translation invariance is broken. Instead, by using a simple s-wave tight binding model for non-interacting electrons of the form

$$\mathcal{H} = \sum_i \epsilon_i |i\rangle\langle i| + \sum_{i,j} t_{ij} |i\rangle\langle j| \tag{3.21}$$

with the basis vectors $|i\rangle$ of the lattice structure, the on-site energy ϵ_i, and the the nearest neighbor interaction energy t_{ij}. Disorder can be introduced with either the on-site energy (with two discrete ϵ_i values for a binary alloy) or the interaction energy (for an amorphous system). Calculating the eigenvectors $|\psi\rangle$ and eigenvalues of the stationary Schrödinger equation $\mathcal{H}|\psi\rangle = E_\psi|\psi\rangle$ for a defined system (given by $|i\rangle$, ϵ_i and t_{ij}) allows to calculate for example the distribution of probability densities $|\langle\psi|i\rangle|^2$ on the lattice for a given disorder structure. It has been demonstrated [3, 61], that the electronic wave function is localized, meaning its propagation is limited to a certain area. The most prominent sign of this localization is the exponential drop of the wave function amplitude with distance given by [62]

$$|\psi(\vec{r})| \sim \exp\left[-\frac{|\vec{r} - \vec{r}_0|}{\xi}\right] \tag{3.22}$$

The decay parameter ξ is defined as the localization length. This effect of localization is illustrated in Fig. 3.6.

In some numerical studies, the influence of different boundary conditions (periodic and antiperiodic) on the energy eigenvalues was used [61]. In case of localized states, the difference ΔE in the energy eigenvalues of corresponding states for different boundary conditions should vanish, while for extended states energy difference should be of the size of the energy spacing $\frac{dE}{dN}$ between different states.

A third definition of localization is given by the participation ratio $(N\alpha)^{-1}$ [61] with α given by

$$\alpha = \frac{\sum\limits_{i=1}^{N} |a_i|^4}{(\sum\limits_{i=1}^{N} |a_i|^2)^2} \tag{3.23}$$

α will be minimal with value N^{-1} when the state is extended equally over all sites, and it will reach its maximum value 1 if the wave function is localized at a single site.

The effect of the wave function localization is not limited to electron waves. Instead, it is a general characteristic of waves and the localization of waves in disordered media has been demonstrated for variety of both quantum mechanical and classical waves: light [7,8], microwaves [6], matter waves [9–11], ultrasound [4, 5] and even water waves [63].

3.3.2 Metal-Insulator Transition

For electronic waves, a signature of localization can be found in transport measurements in the form of an metal-insulator transition when the Fermi level crosses over from extended into localized states. If there are no interactions of the electrons with other (quasi-) particles, the electrons in localized states do not contribute to the conductivity and a system changes it behavior from conducting (metallic) to insulating if the Fermi energy transits the mobility edge from extended states (which always contribute to the conductivity) to the localized states [64].

However, in early measurements of this transition in silicon MOSFETs, there is a competing influence of disorder and electron-correlation [12], and only recently it was possible for crystalline phase-change materials as GeSbTe to attribute the transition purely to disorder [13].

3.4 Monte-Carlo Simulations for alloy structures

Monte-Carlo Simulations based on the Metropolis method came into use with the advent of the first computers [65]. One example for an application of Monte-Carlo simulations are interacting states in thermal equilibrium on regular lattices with normally two or three dimensions (Ising lattice). This can be used to simulate ordering effects in alloys, especially order-disorder transitions [66].

3.4.1 Markov Chains

The description of a system by its distribution $\rho(\vec{p}, \vec{q})$ in the phase space with the Liouville equation is for a many-body system often not possible due to the great number of degrees of freedom. This can be simplified by reducing the number of degrees of freedom and neglecting effects on much smaller time- and length-scales. For example, if one is interested in atom hopping in a alloy lattice, the vibrations of the atoms can be generalized as a external heat bath. The evolution of the system can now be described by transitions from one state S_i into another state S_j. This is given by the master equation

$$\frac{dP(S_i,t)}{dt} = -\sum_j W_{ij} P(S_i,t) + \sum_j W_{ji} P(S_j,t) \qquad (3.24)$$

with $P(S_i, t)$ as the probability that the system is at a certain time t in a certain state S_i and W_{ij} as the transition probability from state S_i to S_j. The first term on the right side of Eq. 3.24 describes the probability, that the system is in the state S_i and transfers to any other state, while the second term describes the probability that the system transfers from any arbitrary state into the state S_i, thus forming probability loss and gain terms respectively. In the case of equilibrium, forward and reverse transitions between all states must be identical, a condition which is known as "detailed balance"

$$W_{ij}P(S_i) = W_{ji}P(S_j) \tag{3.25}$$

The probability for the state S_i is given by

$$P(S_i, t) = \frac{\exp\left[\frac{-E_i}{k_B T}\right]}{Z} \tag{3.26}$$

One problem remains, as the partition function Z cannot be calculated normally due to the great number of possible configurations (e.g. a system modeling a binary alloy with 1920 lattice sites and a ratio $x = 0.33$ as the one in Fig. 3.1 has $\backsim 10^{527}$ different configurations), the probabilities $P(S_i)$ are not known directly.

Monte-Carlo simulations circumvent this problem as they are based upon the generation of Markov chains, a series of configurations k(s) of a system for which the probability to generate a configuration k(t+1) only depends on the directly preceding configuration k(t) (first order Markov chain). A configuration represents one of the possible states $S_1, S_2, S_3 \ldots$ for the system, in the example of the alloy defined by the arrangement of the alloy atoms in the lattice. When each state is generated from a preceding state in a Markov chain, only the ratio of the probabilities $\frac{P_j}{P_i}$ is of importance and the partition function can be eliminated, leaving the energy difference between the final configuration S_j and the initial configuration S_i

$$\Delta E = E_j - E_i \tag{3.27}$$

as the relevant parameter. A possible transition rate that satisfies the condition of detailed balance given by Eq. 3.25 is used in the Metropolis algorithm.

3.4.2 Metropolis Algorithm

The Metropolis method can be used to simulate the distribution of the alloy atoms in the mixed surface alloys. As the alloy atoms (Bi, Pb, Sb) sit on fixed lattice sites, their interaction with the Ag atoms of the alloy layer and the substrate is independent of the location and only gives an additive constant to the total energy. The interaction between the Ag and the alloy atoms is important for the energy barrier that limits the alloy atom exchange to a certain rate. However, Monte Carlo simulations have their own definition of time (see below) so that such rates can be assumed to be one. In this regard, the Ag atoms can be thought of as host matrix which will be ignored in the simulations.

The Metropolis method starts with a random configuration $k(s = 0)$ by assigning the possible σ_i values to the lattice sites representing the possible states the lattice sites can assume, e.g. $\sigma_i = \pm 1$ for the two different types of atoms in a binary alloy. Since, in this case, the number of the different σ_i values is conserved, the desired ratio $x = \frac{A}{A+B}$ has to be taken into account for the random assignment. So the probability for $\sigma_i = +1$ corresponding to an atom A at site i is $p = x$ and for $\sigma_i = -1$ (atom B at site i) the probability is $p = 1 - x$. In the next step, the exchange step, a random site i in the lattice is chosen and, also randomly, a corresponding nearest neighbor site j. To create a new configuration $k(s + 1)$, the σ_i and σ_j values are exchanged with a probability given by the Metropolis function

$$W_{ij} = \min \left[1, \exp \left[-\frac{\Delta E}{k_B T} \right] \right] \tag{3.28}$$

The transition probability W_{ij} is one if the energy E_j of the final configuration is smaller than E_i. If E_j is larger, W_{ij} is given by the Boltzmann distribution. To see how to calculate ΔE, let us now assume an arbitrary but periodic lattice with $N = N_A + N_B$ lattice sites (no vacancies) and n nearest neighbors for each lattice site, where n is defined by the dimensionality and the lattice type (e.g. $n = 6$ for a two dimensional hexagonal lattice or $n = 12$ a three dimensional fcc lattice). Let us further assume that each lattice site can assume two states $\sigma_i = \pm 1$ with no external interaction and only nearest neighbor interaction between the lattice sites. The energy of the system is given by

$$E = \frac{1}{2} \sum_{i=1}^{N} \sum_{j=1}^{n} J \sigma_i \sigma_j \tag{3.29}$$

Here J is the nearest neighbor interaction energy, with $J = J_{AA}, J_{BB}, J_{AB}$ for A-A pairs, B-B pairs and A-B pairs respectively. As the simulations will be performed in the canonical ensemble with a constant number of atoms $N_A, N_B = \text{const.}$ (and because of $N = N_A + N_B$ a constant number of $\frac{n}{2} \cdot N$ neighbor pairs for a lattice with periodic boundary conditions), the interaction energy J can be reduced to an effective pair interaction energy

$$\Delta J = \frac{1}{2}(J_{AA} + J_{BB}) - J_{AB} \tag{3.30}$$

With n_{i+} (n_{i-}) the number of neighbor pairs with atoms of the same kind (different kind) in the configuration S_i, the energy can be simply expressed by

$$E_i = \Delta J(n_{i+} - n_{i-}) \tag{3.31}$$

with $E_i = 0$ defined for a system with $N_A = N_B$ and a totally random distribution. With that we have the necessary parameter to calculate new configurations in the Markov chain.

N repetitions of the exchange step, after which each lattice site was on average chosen once as the first exchange partner, are called one Monte-Carlo step (MCS), which is the fundamental time unit of the Monte-Carlo simulation and is, in this way, independent of the lattice size. After the simulation reached thermal equilibrium, the result has to be averaged over a number of MCS to minimize the effect of thermal fluctuations. It might be necessary to repeat the simulation several times with different initial configurations to minimize effects of the finite size of the lattice.

Normally, Monte-Carlo simulations allow to predict statistical behavior of systems down to a atomic scale for known interactions, but if this statistical behavior is known, for example from atomically and chemically resolved STM measurements, Monte-Carlo simulations can also work the other way around and give the opportunity to learn more about the interaction energies.

Chapter 4

Experimental Setup

A part of this project was the setup of a home-built ultra-high vacuum (UHV) system for a variable temperature (VT) STM. This system was also used for testing components and procedures for a new mK-STM system [67], especially the manipulator arm for the sample preparation. For this purpose, many components are imitating those of the mK-STM as close as possible, for example the cryostat with the STM support structure, or the use of a combined ex-situ active and passive damping systems.

4.1 The Experimental Setup

4.1.1 The UHV-System

For surface sensitive techniques like STM, well defined, clean sample surfaces are necessary as contaminations on the surface can distort such measurements or make them even impossible. There are nowadays standard techniques established to create clean sample surfaces (see section 4.2), but at ambient conditions, most surfaces do not stay clean for very long. For an estimation, one can calculate the flux F of molecules of an ideal gas with pressure p and temperature T impinging on a surface. This is given by [68]

$$F = \frac{p}{\sqrt{2\pi m k_B T}} \tag{4.1}$$

The probability that such a molecule hitting the surface actually remains there and does not fly away is given by the sticking coefficient S. Assuming a sticking coefficient $S = 1$, a pressure of $p = 1\,\mathrm{bar}$ and room temperature, it takes approximately $3.5 \cdot 10^{-10}\,\mathrm{s}$ to cover the surface with one molecule per nm^2. This timescale can be increases by decreasing

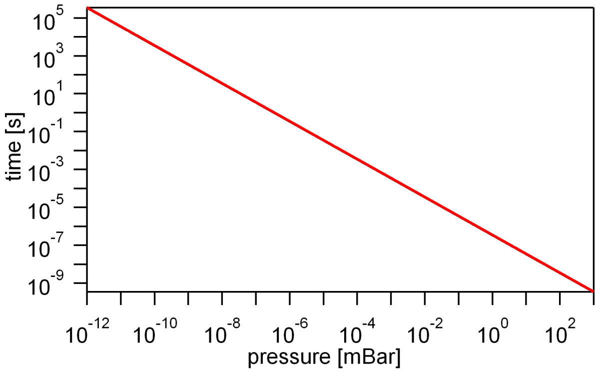

Figure 4.1: The time it takes to cover a clean surface with one molecule per nm^2 as function of the pressure p for $T = 300\,\mathrm{K}$, molecule mass $m = 28\,\mathrm{u}$ (N_2) and sticking coefficient $S = 1$.

the pressure and for $p = 4 \cdot 10^{-12}\,\mathrm{mbar}$, a timescale of one day is reached (see Fig. 4.1). Normally, the sticking coefficient is below 1 and from experience it is known, that sample surfaces remain clean enough for days when kept in UHV with pressures ranging from 10^{-9} to $10^{-11}\,\mathrm{mbar}$.

For the construction of UHV systems, materials with a very low vapor pressure have to be used to prevent outgassing even at low pressures in the UHV range. The UHV chamber itself is made out of stainless steel. Further common materials are oxygen-free copper for gaskets and parts which have to have a good thermal conductivity, molybdenum for parts that need to resist high temperatures and PEEK (polyether ether ketone), a UHV compatible plastic used for insulations and bearings of moving parts.

A CAD model of the UHV-system is displayed in Fig. 4.2 a). The UHV system consists of three parts, the STM chamber with the cryostat and the STM unit (Fig. 4.2 b)), the preparation chamber and a load-lock. The system is pumped by a sequential array of pumps, starting with a diaphragm pump and a drag turbo pump to create a prevacuum (not displayed in the CAD model), and as main turbo pumps one with magnetic bearings for the preparation chamber and another drag turbo pump for the load-lock. In addition, an ion pump and a titan sublimation pump are mounted on the STM chamber, allowing to pump this section separately during sample preparation (preventing contamination of the STM) or the whole system during measurements (when turbo pumps would induce too much noise).

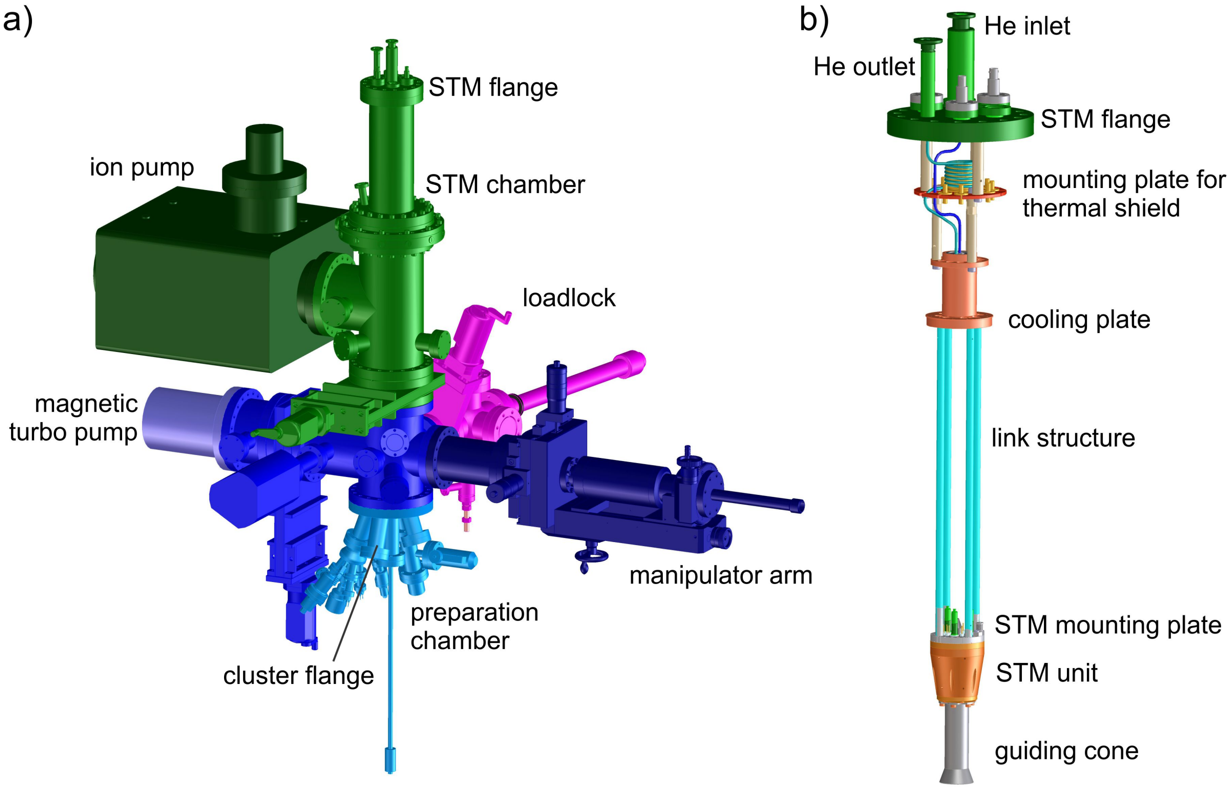

Figure 4.2: CAD model of the experimental setup (without the mounting frame and damping stages). a) The UHV-system with its three parts: Preparation chamber (blue color shades), STM chamber (green color shades) and loadlock (pink color shades). b) The cryostat (without thermal shielding) with the STM unit.

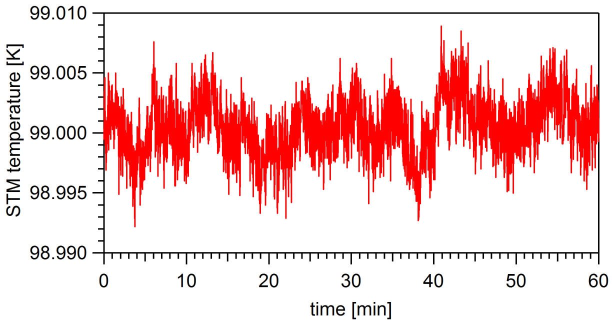

Figure 4.3: Temperature curve measured at the STM mounting plate for a temperature setpoint of 99 K. The temperature is varying in a range of ±5 mK around the temperature setpoint on timescale of minutes.

Cryostat

The home-built cryostat displayed in Fig. 4.2 b) is designed for the use of liquid helium (LHe) and is supplied from a common LHe-dewar. The circulation is completely driven by the pressure that builds up in the dewar by itself, and no pressured He gas supply or additional pumps are necessary. The temperature of the cryostat at the cooling plate depends on the helium flow through the cryostat, which in turn is regulated by the pressure in the dewar (which is usually kept at 0.5 bar) and a precision needle valve in the return line. The temperature at the STM mounting plate is regulated by a PID controlled heater element to keep a preset temperature. At a temperature in the range of 100 K, the LHe consumption is approximately 80 l per week ($\approx 0.5\,\mathrm{l/h}$), so extended measurements over a time range of several days are possible.

Fig. 4.3 shows the temperature measured at the STM mounting plate over one hour. As one can see there are irregular variations in the temperature of ±5 mK around the setpoint of 99 K. Even though this seems to be a small value, it can be shown that it is enough to have an effect on the STM measurements. As the STM unit casing is build from copper, the effect of this variations can be estimated using the the thermal expansion coefficient of copper at 100 K, $\alpha_{\mathrm{Cu}}(100\,\mathrm{K}) \approx 1 \cdot 10^{-5}\,\mathrm{K}^{-1}$. For the variations of ±5 mK found for this system, a 10 cm long piece of copper would change its length by ±5 nm, a measurable effect in STM.

One way to reduce the effect of such temperature variations would be to measure at even lower temperatures. As it can be seen in Fig. 4.4, the thermal expansion coefficient of Cu decreases with temperature. At 4 K, the thermal expansion coefficient drops to $\alpha_{\mathrm{Cu}}(4\,\mathrm{K}) \approx 4 \cdot 10^{-8}\,\mathrm{K}^{-1}$, two orders of magnitude lower compared to the value at 100 K,

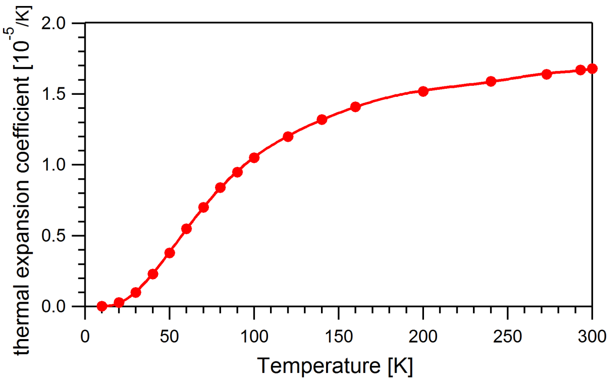

Figure 4.4: Thermal expansion coefficient of copper α_{Cu} as function of temperature. Going from room temperature to 100 K α_{Cu}, drops only by a factor of 1.6, but from 100 K to 4 K, it drops by over two orders of magnitude.

but a completely new cryostat design is necessary to reach these temperatures.

STM unit

The STM unit illustrated in Fig. 4.5 a) was already described in detail elsewhere [67]. Its conical shape is the result of an optimization of the tip-sample distance response to outside disturbances using a one dimensional model with springs and rigid masses to represent the STM [69]. For the coarse approach a commercial piezo step motor (attocube) is used (see Fig. 4.5 b). Both tip and sample can be transferred in-situ to the STM. At 100 K the available scan area is approximately 900 × 900 nm with a z-range of 190 nm.

As there is no visual access into the STM for the coarse approach, the capacitive coupling between tip and sample is measured using a lock-in amplifier. Once known, the coupling signals for the position of a fully retracted tip and the position from which the slower automated approach can be started are highly reproducible. Only in the case of a tip exchange, the positions have to be calibrated again by an automated approach over a longer distance.

Preparation chamber

The preparation chamber can be separated from STM chamber via a gate valve to prevent contamination of the STM and the ion pump during sample preparation. This is particularly necessary when the STM is cooled down and would act similar to a cryo pump. Relatively high pressures (up to $1 \cdot 10^{-6}$ mbar) can occur during the degasing of samples newly introduced into the UHV, or during sputtering.

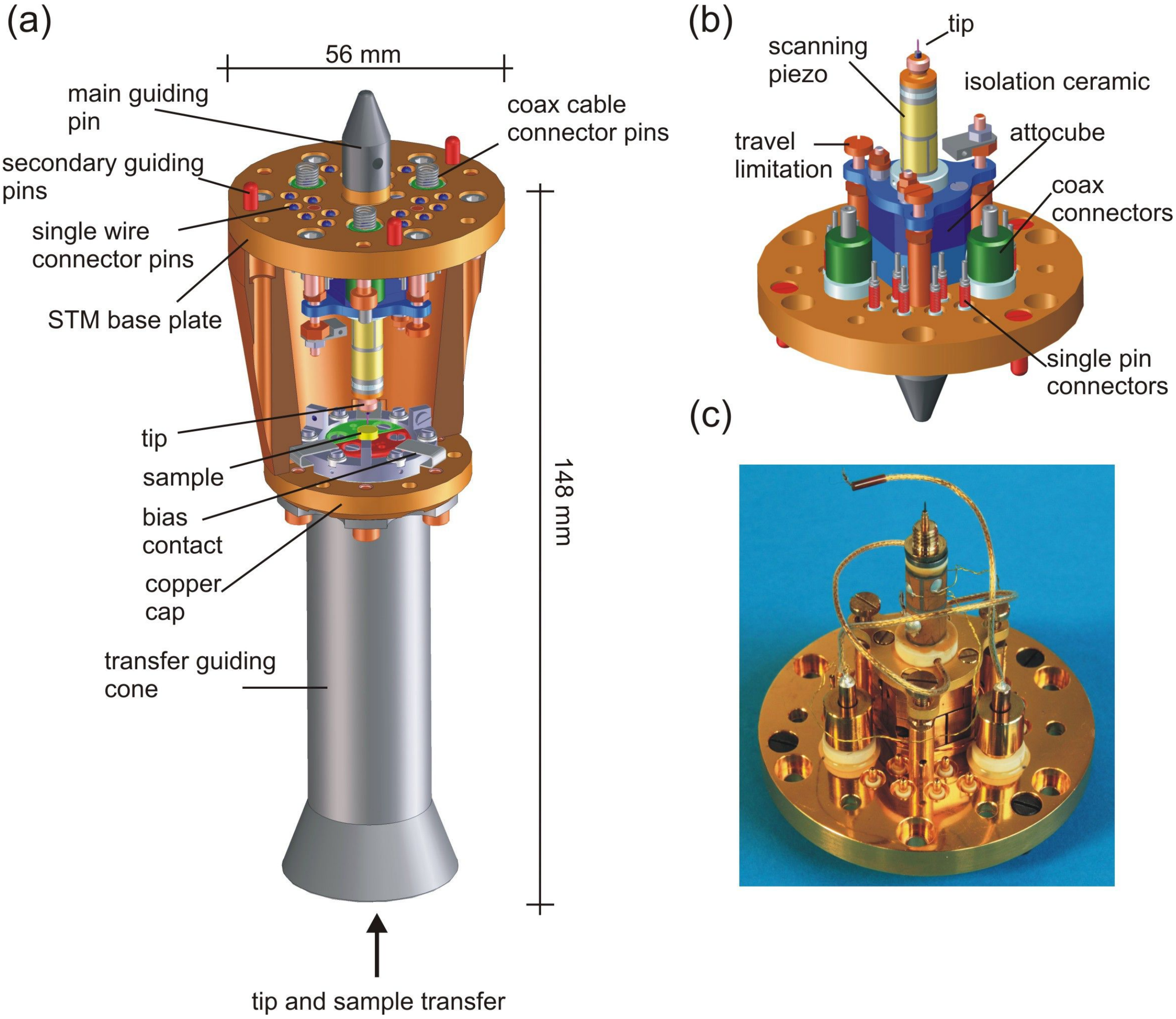

Figure 4.5: a) Design of the full STM head including the guiding cone for the tip/sample transfer mechanism. b) Interior of the STM with the attocube coarse approach motor and the scan piezo with the tip. Photograph of the parts illustrated in b) (reproduced from [67]).

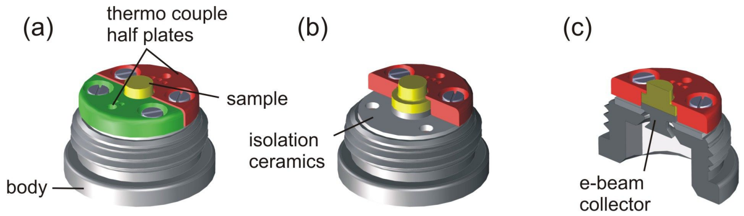

Figure 4.6: a) Design of the complete sample holder. The sample crystal sits on top of an electron collector and is clamped by the two thermocouple half discs. They are electrically isolated from sample holder body by an Al_2O_3 plate. (reproduced from [67]).

For sample preparation, a sputter gun and a commercial triple e-beam evaporator (Omicron) are mounted on the cluster flange at the bottom of the preparation chamber. Each of the three evaporator cells can be used independently and is equipped with its own ion flux monitor at the opening of the cell. This gives a reproducible although not calibrated measure for the evaporation rate and the flux monitor has to be calibrated individually for each new evaporant. The special design of the evaporator shutter allows to evaporate from individual cells or a combination of cells regardless of other cells that might be running. This allows for example to evaporate from two cells sequentially without time delay in between.

For sample heating, the manipulator arm is equipped with an electron beam heater, directly heating the sample crystal via the electron beam collector of the sample holder (see Fig. 4.6). The sample is clamped to the sample holder body by two half discs made from Pt and $Pt_{0.9}Rh_{0.1}$ respectively. Together with the sample crystal, the half plates form a type S thermocouple (one can assume that there is no temperature gradient in the sample crystal, so it does not give any contribution to the thermovoltage), allowing a direct and secure measurement of the sample temperature. The filament for the electron emission is mobile and can be removed from the UHV-chamber for repairs via the load-lock using the same transfer system as for the sample and tip.

With liquid nitrogen cooling of the manipulator arm head, sample preparation temperatures up to 1500°C for a short time (flashing) or up to 800°C for an extended time were tested. The sample temperatures are limited due to the melting point of Pt (1768°C) and the fact that Rh starts to segregate out of the Pt at temperatures in the range of 800°C to 1200°C [70].

4.1.2 Vibration Damping

STM measurements are very sensitive to vibrations that can induce oscillations of the tip and sample relative to each other. Sources of such vibrations can be pumps, ventilation systems or building vibration in general. To reduce such oscillations, the respective sources have to be switched off, or since this is not always possible as in the case of building vibrations, the STM has to be decoupled from its surroundings. This can be achieved in-situ by decoupling the STM head from the rest of the UHV system via springs and by using eddy-current damping or via a newly developed UHV-compatible active damping system in form of a Gough-Stewart platform [71]. To keep a close compatibility to the mK-STM, for which neither solution is applicable, an alternative with ex-situ damping stages is used. For this, the whole UHV chamber is decoupled from the floor. A combination of an actively controlled damping stage and a passive pneumatic damping stage generally brings the best results. Such a two stage damping system has been used for this system and the setup is illustrated in Fig. 4.7. As there is no damping state inside the UHV system, any noise source that has direct contact with the UHV chamber like turbopumps has to be identified and switched off during measurements.

Fig. 4.8 shows oscillation spectra measured at the STM flange as accelerations. For these measurements, as for the STM measurements, the turbopumps were switched off completely. Fig. 4.8 a) and b) show, how the active damping stage and the combination of active and passive damping stage can reduce the oscillation, especially in the low frequency range. The active dampers alone induce some noise in the frequency range from approximately 720 Hz to 850 Hz, but this is compensated by the passive dampers. A feature that remains in the oscillation spectra even in the fully damped case is a prominent peak at 100 Hz. The ion pump was identified as the source of this oscillation. The peak amplitude correlates with the high voltage applied to the ion pump as it can be seen in Fig. 4.8 d). Direct measurements of the dc high voltage signal of the commercial power supply revealed a ac modulation with a frequency of 100 Hz. The resulting mechanical oscillations are probably induced by electrostatic interactions between the freely hanging high voltage conducting line and the grounded pump casing. To eliminate this noise source, a homebuild high voltage power supply was used during measurements. As this power supply lacked a protection mode that prevents the ion pump from operating at too high pressures, the original power supply was still used during non-measurement times.

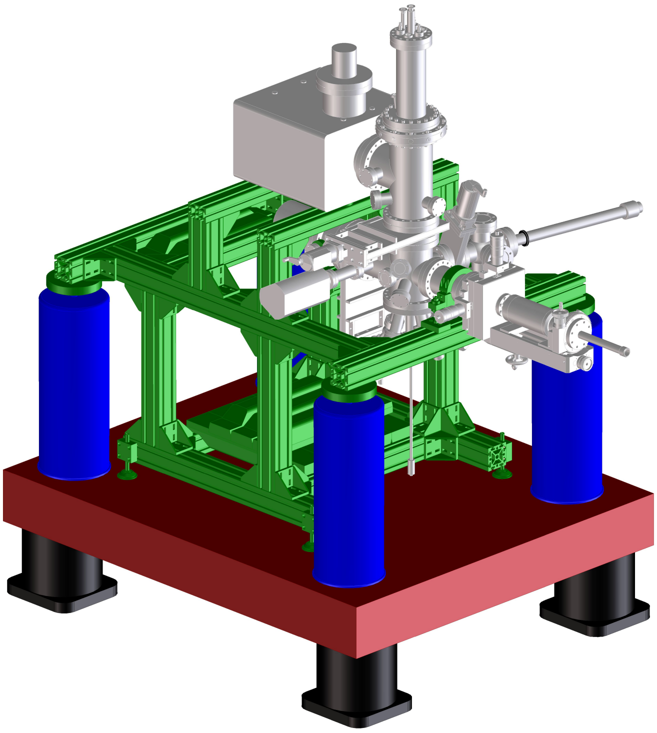

Figure 4.7: CAD model of the different damping stages of the measurement system: active damping stage with active damping units (black) and optical table (red), the passive damping stage with pneumatic passive damping units (blue) and mounting frame (green) and the UHV chamber itself (light gray)

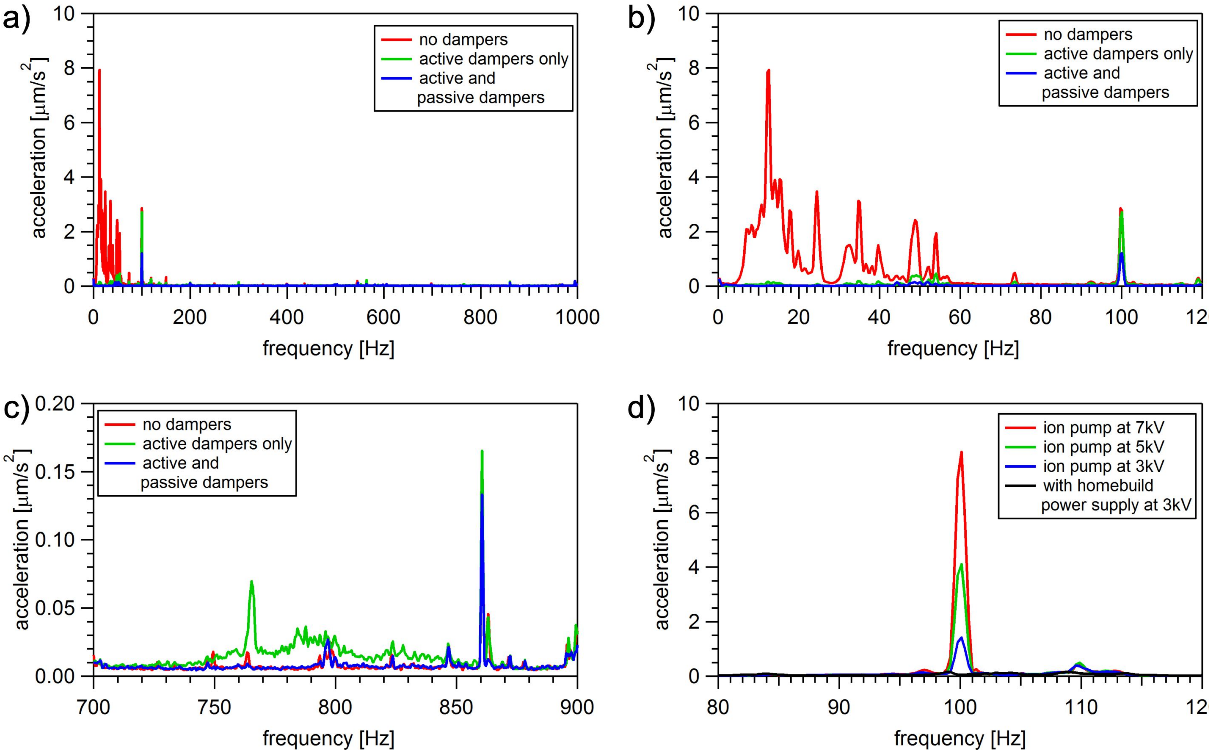

Figure 4.8: a)-c) Oscillation spectra measured at the STM flange to demonstrate the effect of the damping stages. Graph b) shows the strong damping of low frequency oscillations by the active damping stage. A striking feature is the remaining 100 Hz peak for which the ion pump was identified as source. Graph c) shows the high frequency range, where the active dampers actually induce some noise in the range from 720 Hz to 850 Hz. However, this can be compensated by the passive dampers. Graph d) shows the 100 Hz peak which is induced by a ac modulation detected in the ion pump high voltage. This noise source could be eliminated by using a homebuild high voltage power supply

4.2 Sample and Tip Preparation

4.2.1 Preparation of Metal Substrates

Ag(111)

As sample substrate, commercial single crystals with a (111) surfaces were used. The cleaning procedures for such single crystal surfaces in UHV are well established [72]. For Ag(111), the surface is cleaned in UHV by repeated cycles of sputtering and annealing. The surface is first sputtered at room temperature with Ar^+-ions at a pressure of $1 \cdot 10^{-6}$ with an energy of 1 keV resulting in an ion flux of $7.5\,\frac{\mu\mathrm{A}}{\mathrm{cm}^2}$ on the sample surface. For the final cycle, the Ar^+-ion energy was reduced to 600 eV resulting in a flux of $4.0\,\frac{\mu\mathrm{A}}{\mathrm{cm}^2}$. After sputtering, the sample was annealed at 500°C for 10 min.

Ag thin film on Pt(111)

Compared to surfaces of noble metals like Ag with their completely filled *d*-band, the Pt(111) surface is more reactive and cleaning it is more difficult and laborious. Similar to the Ag(111) surface, the Pt(111) surface was cleaned by repeated cycles of sputtering and annealing. While the same parameters for the sputtering were used, for the annealing temperatures from 600°C to 800°C were used. In addition, the sample was flashed (this means heated for few seconds) during the annealing several times at temperatures ranging from 1000°C to 1500°C.

Ag was subsequently evaporated at room temperature on the cleaned Pt(111) surface. To form a Ag film, after the evaporation, the sample was annealed up to 200°C. As there is no additional experimental method on the UHV system like a micro balance to calibrate the evaporators, STM measurements of a sub-monolayer preparation were used for a rough calibration.

4.2.2 Preparation of the Surface Alloys

The surface alloys were prepared by evaporating Bi, Pb or Sb from the tripple e-beam evaporator at a sample temperature of 300°C. For the evaporation of Sb on Ag(111), the high voltage applied to the crucible of the evaporator was usually well below 370 V, so it can be assumed that there is fcc top layer stacking and no Sb implantation into subsurface layers [51]. For the evaporator calibration, evaporation time and ion flux were varied until the surface alloy with its $1/3$ monolayer coverage was found as prevailing phase in STM measurements.

4.2.3 Tip Preparation

For the STM measurements, tips made from tungsten wire were used. Sharp W tips with a hyperbolic cone shape can be made by electrochemical etching in NaOH solution [73]. For the etching process, NaOH solution with a molar concentration of 1 mol/l (4 g of NaOH in 100 ml water) was used. To remove contaminations on the tip surface like tungsten oxide, the tip is treated in-situ by field emission. Finally, during STM measurements, the tip was further treated by tip dips and voltage pulses.

4.3 Outlook

The use of almost identical components for this system and the related mK-STM system, especially the identical STM unit and sample transfer allows extensive testing of advanced and newly developed components without time consuming disruptions of the mK-STM operations. One such advancement would be an additional coarse motor for horizontal movement in at least one direction, giving access to larger parts of the sample. Also, sample preparation procedures can be tested relatively quickly for variety of parameters as sample transfer, thermalization and tip approach take far less time then in the mK-STM system.

In addition to the testing purposes, this VT-STM system is in itself usable for performing studies of the topographic and electronic properties of surfaces as it is demonstrated in the following chapters.

The main problem of the system remains the drift due to small temperature variations at the STM base plate. The best solution for this problem would be a cryostat with a lower operation temperature, which would decrease the thermal expansion coefficients drastically. A flow cryostat with a small helium reservoir at the cold plate has been designed, and first test demonstrated that a base temperature of 4.2 K can be reached with this design. In addition, the new design is compatible with the Gough-Steward platform, allowing an additional damping stage to reduce noise from the cryostat [71]. However, this cryostat has not yet been tested for operations with low helium flow, which is necessary for experiments over an extended time scale.

Chapter 5

Surface Alloy Growth

While different aspects of the growth of Bi on Ag(111) [49, 74] and Pb on Ag(111) [50] have been studied with scanning tunneling microscopy, there are no local probe measurements of Sb on Ag(111) or any mixed surface alloy. The regular structure structure of Sb/Ag(111) has been determined by non-local techniques like IV-LEED [51, 75] and the comparison with theoretical models, but this is not possible for the disordered mixed surface alloys. Without any experimental data of the local structure, theoretical calculations of the electronic structure of the mixed surface alloys [19, 60] relied on mean-field theories like the coherent potential approximation [2] using an effective medium. Surface alloys with different coverages below 1/3 ML and their dealloying behavior for higher coverages have been studied on a local scale for Pb/Ag(111) [50] as well as Bi/Ag(111) [49], so the focus of this chapter lies on the 1/3 ML phase, which is of the most interest due to its peculiar electronic structure which will be discussed in chapter 6.

5.1 Growth of the pure surface alloy Sb/Ag(111)

Similar to Bi/Ag(111) and Pb/Ag(111), for Sb/Ag(111) a $\sqrt{3} \times \sqrt{3}\,\mathrm{R}30^\circ$ reconstruction was predicted by first-principle calculations [76] and found in LEED measurements [75]. Fig. 5.1 a) shows a topographic image of the pure surface alloy Sb/Ag(111) with its $\sqrt{3} \times \sqrt{3}\,\mathrm{R}30^\circ$ reconstruction. Like in the case of Bi/Ag(111) and Pb/Ag(111), the protrusions forming a hexagonal structure represent the outwards relaxed Sb atoms. The surface alloy covers the terraces completely and in contrast to Bi/Ag(111) and Pb/Ag(111), no monolayer phase was found for sample preparations at 300°C even for larger amounts of Sb (up to 4/3 ML).

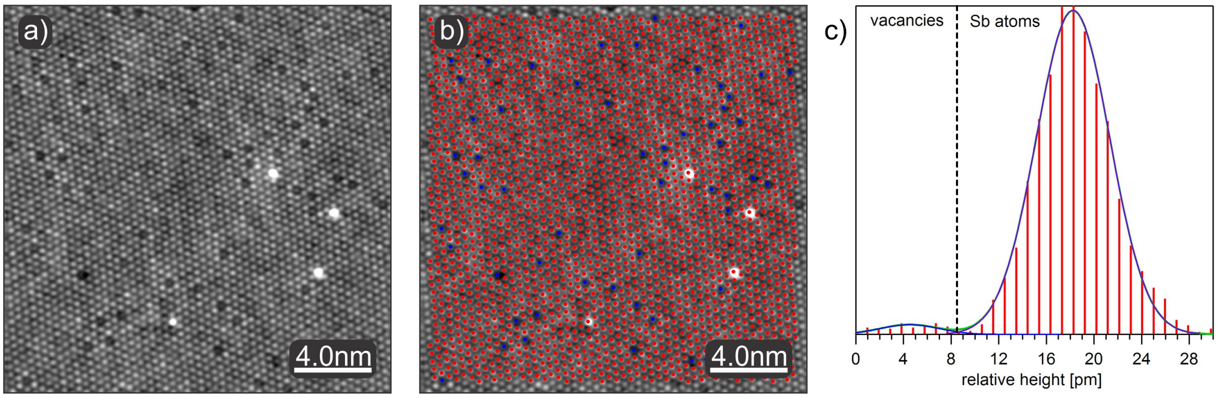

Figure 5.1: a) 20 × 20 nm topographic image of Sb/Ag(111) measured at 5 mV, 5.0 nA. b) The same image, overlaid with alloy structure determined from the topographic structure. Red dots mark the positions of Sb atoms, blue dots mark positions of vacancies. c) Height distribution of the marked locations in b). The dashed line marks the separation between the substitutional Sb atoms and the vacancies.

Some of the substitutional lattice positions show a considerably lower height. Using an automated algorithm to locate and analyze the substitutional lattice positions (see appendix A), these points can be identified (marked as blue lattice points in Fig. 5.1 b)). With the height distribution of the substitutional lattice sites, it can be demonstrated that their height differs distinctively from the substitutional Sb atoms (Fig. 5.1 c). Two distribution of atom heights can be distinguished in the histogram and both can be fitted with a gaussian distribution. The smaller gaussian distribution represents approximately 2% of the lattice sites.

It appears that the substrate atom has not been not replaced by an substitutional atom at these points. As there is an atom missing in the substitutional lattice, these points will be called vacancies. The average height difference between the Sb atoms and the vacancies was found to be 15 ± 1 pm. This is somewhat larger than the relaxation of 10 ± 2 pm found with IV-LEED measurements [51].

5.2 Mixed surface alloy growth

5.2.1 Topographic structure of $\mathrm{Bi}_x\mathrm{Pb}_{1-x}/\mathrm{Ag}(111)$

STM measurements on the mixed surface alloy $\mathrm{Bi}_x\mathrm{Pb}_{1-x}/\mathrm{Ag}(111)$ were performed for different alloy ratios from the whole composition range $x = 0$ to 1. Images of the topography

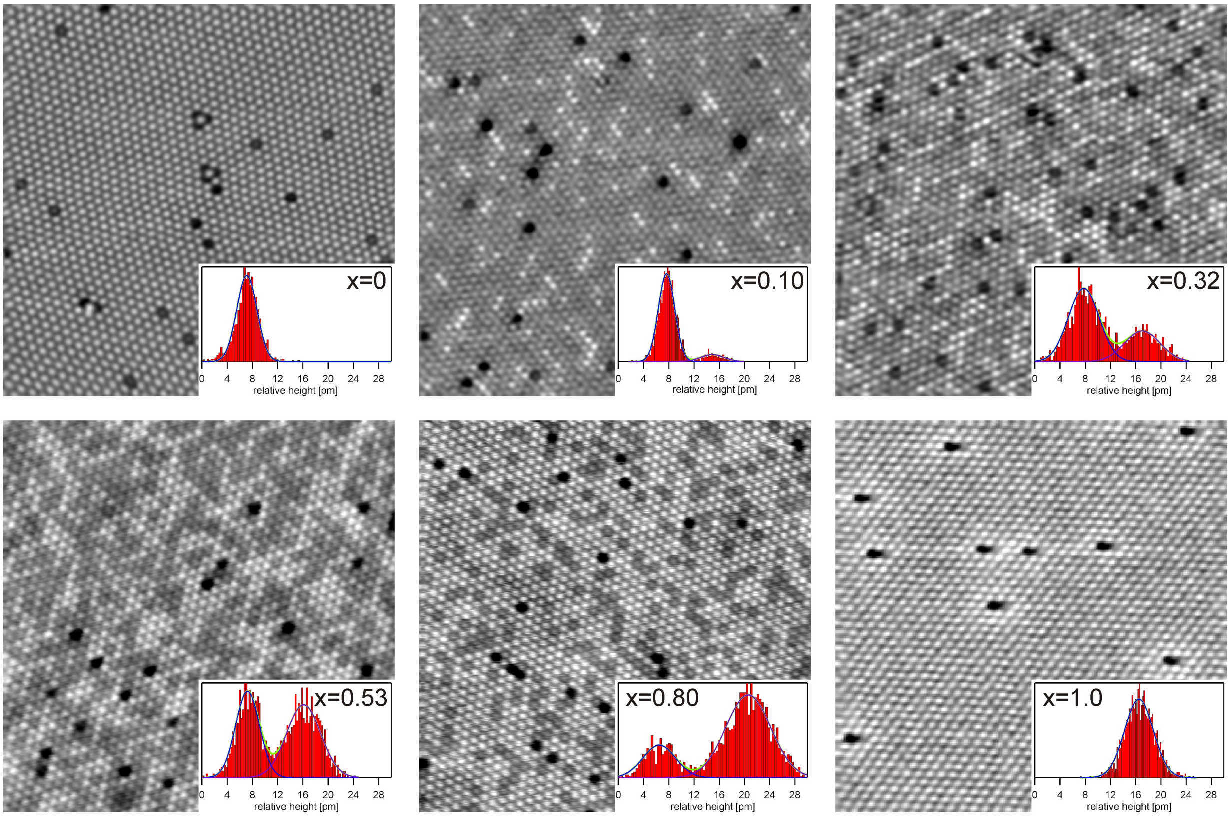

Figure 5.2: Topographic images of $Bi_xPb_{1-x}/Ag(111)$ for different alloy ratios x. All topographies have a size of $20 \times 20\,\mathrm{nm}$ and were measured at $3\,\mathrm{mV}$, $7.0\,\mathrm{nA}$. The insets shows the height distributions of the alloy atoms. For the mixed surface alloys ($x \neq 0, 1$), two gauss distributions of atom heights are found which can be attributed to the different components of the alloy. The number of higher atoms in the mixed alloys which are attributed as Bi atoms increases with the proportion of Bi to Pb that was evaporated on the surface. The exact alloy ratio x was calculated from the topographic data.

for several different ratios are displayed in Fig. 5.2. The surface alloy was found as a continuous structure over hundreds of nm, with areas of the overlayer phase of different size at the step edge to the next lower terrace (see section 7.2.1). As for the pure surface alloys only the outward relaxed alloy atoms, forming again the $\sqrt{3} \times \sqrt{3}\,\mathrm{R}30^\circ$ reconstruction with a distance of 5 Å in between them, are resolved in the STM images. In the images for all alloy ratios there are lattice sites where alloy atoms are missing (single vacancies) or, more rarely, were one alloy atom sits at an shifted lattice position (triple vacancy, here seen only in the topography for x=0). The triple vacancies are a good hint that these are indeed vacancies and not some other sort of atom sitting at the respective lattice site, as in this case the position of the substitutional atom is shifted compared to the surrounding lattice. The relaxation of the substitutional atoms was again extracted from the measurements using the depth of the vacancies. The apparent depth of these vacancies was determined for the pure surface alloys with $43 \pm 3\,\mathrm{pm}$ for Bi/Ag(111) (x=1) and $32 \pm 8\,\mathrm{pm}$ for Pb/Ag(111) (x=0) with respect to the average height of the alloy atoms. This result follows the trend of the relaxation determined in IV-LEED measurements ($65 \pm 10\,\mathrm{pm}$ and $46 \pm 6\,\mathrm{pm}$, respectively) [51].

In contrast to the pure surface alloys, atoms with two different apparent heights can be distinguished in the topographies besides the vacancies. This is also clearly demonstrated in the respective atom height histograms (insets in Fig. 5.2). Two gaussian distributions are clearly separated, representing the two different apparent heights visible in the topographic images. As the ratio of the high to low atoms in the mixed surface alloy correlates with the ratio of Bi to Pb that was evaporated on the surface, the high atoms are attributed to Bi and the low atoms to Pb. This is further supported by the average height distance between the high and low atoms, which was found to be $11 \pm 3\,\mathrm{pm}$, correlating with the difference in relaxation measured for pure surface alloys.

In addition to the height difference of the alloy atoms, there is an additional faint difference in the apparent height on a larger length scale visible in the image for $x = 0.80$. This can also be seen in the wider height distribution found for this concentration and indicates local variations in the electronic structure at the energy of 3 meV, corresponding to the voltage at which the image was measured. This variation of the electronic structure will be further discussed in section 6.1.

To study the spatial distribution of the substitutional atoms in the alloy layer, one can examine the short range ordering. From the topographic images in Fig. 5.2, one can clearly see that the distribution of the Bi and Pb atoms in the $\sqrt{3} \times \sqrt{3}\,\mathrm{R}30^\circ$ lattice structure

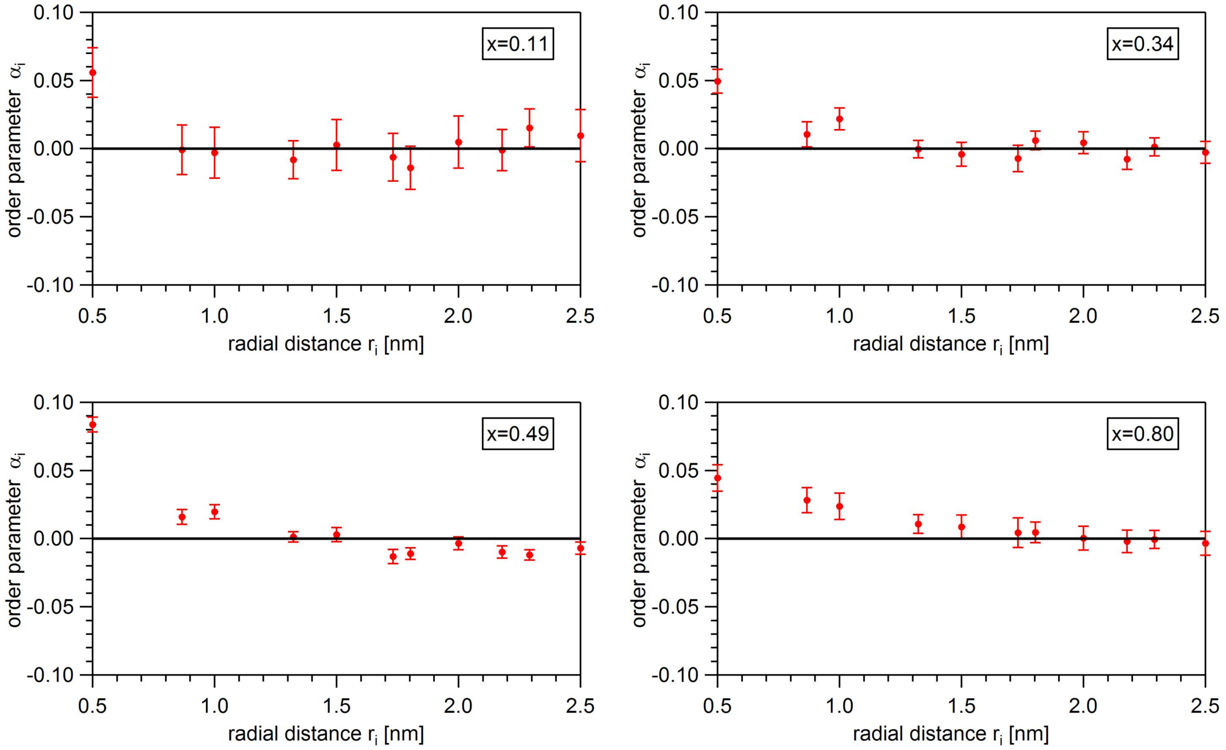

Figure 5.3: Order parameters from STM measurements for the first 11 neighbor orders for different global alloy ratios. All plots show a small short range ordering for the nearest neighbors, but drop quickly to zero for higher orders.

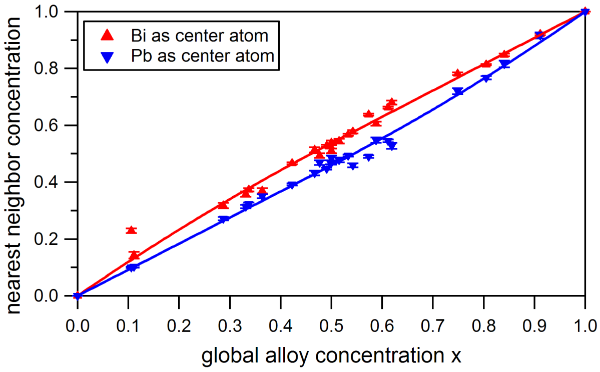

Figure 5.4: a) Experimentally extracted nearest neighbor ratio in $Bi_xPb_{1-x}/Ag(111)$ as function of the global alloy concentration x. The solid lines are fitted curves using model functions found in Monte-Carlo simulations.

shows no regular pattern (which would indicate long range ordering) but is inhomogeneous and atoms of the same kind seem to form clusters. This is confirmed by the order parameters α_i displayed in Fig. 5.3 showing that the alloys are indeed not purely random. The order parameters for the first few orders are positive and drop continuously to 0, indicating that there is a weak short range ordering effect in form of a small decomposition (preference of nearest neighbors of the same kind). This decomposition leads to the formation of small clusters. The average concentration found in the nearest neighbors of either Bi atoms or Pb atoms is plotted in Fig. 5.4 as a function of the global alloy concentration. The splitting of the nearest neighbor concentration into two curves depending on the center atom further illustrates the effect of the short range ordering.

5.2.2 Topographic structure of $Bi_xSb_{1-x}/Ag(111)$

The mixed surface alloy $Bi_xSb_{1-x}/Ag(111)$ was also studied with STM for different alloy concentrations x, displayed in Fig. 5.5. As in the case of $Bi_xPb_{1-x}/Ag(111)$, the two different substituents can be clearly distinguished in the STM topographies and the atom height histograms. The average apparent height difference was found to be 47 ± 5 pm, comparable with the height difference of 55 ± 10 pm expected from the IV-LEED measurements [51]. So, again the high atoms can be assumed to be Bi atoms, and lower ones to be Sb atoms. The distribution of the substitutional atoms appears to be similar, again a disordered structure with no long range ordering observable. However, there are also differences between the two systems, as no vacancies are found even for high Bi concentrations. In addition it was possible to the change the alloy concentration by evaporating

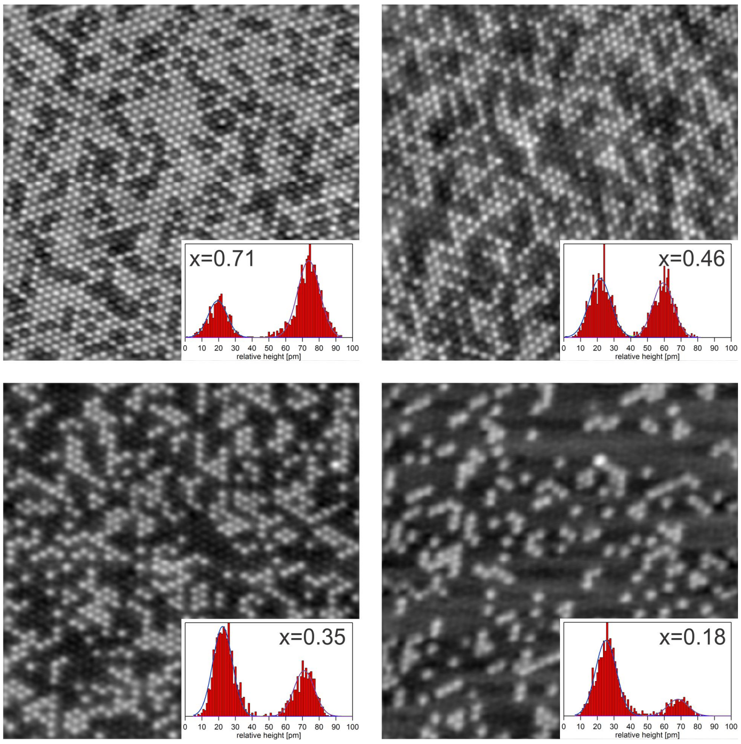

Figure 5.5: Topographic images of Bi$_x$Sb$_{1-x}$/Ag(111) for different alloy ratios x. All topographies have a size of 20×20 nm and were measured at 3 mV, 7.0 nA. The insets shows the height distributions of the alloy atoms. As in the case of Bi$_x$Sb$_{1-x}$/Ag(111) two gauss distributions of atom heights are found which can be attributed to the different components of the alloy. The exact alloy ratio x was calculated from the topographic data.

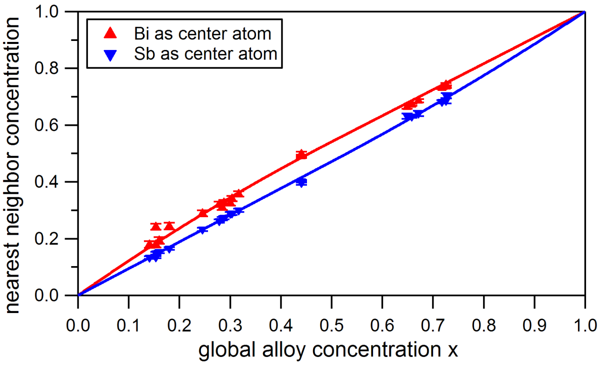

Figure 5.6: a) Experimentally extracted nearest neighbor ratio in $\mathrm{Bi}_x\mathrm{Sb}_{1-x}$/Ag(111) as function of the global alloy concentration x. The solid lines are fitted curves using model functions found in Monte-Carlo simulations.

an additional amount of Sb on an surface alloy with 1/3 ML coverage. The surface alloys displayed in Fig. 5.5 were prepared by successive evaporation of additional Sb (each time approximately 1/12 ML) on a pure Bi/Ag(111) surface alloy at a sample temperature of at 300°C. For surface alloys with higher Sb concentration formed by this method, areas of the pure Bi monolayer phase is found (see section 7.2.3).

As it was the case for $\mathrm{Bi}_x\mathrm{Pb}_{1-x}$/Ag(111), the topographies of $\mathrm{Bi}_x\mathrm{Sb}_{1-x}$/Ag(111) in Fig. 5.5 indicate a clustering of atoms of the same kind (positive short range ordering). This is confirmed by the nearest neighbor concentration displayed in Fig. 5.6, separately plotted for nearest neighbors of Bi or Sb atoms.

5.3 Monte-Carlo Simulations

Monte-Carlo method can be used to simulate the distribution of the alloy atoms depending on the temperature and the interaction energies between the different components. The simulations are implemented in a two dimensional hexagonal lattice corresponding 40 × 40 atoms. Periodic boundary conditions are used for atoms at the edge of the lattice. The components of the alloy will be distinguished as "high" atoms (bright lattice points, corresponding to Bi) and "low" atoms (dark lattice points, corresponding to Pb and Sb). In accordance with the experimental data, the concentration will be given as the fraction of high atoms.

For the simulation the Metropolis algorithm with a positive effective pair interaction energy ΔJ (see Eq. 3.30) value will used to simulate a positive short range ordering (preference of nearest neighbors of the same kind), which is indicated in the STM measurements especially for balanced alloy concentrations. As the freezing temperature for the movement of the substitutional atoms in the widespread surface alloy is not known, the preparation temperature of 300°C is used in the simulations.

In the following analysis, only the nearest neighbor interaction will be studied further. In principle, the energetics for such ordering can be calculated for a individual ratios using the inverse Monte-Carlo Method [77] which has also been applied to STM measurements [78]. Here instead, a combined analysis for the whole ratio range will be used, comparing the behavior of the measured alloy structures with normal Monte-Carlo simulations.

5.3.1 MC simulation of the mixed surface alloy

Fig. 5.7 shows the result of such an Monte-Carlo simulation for an alloy structure with a concentration of $x = 0.5$ and $\Delta J = 20\,\mathrm{meV}$. Starting from a random distribution as displayed in Fig. 5.7 a), after 1000 MC steps (corresponding in this case to $1.6 \cdot 10^6$ tests of the Metropolis condition Eq. 3.28 for individual lattice site pairs) an alloy structure with a distinct clustering is formed in Fig. 5.7 b). The evolution of the nearest neighbor concentration difference displayed in Fig. 5.7 c) shows the transition from the random distribution with a concentration difference of 0 to the thermal equilibrium, for which entropy and the nearest neighbor interaction cancel each other as driving forces. As there are thermal fluctuations of the concentration difference, the results of several of the MC Steps are used to determine an average value. To make sure that the system is in thermal equilibrium (which can take more MC steps for higher ΔJ, approximately 800 MC steps for $\Delta J = 50\,\mathrm{meV}$), only the last 20% of the MC steps are used in the average, as marked by the shaded area.

From Fig. 5.7 b) it is obviously the effective pair interaction ΔJ in the simulation is stronger than in the surface alloys displayed in Fig. 5.2 and Fig. 5.5. However with a somewhat higher ΔJ the evolution of the nearest neighbor concentration can be better illustrated. 5.7 d) shows simulation results of the nearest neighbor concentrations for different center atoms as function of the global concentration of high atoms. If the center atom is a majority atom (Pb for $x < 0.5$ or Bi for $x > 0.5$), the nearest neighbor ratio can be approximated by a linear function of the ratio, while for a minority atom it shows an approximately parabolic behavior. This behavior can be plotted using only one parameter δ, the difference in the nearest neighbor concentration at $x = 0.5$ as displayed in Fig. 5.7 d). The fit functions $f_{\mathrm{lin}}(x)$, $f_{\mathrm{para}}(x)$ ($g_{\mathrm{lin}}(x)$, $g_{\mathrm{para}}(x)$) for a high (low) atom as center

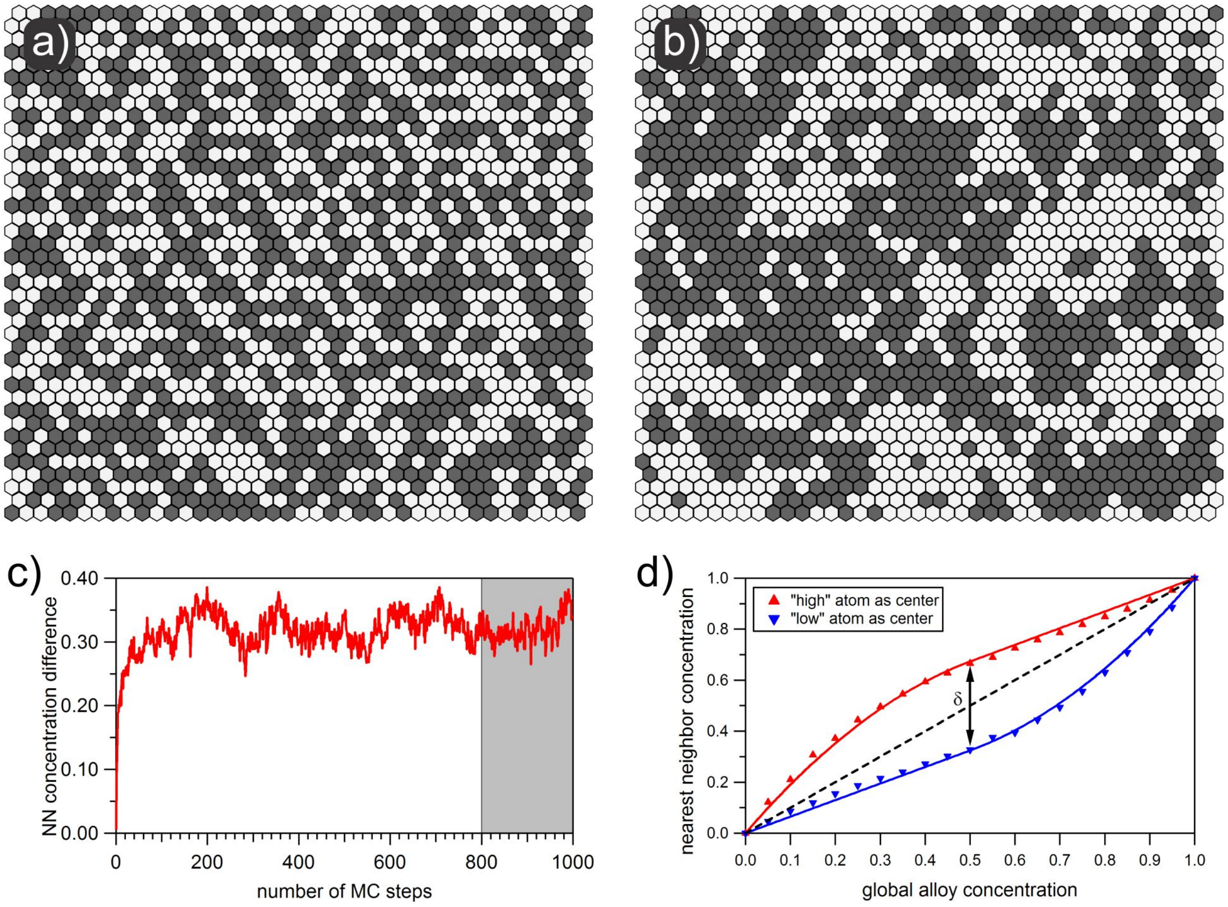

Figure 5.7: a) 40×40 alloy structure with randomly distributed atoms for a concentration $x = 0.5$. b) The alloy structure after 1000 MC steps with the structure displayed in a) as starting points. As parameters for the Metropolis function 3.28 $T = 573\,K$ and $\Delta J = 20\,\mathrm{meV}$ were used. c) Evolution of the nearest neighbor concentration difference during the Monte-Carlo simulation leading to the alloy structure displayed in b). d) Simulation of the nearest neighbor concentrations as function of the global Bi concentration for the same parameters as b). The difference δ gives the maximal concentration difference found at $x = 0.5$, which is used for the comparison with the experimental data.

used in the fit for the linear and parabolic part respectively, can be found by stating the following conditions:

$$f_{\text{para}}(0) = g_{\text{lin}}(0) = 0 \tag{5.1}$$

$$f_{\text{lin}}(1) = g_{\text{para}}(1) = 1 \tag{5.2}$$

$$f_{\text{lin}}(0.5) = f_{\text{para}}(0.5) = 0.5 + 0.5\delta \tag{5.3}$$

$$g_{\text{lin}}(0.5) = g_{\text{para}}(0.5) = 0.5 - 0.5\delta \tag{5.4}$$

In addition, the functions should be continuously differentiable, especially at the transition from linear to parabolic behavior, leading to the conditions for the first derivatives

$$f'_{\text{para}}(0.5) = f'_{\text{lin}}(0.5) \tag{5.5}$$

$$g'_{\text{para}}(0.5) = g'_{\text{lin}}(0.5) \tag{5.6}$$

With this there are enough conditions to define the functions (two conditions for the linear functions and three conditions for the parabolic functions), and they can be found as

$$f_{\text{lin}}(x) = (1-\delta)\cdot x + \delta \quad \text{for } 0.5 \leq x \leq 1 \tag{5.7}$$

$$g_{\text{lin}}(x) = (1-\delta)\cdot x \quad \text{for } 0 \leq x \leq 0.5 \tag{5.8}$$

$$f_{\text{para}}(x) = -4\delta x^2 + (1+3\delta)x \quad \text{for } 0 \leq x \leq 0.5 \tag{5.9}$$

$$g_{\text{para}}(x) = 4\delta x^2 + (1-5\delta)x + \delta \quad \text{for } 0.5 \leq x \leq 1 \tag{5.10}$$

These functions have been fitted to the simulated data in Fig. 5.7 d) and plotted as solid lines.

5.3.2 Comparison with experimental data

With the single parameter model described by Eq. 5.7 to Eq. 5.10, a direct comparison can be made between Monte-Carlo simulations and the experimental results can be made. The single parameter model allows on the experimental side to include data with different concentration for the determination of δ while for the simulations the ΔJ series has to be calculated for only one concentration to determination of the effective pair interaction for the two mixed surface alloys. Two series of Monte-Carlo simulations were performed for an global alloy concentration $x = 0.5$ and ΔJ in the range from 0–50 meV and 0–10 meV respectively.

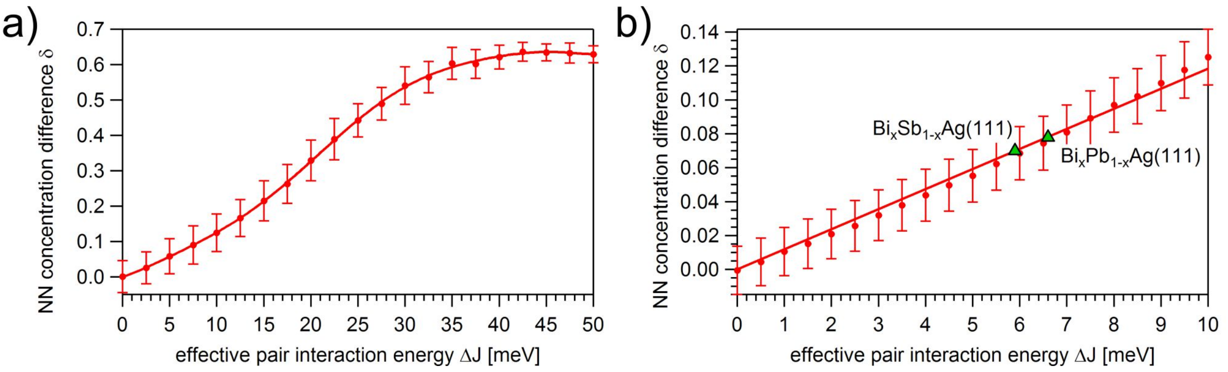

Figure 5.8: Nearest neighbor concentration difference at $x = 0.5$ as function of the effective pari interaction energy ΔJ from a series of Monte-Carlo simulations. In the overview graph a) the solid line is a guide to the eye. In the graph with higher resolution b), the solid line represents the linear fit used for the comparison with the experimental data. The green triangles represent the actual results found for the mixed surface alloys in the comparison.

Fig. 5.8 a) shows δ as a function of ΔJ over the larger range from 0–50 meV. For each data point of this series, the results of 10 simulation with different random starting configurations were averaged. δ rises at first linearly but it saturates at approximately δ=0.65. For the comparison with the experimental data a second series was calculated in smaller energy range and higher resolution as displayed in Fig. 5.8 b). To reduce statistical fluctuations further, in this series the results of 100 individual simulations with random starting configurations were averaged for each data point. In this ΔJ range, the resulting δ curve shows an approximately linear behavior. A linear fit gives slope of $11.85 \pm 0.60\,\mathrm{eV}^{-1}$.

Fitting the model to the experimental data in Fig. 5.4 and Fig. 5.6, a nearest neighbor concentration difference $\delta = 0.078 \pm 0.010$ for $\mathrm{Bi}_x\mathrm{Pb}_{1-x}$/Ag(111) and $\delta = 0.070 \pm 0.007$ for $\mathrm{Bi}_x\mathrm{Sb}_{1-x}$/Ag(111) was found. Comparing these results with the simulated δ curve gives for $\mathrm{Bi}_x\mathrm{Pb}_{1-x}$/Ag(111) an effective pair interaction energy $\Delta J = 6.6 \pm 1.2\,\mathrm{meV}$, and for $\mathrm{Bi}_x\mathrm{Sb}_{1-x}$/Ag(111) $\Delta J = 5.9 \pm 0.9\,\mathrm{meV}$.

5.4 Discussion

The different height relaxation of the substitutional atoms Bi, Pb and Sb allows to clearly identify them in the STM topographies of the mixed surface alloys $\mathrm{Bi}_x\mathrm{Pb}_{1-x}$/Ag(111) and $\mathrm{Bi}_x\mathrm{Sb}_{1-x}$/Ag(111). In addition, even for the comparatively small relaxation of Sb, a distinction to vacancies in the substitutional lattice where the respective Ag atom was not replaced by a substitutional atoms, is possible. This allows to measure an absolute value

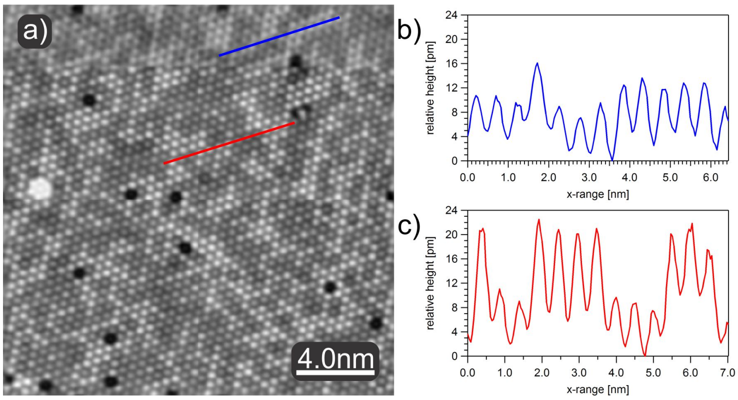

Figure 5.9: a) Topographic image of $Bi_{0.53}Pb_{0.47}$/Ag(111) measured at 3 mV, 7.0 nA. The scan direction was upwards, with a tip change near the end of the scan. b) Line profile marked by the blue line in the image a) after the tip change. c) Line profile marked by the red line before the tip change.

of the relaxation even if the coverage with the surface alloys is complete and there is no clean Ag(111) surface available for comarison. However, when comparing the relaxation of the substitutional atoms determined from the STM topographies with IV-LEED measurements, one has to keep the differences of the experimental methods in mind, which make a direct quantitative comparison difficult. In the STM measurements, there is the influence of the tip as well as the electronic structure of the sample. Tip changes can change the apparent height and measured height difference as illustrated in Fig. 5.9. While the tip retains the atomic and chemical resolution, the height contrast between the Bi and Pb atoms is reduced. Even though tips were treated to achieve a strong height contrast between the different substitutional atoms, a influence on the measurement by the tip resulting in a smaller height difference cannot be excluded. Furthermore, while IV-LEED is a scattering technique with which the center of the atoms are probed, in STM the surrounding electron orbitals are probed, so that the radius of the atoms must be taken into account. Looking at the empirical radius as compiled by Slater [79], one finds that Pb has with 180 pm a larger radius as Bi with 160 pm, which can be explained by the higher core charge of Bi. With this estimation one can assume, that the larger atom radius of Pb partially compensates the height difference. On the other hand, Sb (145 pm radius) is smaller than Bi, leading to an overestimation of the height difference which might be compensated by the tip influence discussed above. On the other hand, with IV-LEED, the atomic structure is not measured directly. Instead, different model structures are used for simulations of the measured I-V curves with the goal to reproduce the measurements as close as possible.

Still, finding the same trend for the relaxations in the STM measurements and the IV-LEED simulations further supports the models used in these simulations and the result of an increase of the Rashba splitting with increased relaxation [51]. The result stands in contrast to theoretical calculations, which predict a higher relaxation for Pb compared to Bi [60, 80]

Both mixed surface alloys show a very similar structure varying only in minor details as the nearest neighbor interaction energy, leading to a smaller clustering effect in $\mathrm{Bi}_x\mathrm{Sb}_{1-x}$/Ag(111). The absence of a dependence of the substitutional atom relaxation on the concentration as well as the fact that the relaxation differences are comparable to what is expected from the IV-LEED measurements of the pure surface alloys [51] indicates that there is no influence on the relaxation by different neighbor in the substitutional lattice. The different growth behavior of $\mathrm{Bi}_x\mathrm{Sb}_{1-x}$/Ag(111)with the substitution of Bi by Sb indicates that Sb is preferred to Bi as substitutional atoms, while such a differentiation was not observed for Bi and Pb.

The presence of vacancies in most of the surface alloys can be attributed to the higher sample temperature used for the preparation. In studies of the Pb/Ag(111) with a comparable preparation temperature (annealing at 250°C after the deposition [50]), similar defects can be found, while in other works with lower preparation temperatures (below 200°C [27, 59]), these vacancies do not seem to appear. At high enough temperatures, the substitutional atoms seem to desorb again and when no further atoms are adsorbed on the surface either during sample cooldown after evaporation or during post-annealing, vacancies are formed. Even in the presence of an excess of substitutional atoms in form of a nearby monolayer phase, these vacancies are found. This indicates that the mobility of Bi and Pb in the widespread surface alloys is not high enough to fill these vacancies even though they are mobile at low concentrations ($\ll$1/3 ML) indicated by the formation of cluster at room temperature for Pb/Ag(111) [50]). A possible explanation for this is the fact that a substitutional atom moving from one substitutional lattice site to another with a vacancy has to exchange its place twice with an Ag atom, the first sitting at an off-lattice site. In the presence of large atoms (Bi, Pb) at surrounding lattice sites, the off-lattice site is unfavorable, decreasing the chance for an exchange. In the presence of Sb atoms which are even smaller than Ag, the off-lattice sites might not be so unfavorable (even though the substitutional lattice sites are obviously still preferred) and movement of the substitutional atoms has a higher probability. This would explain the absence of vacancies in the case of $\mathrm{Bi}_x\mathrm{Sb}_{1-x}$/Ag(111), where excess of Bi is present in the form of the monolayer phase. In the case of pure Sb/Ag(111) no excess atoms are available at these high preparation temperatures and so the vacancies formed after the evaporation cannot be filled. The absence of excess atoms in form of a monolayer phase for Sb/Ag(111) is in agreement with LEED and Auger measurements [81], which found a coverage saturation of 0.6 atomic layer (corresponding to 1/3 ML on the Ag(111) surface) and a $\sqrt{3} \times \sqrt{3}\,\mathrm{R}30^\circ$ reconstruction when grown at 275°C.

For the nearest neighbor concentration difference displayed in Fig. 5.8 a), one could assume, that an increase in the effective pair interaction energy ΔJ leads to a stronger decomposition of the alloy components until a complete separation with $\delta \approx 1$ is reached (due to the interface between the two components $\delta = 1$ can only be reached for in infinite system when the interface becomes insignificant compared to the volume). However as the two components become more and more separated, the distance between areas of the same component become too large and the thermal fluctuations do not suffice anymore to combine these separated areas in a finite time. Only higher temperatures (and consequently stronger thermal fluctuations) would lead to a further separation.

As the $\sqrt{3} \times \sqrt{3}\,\mathrm{R}30^\circ$ alloy lattice is embedded into the Ag host lattice, a nearest neighbor interaction between substitutional atoms is actually a next nearest neighbor interaction. Similarly, the next nearest neighbor interaction of the substitutional atoms is actually a fifth order neighbor interaction. So it is not surprising that the short range order parameters drop quickly to zero for higher orders. The nearest neighbor interaction energy for the substitutional lattice is comparable to the next nearest neighbor interaction energy found for the binary surface alloy $\mathrm{Au}_x\mathrm{Pt}_{1-x}$/Pt(111) [82], which shows a similar behavior as the mixed surface alloys examined here. Especially the nearest neighbor ratio for this system behaves as described approximately by Eq. 5.7 to 5.10.

5.5 Conclusion

In this chapter the first measurements of the local structure of the mixed surface alloys $\mathrm{Bi}_x\mathrm{Pb}_{1-x}$/Ag(111) and $\mathrm{Bi}_x\mathrm{Sb}_{1-x}$/Ag(111) were presented. In addition to the atomic resolution of the substitutional atoms, also chemical resolution was possible, allowing to distinguish the different substitutional elements in the alloy. This chemical resolution allowed to study the distribution of the substitutional atoms. A small clustering effect was found, indicating an attractive interaction between substitutional atoms of the same kind. Comparing the experimentally found distribution of the substitutional atoms with Monte-Carlo simulations, it was possible to determine the strength of effective pair interaction.

Even though both $\mathrm{Bi}_x\mathrm{Pb}_{1-x}/\mathrm{Ag}(111)$ and $\mathrm{Bi}_x\mathrm{Sb}_{1-x}/\mathrm{Ag}(111)$ have a similar topographic structure, differences in the growth behavior was found. Theoretical studies of the growth dynamics of these and similar systems might give further insight into these differences.

Based on the findings here, one can expect that it is possible to distinguish the substitutional atoms in the related surface alloy $\mathrm{Pb}_x\mathrm{Sb}_{1-x}/\mathrm{Ag}(111)$ and especially in the highly interesting ternary surface $\mathrm{Bi}_x\mathrm{Pb}_y\mathrm{Sb}_{1-x-y}/\mathrm{Ag}(111)$ [20, 60]. The almost identical topographic structure of these systems in combination with the different electronic properties found for the pure surface alloys makes them ideal systems for the study of electronic properties of disordered structures, such as Anderson localization. Variations of the chemical components of the surface alloy either by changing the concentration x or completely exchanging one element of another without general changes in the topographic structure opens the way for experimental studies of the influence of different parameters such as disorder potential or Rashba splitting on the Anderson localization of electronic waves.

Chapter 6

Anderson Localization in the mixed surface alloys

6.1 Electronic structure of $\mathrm{Bi}_x\mathrm{Pb}_{1-x}$/Ag(111)

6.1.1 STS measurements on Pb/Ag(111), Bi/Ag(111) and Sb/Ag(111)

DFT calculations predict a total of four states mostly localized in the surface layer of Bi/Ag(111) which are so shifted to higher energies in Pb/Ag(111) [80]. They are labeled by their predominant character (with increasing energy) as sp_z, p_{xy} $(m_j = 1/2)$, p_{xy} $(m_j = 3/2)$ and p_z. In STS measurements of Pb/Ag(111) and Bi/Ag(111), all four states can be identified (see Fig. 6.1). As illustrated, these two spectra define the energy range through which the states of $\mathrm{Bi}_x\mathrm{Pb}_{1-x}$/Ag(111) shift with changing ratio x. When shifting to higher energies, the peaks become weaker and it is more difficult to measure them with STS. This can be explained that for higher energies, the projected band gap closes and the states interact with bulk bands. The increasing influence of these bulk bands can be seen in the background signal of the dI/dV-spectra, which becomes stronger for larger voltages (see e.g. Fig. 6.1).

Also for Sb/Ag(111) the STS spectra are in agreement with the DFT calculations [83]. The onset of the sp_z state was found at $-0.35\,\mathrm{eV}$ at somewhat larger energies than $-0.27\,\mathrm{eV}$ determined from ARPES measurements [83]. The predicted splitting of the $p_{(x,y)}$-band into $m_j = 1/2$ and $m_j = 3/2$ states could not be resolved for the pure surface alloy. However, following the DFT calculations, the energy of the $m_j = 1/2$ state should be approximately

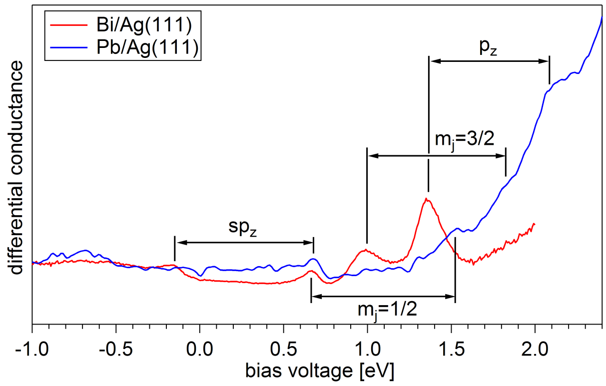

Figure 6.1: STS spectra of the pure surface alloys Pb/Ag(111) and Bi/Ag(111). All four states predicted by DFT calculations can be seen. In addition, the energy range through which the states of Bi_xPb_{1-x}/Ag(111) shift with changing ratio x are marked. [80].

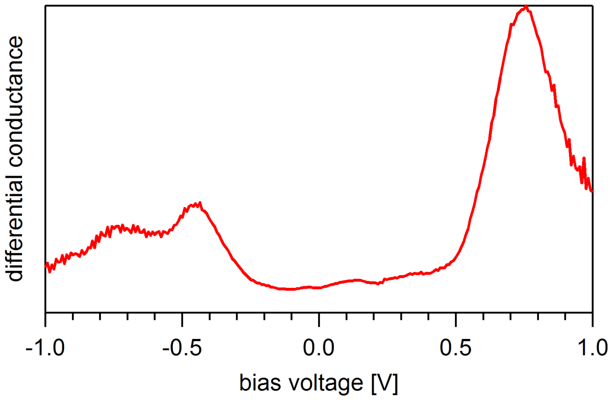

Figure 6.2: STS spectrum of the pure surface alloys Sb/Ag(111). In the case of the pure surface alloy it was not possible to resolve the different $p_{(x,y)}$ states as predicted by theoretical calculations.

state	Bi/Ag(111)	Pb/Ag(111)	Sb/Ag(111)
sp_z	-0.13 eV	0.71 eV	-0.35 eV
$m_j = 1/2$	0.68 eV	1.56 eV	0.67 eV*
$m_j = 3/2$	1.07 eV	1.85 eV	0.91 eV*
p_z	1.41 eV	2.16 eV	n/a

Table 6.1: Band onsets of the pure surface alloys as determined from the STS measurements except for the marked values (*), which could not be resolved separately be and for which values from DFT calculations are given.

0.67 eV and 0.91 eV for the $m_j = 3/2$ state, both energies lying well inside the single peak seen in the STS spectrum. For Sb/Ag(111) no p_z-peak could be observed up to an energy of 2.0 eV. As the shift of the onset energies from Sb/Ag(111) to Bi/Ag(111) is very small and the evolution of at least the sp_z-band in $\mathrm{Bi}_x\mathrm{Sb}_{1-x}$/Ag(111) from $x = 0$ to 1 is known to have a parabolic instead of a monotone character [20], it is not possible to discern the respective energy range from the STS spectra of the pure surface alloys as it was done for $\mathrm{Bi}_x\mathrm{Pb}_{1-x}$/Ag(111).

An overview of the band onsets for the three pure surface alloys is given in table 6.1.

6.1.2 Local STS measurements on $\mathrm{Bi}_x\mathrm{Pb}_{1-x}$/Ag(111)

An example STS spectrum measured at different locations of a $\mathrm{Bi}_{0.80}\mathrm{Pb}_{0.20}$/Ag(111) mixed surface alloy is shown in Fig. 6.1. Again four peaks representing the four states can be seen in energy regions limited by the peaks seen in the STS spectra of Bi/Ag(111) and Pb/Ag(111) 6.1. A striking feature of the STS spectra is the fact that for all four states there is a similar energy shift. From ARPES measurements it is known, that there is a band shift with changing global concentration [19], so variations in the alloy structure might change the electronic structure on a local scale. Assuming that the electrons only see a limited area of the alloy, one can calculate an effective alloy concentration that the electron sees and that defines the shift of the band onset. As an example, the inset in Fig. 6.3 b) shows the effective alloy concentration as a function of the effective radius r_{eff} for an alloy influence dropping exponentially with the distance, defined as

$$x(\vec{r}) = C \cdot \sum_i \exp\left[-\frac{|\vec{r} - \vec{r}_i|}{r_{\text{eff}}}\right] \cdot x_i \tag{6.1}$$

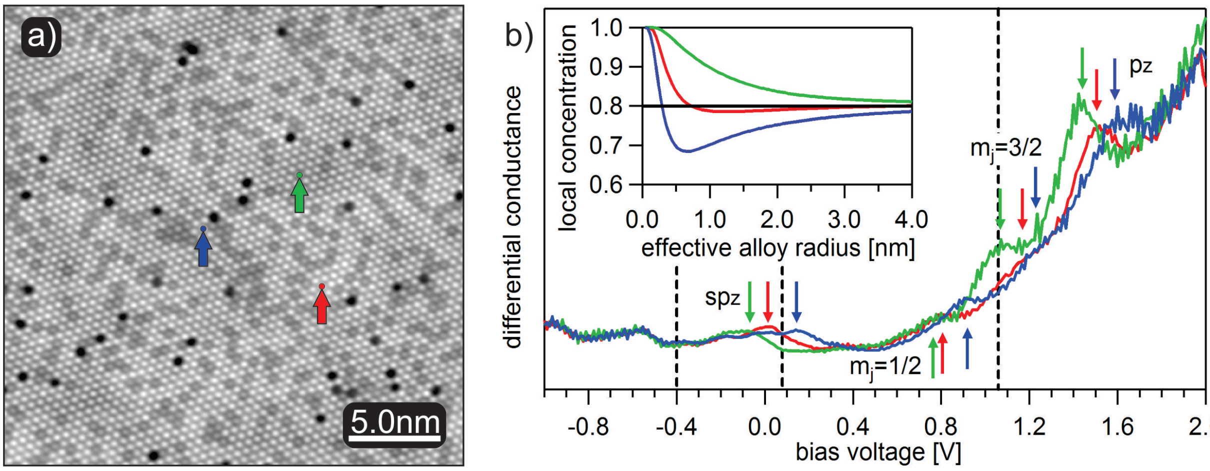

Figure 6.3: a) STM image of $\mathrm{Bi}_{0.80}\mathrm{Pb}_{0.20}/\mathrm{Ag}(111)$ measured at 3 mV, 7.0 nA. b) STS spectra for different locations as marked in a). For the STS measurements, the tip was stabilized at -1.0 V, 1.0 nA. The shifting features visible in the spectra (marked with arrows in the respective color) represent surface states with different orbital character. The dashed lines mark the voltages at which the dI/dV-maps 6.8 b)–d) were measured. The inset shows the evolution of the local concentration at the marked locations as function of effective alloy radius for exponentially localized states.

Here, x_i is 0 (1) for an Pb (Bi) atom at position $\vec{r}_i$, C is a normalization constant given by $C^{-1} = \sum_i \exp\left[-\frac{|\vec{r}-\vec{r}_i|}{r_{\mathrm{eff}}}\right]$ and the sum goes over all atoms. Comparing now the local concentration curves with the energy shift, one can see, that there is a correlation, as for a higher Bi concentration, the states shift to lower energy as expected from spectra of the pure surface alloys. The same effect can be seen for other concentrations. In Fig. 6.4 a), the energy of the four states are plotted as functions of the overall concentration. The variation of state energy for measurements at different locations on the same sample can be seen as a vertical spreading of the data points. A continuous behavior of the state energies with respect to the concentration can be seen when they are plotted as function of the effective local concentration (Fig. 6.4 b)). Assuming an effective alloy radius which is independent of the concentration, for each state the effective alloy radius was optimized so that the data points follow a parabolic fit as close as possible, as such a parabolic dependence is in principle possible (see [20]). The effective alloy radii for the individual states are 1.04 nm for the sp_z-state, 0.96 nm for the $m_j = 1/2$-state, 0.68 nm for the $m_j = 3/2$-state and 0.88 nm for the p_z-state.

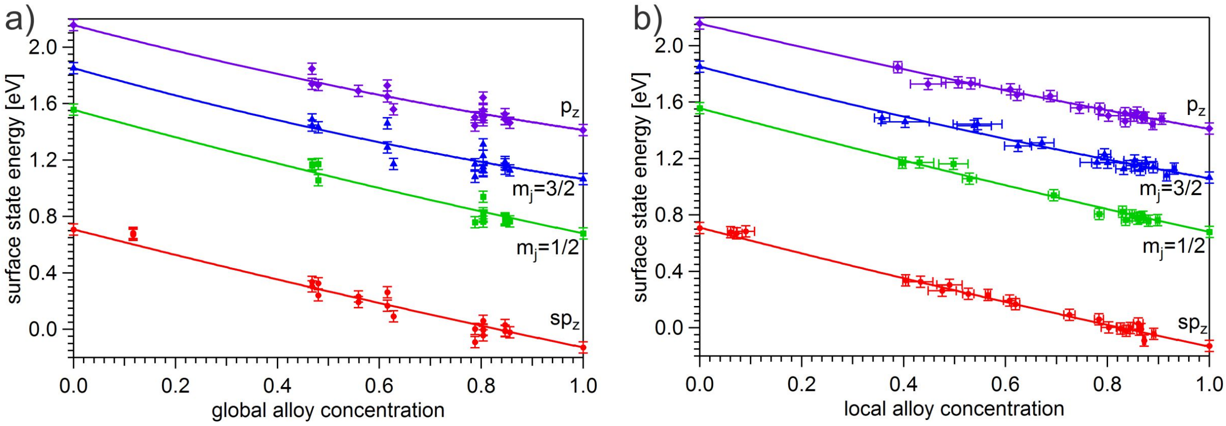

Figure 6.4: (a) Energies of the four states localized in the surface alloy layer as function of the global alloy concentration. (b) The same plot as a function of an effective, local alloy concentration seen by exponentially localized states. Assuming an alloy radius independent of the concentration, for each state an effective alloy radius was determined so that the data points show an continuous shift from pure Pb/Ag(111) ($x = 0$) to pure Bi/Ag(111) ($x = 1$) as best as possible.

6.1.3 Spatial Distribution of the Electronic Structure in $Bi_xPb_{1-x}/Ag(111)$

To study the spatial distribution of the states in the disordered surface layer, dI/dV-maps were measured for energies at the edges of the peaks generated by the singularities at the band onset. The energy of 1.06 eV of the dI/dV-map displayed in Fig. 6.5 b) is marked by the right dashed line in Fig. 6.3 b). The spatial variation in the intensity of the dI/dV signal can be ascribed to an energy shift of the $m_j = 3/2$ state: In areas with many Pb atoms (darker atoms in the topography 6.5 a)) the intensity is lower (blue areas in the dI/dV-map 6.5 b)) as the state shifts to higher energy towards the situation of pure Pb/Ag(111) and less of it is seen by the dI/dV-signal. So the dI/dV-map gives a spatially resolved measure of the energy shift of the states as seen in the STS spectra.

One can now again study the correlation between the energy shift and the local concentration. For this, local concentration maps (Fig. 6.5 c) to f)) have been calculated from the topographic data for different decay functions as plotted in Fig. 6.5 g). Each local concentration map was calculated for an effective radius that gives the best quantitative agreement with the dI/dV-map for the respective decay function. To make a quantitative comparison of the dI/dV-map and the local concentration maps possible, they were normalized. This means, that the data values were shifted so that their mean is at 0 and

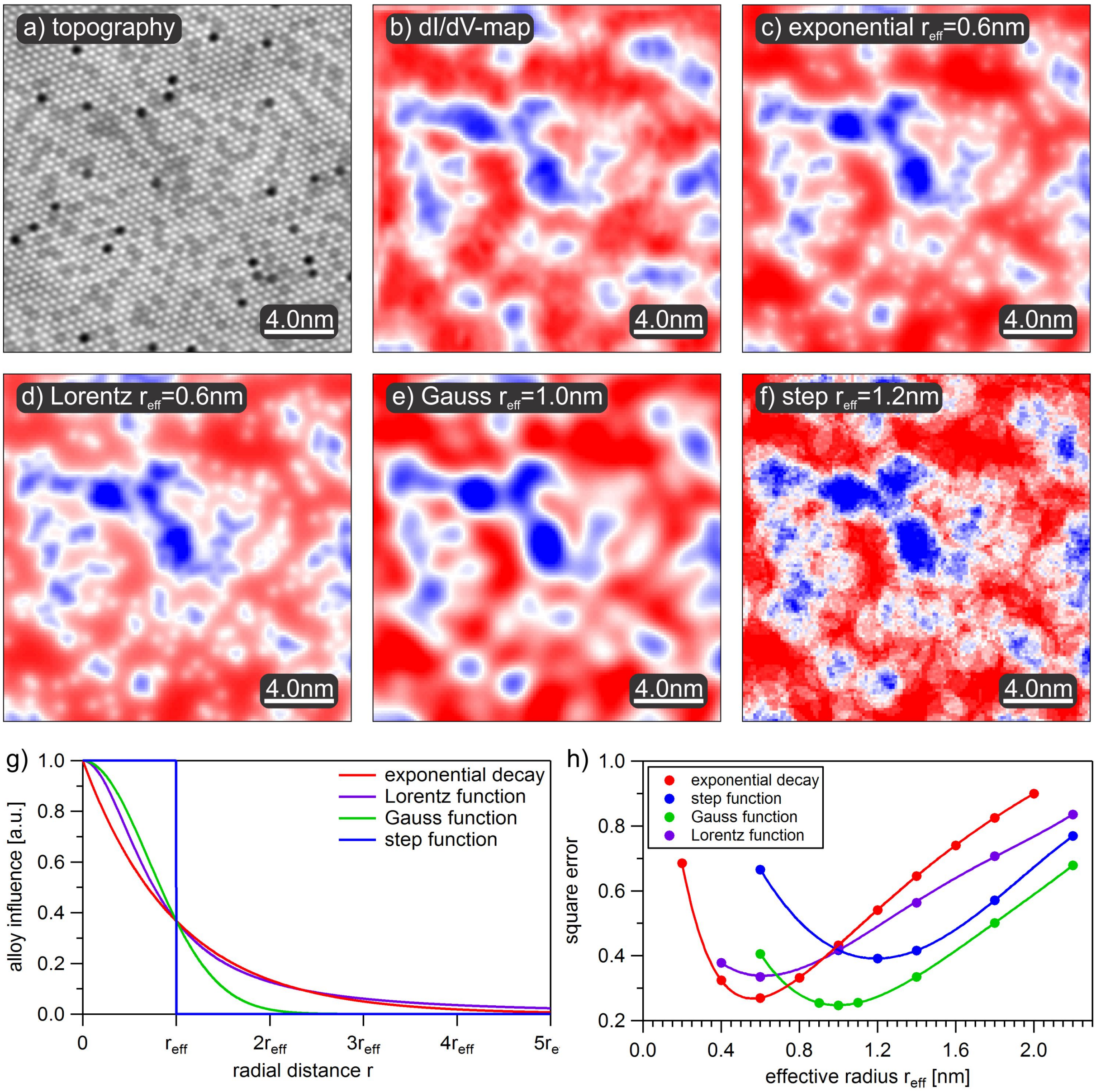

Figure 6.5: (a) Topographic structure of $Bi_{0.8}Pb_{0.2}/Ag(111)$ measured at 3 mV, 7.0 nA. b) Corresponding dI/dV-map measured at 1.06 V, 1.0 nA. The energy position at which the dI/dV-map was measured is marked by the right dashed line at the $m_j = 3/2$ state in Fig. 6.3 b). Red represents a higher intensity and blue a lower intensity of the dI/dV-signal. For comparison, local concentration maps were calculated for different decay functions: c) exponential decay function, d) Lorentz function, e) Gauss function and f) step function. g) The individual decay functions used to calculate the local concentration maps. The distance at which the function drops by factor e^{-1} is defined as effective radius e_{eff}. h) Plot of the square error between the dI/dV-map and the local concentration maps (both normalized for this calculation). The effective radii were chosen, so that the concentration map shows the best quantitative agreement with the dI/dV-map for the respective decay function. The solid lines are a guide to the eye.

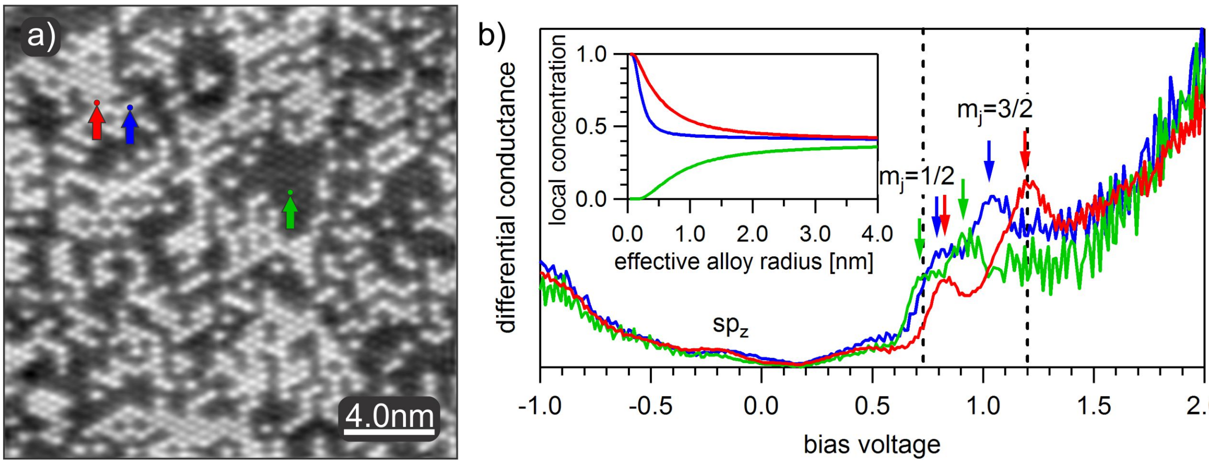

Figure 6.6: a) STM image of $\mathrm{Bi}_{0.39}\mathrm{Sb}_{0.61}$/Ag(111) measured at 3 mV, 7.0 nA. b) STS spectra for different locations as marked in a). For the STS measurements, the tip was stabilized at -1.0 V, 1.0 nA. The shifting features visible in the spectra (marked with arrows in the respective color) represent surface states with different orbital character. The inset shows the evolution of the local concentration at the marked locations as function of effective alloy radius for exponentially localized states.

rescaled for a standard deviation of 1. The average square error gained from the comparison of these normalized maps is plotted in Fig. 6.5 h). While all functions can roughly reproduce the spatial structure of the dI/dV map, only the exponential decay function and the Lorentz function reproduce the finer details of the map, with the exponential function resulting in a lower square error.

6.2 Electronic structure of $\mathrm{Bi}_x\mathrm{Sb}_{1-x}$/Ag(111)

6.2.1 Local STS measurements on $\mathrm{Bi}_x\mathrm{Sb}_{1-x}$/Ag(111)

Fig. 6.6 shows the result of local STS measurements on $\mathrm{Bi}_{0.39}\mathrm{Sb}_{0.61}$/Ag(111), with spectra taken at a position of low, medium and high Bi concentration. The spectrum high Bi concentration was measured before and after the measurement of the other two spectra to rule out any changes of tip during the measurement. Two strong features in the unoccupied states representing the $p_{(x,y)}$ band split into states with $m_j = 1/2$ and $m_j = 3/2$ character are observable. No p_z state can be seen at this concentration. As for $\mathrm{Bi}_x\mathrm{Pb}_{1-x}$/Ag(111), a correlation between the energy position of the bands and the local concentration can be seen, with an shift of the states to higher energy for higher Bi concentrations. Even though the positions for the spectra at high and medium Bi concentration are only a few lattice constants away from each other, a clear difference in the respective spectra can be seen, indicating a strong localization of the states.

6.3 Tight-Binding calculations

A possible explanation for these localized states is Anderson localization, which predicts such exponentially localized states in disordered systems. As the atomic structure of the disordered mixed surface alloy is fully known from the topography measurements and the ordered substrate should not give any spatially varying contribution on the length scale above the $\sqrt{3} \times \sqrt{3}$ lattice constant, the measurements of the electronic structure can be directly compared to calculations using the Anderson model. To keep the model as simple as possible, it is limited to s-waves and effects like spin-orbit interaction are not included. In addition, the Ag atoms were completely ignored in these calculations, as they do not contribute to the disorder and their effect can be directly incorporated into the nearest neighbor interaction energy t_{ij}. This reduces the number of parameters and the size of the Hamilton matrix further, and the $\sqrt{3} \times \sqrt{3}$ lattice can be used as the basis $|\psi\rangle$.

$$\mathcal{H} = \sum_i \epsilon_i |i\rangle\langle i| + t \sum_{i,j} |i\rangle\langle j| \tag{6.2}$$

Assuming a single nearest neighbor interaction parameter t independent of the combination of neighbor atom types, allows to divide Eq. 6.2 by t and makes it effectively an one parameter model, only depending on the the difference of the on-site potentials of the different atom types $\Delta\epsilon$, given in units of t. As basis $|\psi\rangle$ is given by the lattice, an arbitrary alloy structure can be described by a corresponding vector $\vec{a}$, with a_i=1 if the ith lattice point by one atom type (usually Bi) or a_i=0 for the other atom type (Pb or Sb). This allows to directly visualize the spatial distribution of the alloy structure and the resulting eigenvectors $|\psi\rangle$ or probability densities $|\psi|^2$. A positive sign in front of the hopping term leads to a negative effective electron mass and a downwards opened band structure so that the energetically highest state is at the Γ-point. For a negative sign, this is reversed. Periodic boundary conditions are applied to keep the general electronic properties at the border of the lattice the same as in the inner area. The Hamilton matrix and the resulting eigenvalues and eigenvectors are calculated with IGOR Pro and its build-in procedures based on the LAPACK libraries [84] using double precision matrices.

6.3.1 Disorder localization on a local scale

The effect how the introduction of disorder changes the electronic structure in the Anderson model 6.2 is illustrated in Fig. 6.7. The figure shows a comparison of the probability density $|\psi|^2$ of the state at the Γ-point for an ordered and a disordered system with both the same concentration and the parameters for the Anderson model. The concentration of x=0.9375 was chosen to allow a continuous translation invariance in the ordered case across the periodic boundaries of the lattice structure. In the ordered case (Fig. 6.7 b)), one can see how the state is extended uniformly over the whole lattice, only slightly modulated by the presence of the minority atoms. A behavior like this can be seen e.g. in the surface state of the reconstructed Au(111) surface. The herringbone reconstruction [85] forms a periodic structure and local scanning tunneling spectroscopy measurements have shown variations in the intensity at the band edge of the surface state depending on the spatial position, but no energy shift. [86, 87]

In contrast to this, the same state for the disordered structure is strongly localized in an area of a high concentration of impurities (Fig. 6.7 d)). Plotting the radially averaged $|\psi|^2$ as a function of distance from the lattice point $\vec{r}_0$ with the highest probability density $|\psi_0|^2$ illustrates the exponential drop (see Fig. 6.7 e)). The localization length ξ can be obtained by fitting the function

$$|\psi(\vec{r})|^2 = |\psi_0|^2 \mathrm{exp}\left[-\frac{|\vec{r}-\vec{r}_0|}{\xi}\right] \tag{6.3}$$

Variations in the parameter $\Delta\epsilon$ (given in units of t) do not change the general picture. In the ordered alloy, this only changes the strength of the modulation due to the impurities, while in the disordered case there is a variation in exponential decay length as seen in Fig 6.7 e). The evolution of the exponential decay length as function of $\Delta\epsilon$ in the case of positive as well as negative t for disordered alloys is displayed in Fig. 6.7 f). For each parameter set, the first state of 100 random alloy structures with the same concentration was calculated and the resulting localization lengths were averaged. For both positive and negative parameter t, the localization length follows a power law $\xi \propto \Delta\epsilon^{\nu}$, with an additional offset in the case of negative t. In both cases the exponent ν was found to be close to -1 with $\nu = -1.13 \pm 0.01$ for positive t and $\nu = -1.03 \pm 0.01$ for negative t. For this concentration, the offset for the case of negative t was found to be $1.09 \pm 0.04\,\mathrm{nm}$ corresponding approximately to two lattice constants. The dashed lines mark the values for which the localization length becomes larger than half of the system size or smaller

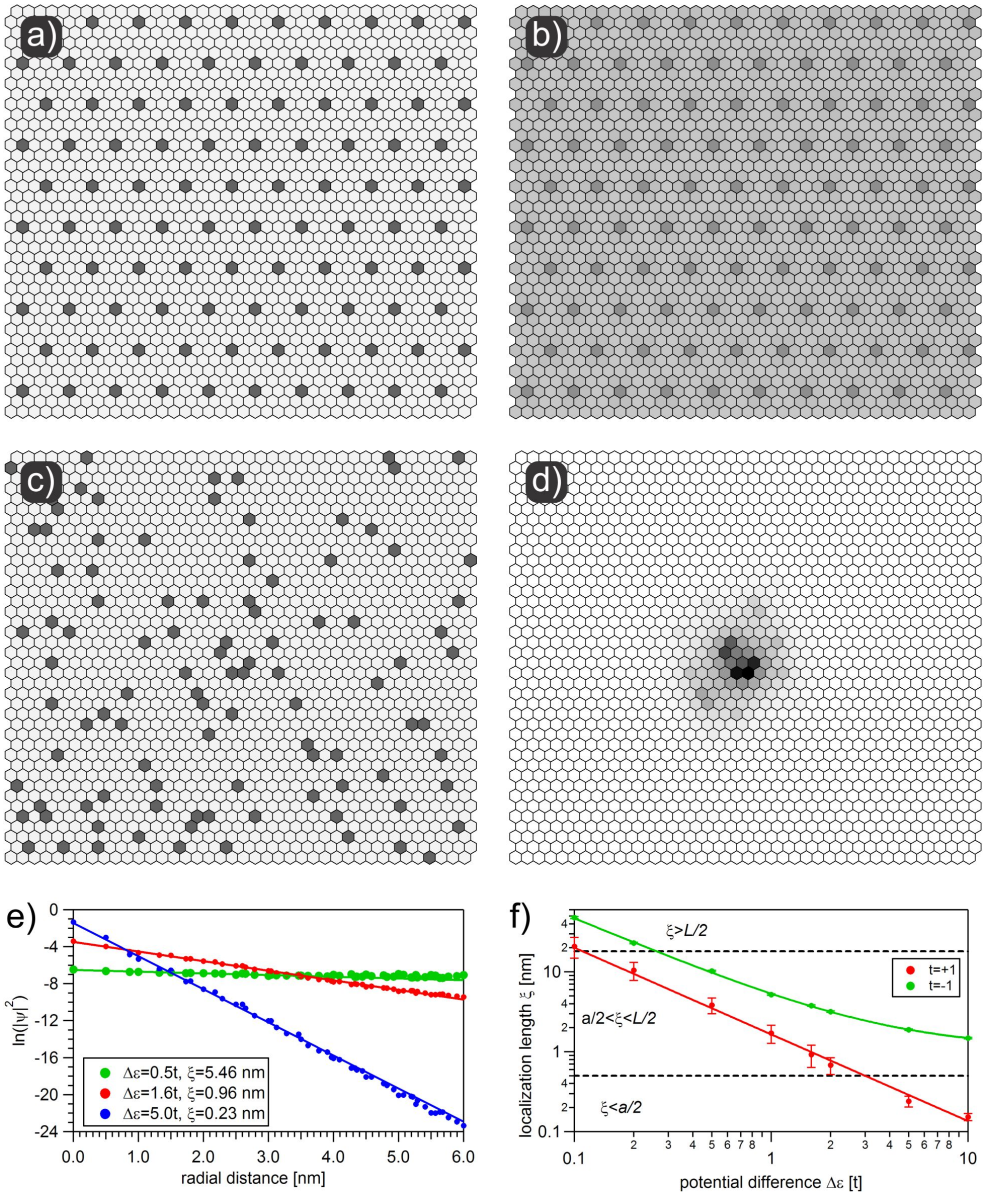

Figure 6.7: a) 40 × 40 atoms structure for an ordered alloy with x=0.9375 corresponding to 100 atoms of the minority element. b) Probability density of the state at the Γ-point (k=0) calculated for the ordered alloy structure in a) for $\Delta\epsilon = 2.0$. c) Alloy structure with the same concentration as a), but with randomly distributed minority atoms. d) Probability density calculated from the disordered alloy structure in c) for the same parameter as b). In the probability density maps, black indicates a high probability. e) Plot of the probability density as a function of the radial distance for different $\Delta\epsilon$ values and positive t. The fit of an exponential decay function is used to determine the localization length ξ. f) Localization length as a function of the tight-binding parameter $\Delta\epsilon$ in the case of positive and negative t for the disordered alloy. For the calculation of the localization length a lattice constant of 0.5 nm is assumed.

then half the lattice constant, respectively. In the former case, the states can be viewed as extended states, while in the latter they can be viewed as impurity localized states.

6.3.2 Comparison to experiment

To see, if the localized states measured in dI/dV-maps as Fig. 6.5 b) can be described by the Anderson tight-binding model, a direct comparison between measurement and calculation is necessary. Due to the limitation of the disordered alloy structure (and consequently the confinement of the electronic structure) to a two dimensional system in the topmost layer, the surface alloys give the unique opportunity to do this using the topographic and electronic data gained simultaneously from the STM measurements. Model alloy structures deduced from STM topographies can be used in the calculations. Provided the measurement resolution is good enough, it is possible with the automated data analysis algorithm to generate the necessary structure data even for large measured alloy structures. Structures up to approximately 7000 atoms, corresponding to a $40 \times 40\,\mathrm{nm}$ STM image were generated this way and used in the calculations. Such alloy structures that include an area larger than the measured dI/dV-maps were used to minimize the effect of the periodic boundary conditions in the area of interest. In addition, the large structure results in a higher density of eigenvalues and so a better representation of the electronic structure.

To simulate the experimental broadening, the resulting probability densities (depending on the corresponding energy eigenvalue) are weighted with a Gauss function (defined by the center energy E_{center} and the FWHM E_{broad}) and then integrated.

$\mathbf{Bi_{0.80}Pb_{0.20}}$/Ag(111)

The on-site potential difference $\Delta\epsilon_i$ of Bi and Pb are given by the band onsets of the pure surface alloys Bi/Ag(111) and Pb/Ag(111) as displayed in Fig. 6.1 and is approximated as $\Delta\epsilon = 0.8$. In principle, the nearest neighbor interaction energy t_{ij} can be estimated from the band width. However, there is no experimental data for the band width of the three upper bands and in the first principle calculations that show the full band width of all bands at least for Bi/Ag(111) [80], the width of the lower band differs greatly from the experimental data for Bi/Ag(111) [88] and Pb/Ag(111) [89] measured with ARPES. Instead, for the comparison of experimental data and the calculations, t_{ij} was adapted to reproduce the measured dI/dV-maps.

Fig. 6.8 displays several dI/dV-maps measured on $Bi_{0.80}Pb_{0.20}$/Ag(111) at different

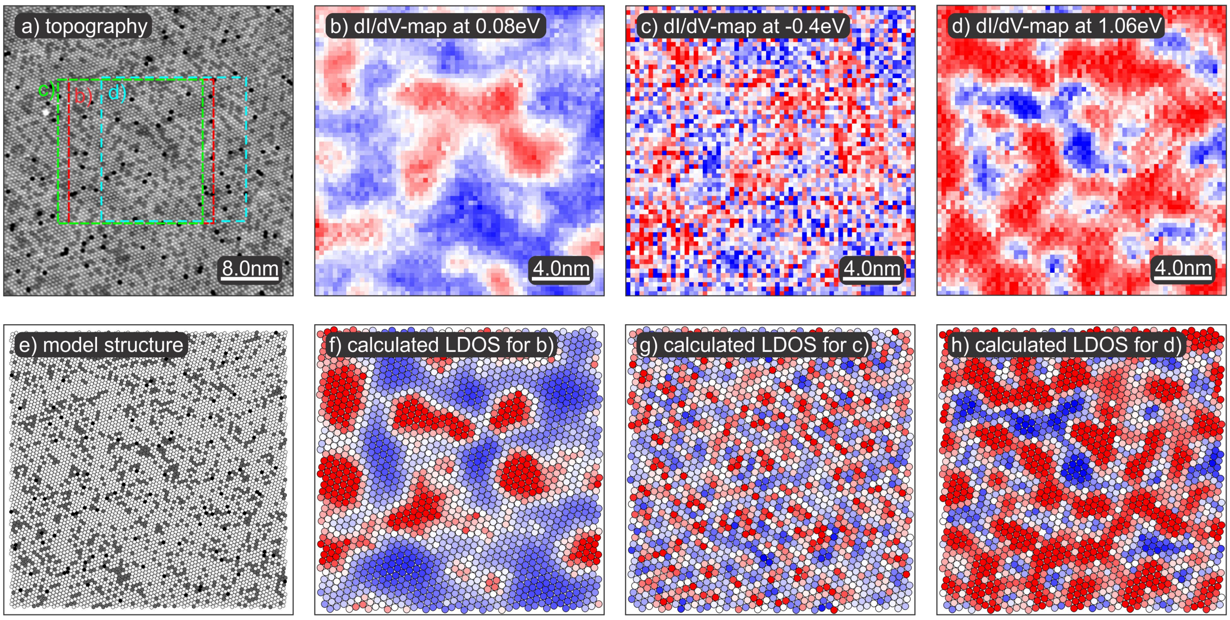

Figure 6.8: a) 40 × 40 nm overview image of $Bi_{0.80}Pb_{0.20}/Ag(111)$ measured at 3 mV, 7.0 nA. The boxes mark the positions of the dI/dV-maps displayed in b)-d). b) dI/dV-map measured at 0.08 eV, 1.0 nA at the onset of the sp_z-band. c) dI/dV-map measured at -0.4 eV, 1.0 nA, deeper inside the sp_z-band. d) dI/dV-map measured at 1.06 eV, 1.0,nA, at the onset of the $m_j = 3/2$-band. e) Model alloy structure deduced from the topographic image a). This structure was used in the tight-binding calculation to simulate the local densities of states f)-h) which reproduce the measured dI/dV-maps. In all measured dI/dV- and simulated local density maps, red indicates a high intensity and blue a low intensity.

dI/dV-map energy	$\Delta\epsilon$	t	E_{center}	E_{broad}
0.08 eV	0.8	1.2	-0.22	0.12
-0.40 eV	0.8	1.2	-1.5	0.12
1.06 eV	0.8	-0.47	-0.18	0.12

Table 6.2: Parameters used in the calculation of the probability density maps in Fig. 6.8 f)-h).

energies corresponding to the band onsets of the sp_z- and $m_j = 3/2$-band as well as states deeper inside the sp_z-band. Due to the thermal drift, it was not possible to measure all dI/dV-maps at the same location. However, the topographic structure measured simultaneously allowed to identify the location of the dI/dV-map in the overview image as marked in Fig. 6.8 a). Both dI/dV-maps near the band onsets, Fig. 6.8 b) and d) show strong variations in the intensity, forming clearly separated areas of high and low intensity. Except for the inverted intensity, they show a similar spatial structure. This structure can be correlated with the distribution of the different substitutional atoms seen in the topography of the surface alloy. In contrast to this, in the dI/dV-map further inside the sp_z-band (Fig. 6.8 c)), this spatial structure is almost completely lost, and no correlation with the alloy structure can be made. The simulated probability density maps near the band onsets in Fig. 6.8 f) and h) can reproduce the general spatial features and for the dI/dV-map at 1.06 eV ($m_j = 3/2$-band) an especially good agreement could be achieved in the simulation. For the simulated probability density map inside the sp_z-band, an E_{center} was set to -1.5 which is approximately the same position in the simulated band as -0.40 eV in the measured band. In table 6.2 the tight-binding parameter $\Delta\epsilon$ and t as well as E_{center} and E_{broad} for the calculation of the local densities of state shown in Fig. 6.8 f)-h) are summarized. To reproduce the electronic structure found in the dI/dV at 1.06 eV, a negative t parameter was used, leading to an upwards opened band with a positive effective mass.

To determine a localization length ξ for this system, the three states nearest to the Γ-point, which are the energetically highest (lowest) states for the sp_z-band ($m_j = 3/2$-band) are studied for each band. The probability density maps for these states are displayed in Fig. 6.9. In addition, for each state the average of the probability density as function of the distance from the lattice point with the highest value is plotted. By fitting an exponential decay function to these plots, the localization length ξ was extracted. The localization length for the sp_z-band is found to be somewhat smaller (localization length of the first state $\xi_{1st} = 1.33 \pm 0.04\,\text{nm}$) than for the $m_j = 3/2$-band ($\xi_{1st} = 1.58 \pm 0.25\,\text{nm}$).

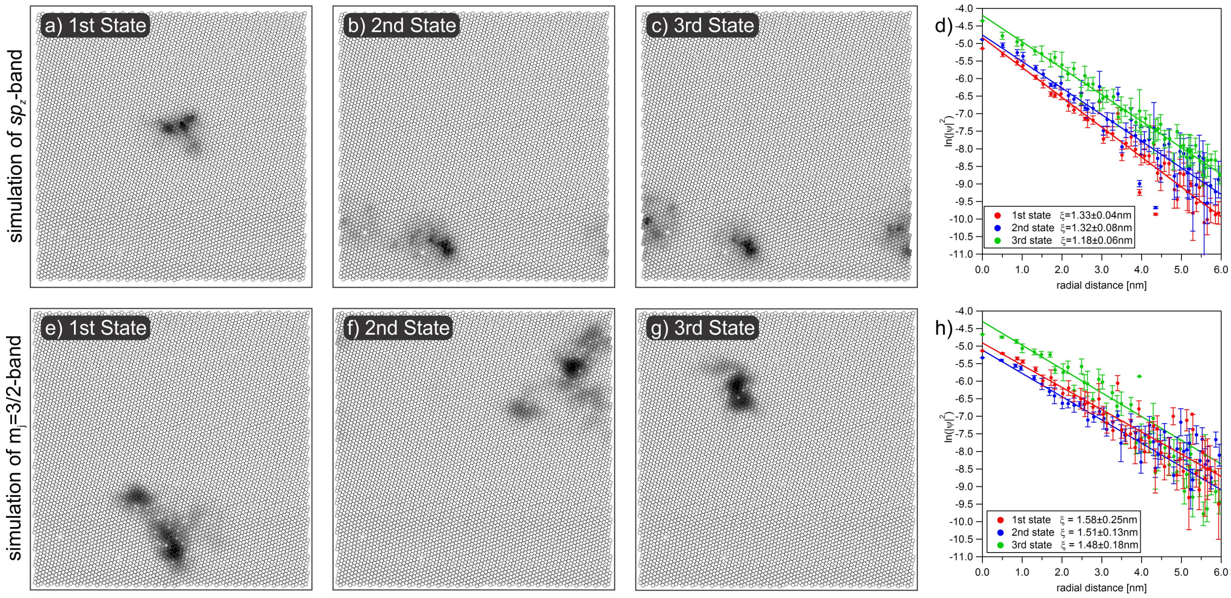

Figure 6.9: a)-c) The energetically highest three states (near the Γ-point) for the calculated sp_z-band of $\mathrm{Bi}_{0.80}\mathrm{Pb}_{0.20}$/Ag(111). Black indicates a high and white a low probability density. d) Probability density plot as function of the radial distance from the point with highest density for the states displayed in a)-c). The energetically lowest three states (near the Γ-point) for the calculated $m_j = 3/2$-band. h) Probability density plot as function of the radial distance from the point with highest density for the states displayed in e)-g).

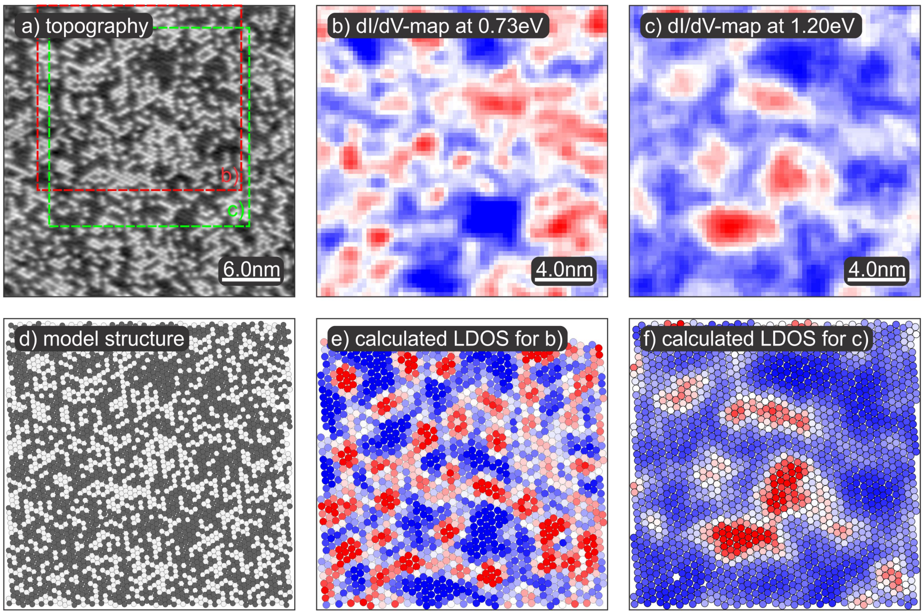

Figure 6.10: a) 30×30 nm overview image of $Bi_{0.39}Sb_{0.61}$/Ag(111) measured at 3 mV, 7.0 nA. The boxes mark the positions of the dI/dV-maps displayed in b) and c). b) dI/dV-map measured at 0.73 eV, 1.0 nA at the onset of the $m_j = 1/2$-band. c) dI/dV-map measured at 1.20 eV, 1.0 nA, at the onset of the $m_j = 3/2$-band. d) Model alloy structure deduced from the topographic image a). This structure was used in the tight-binding calculation to simulate the local densities of states e) and f) which reproduce the measured dI/dV-maps. In all measured dI/dV- and simulated local density maps, red indicates a high intensity and blue a low intensity.

$Bi_{0.39}Sb_{0.61}$/Ag(111)

For Bi_xSb_{1-x}/Ag(111), the determination of the on-site potential difference is not as simple as for Bi_xPb_{1-x}/Ag(111). As Bi and Sb are isoelectric, the potential difference between the respective pure surface alloys is comparatively small and different for each band. However, as there is an energy shift going beyond that potential difference, an effective potential difference is assumed for the tight-binding calculation.

The comparison of the dI/dV-maps of $Bi_{0.39}Sb_{0.61}$/Ag(111) with the simulated probability density maps gives similar results as for $Bi_{0.80}Pb_{0.20}$/Ag(111). As before, the two dI/dV-maps measured at the band onset of the $m_j = 1/2$-band (Fig. 6.10 b)) and the $m_j = 3/2$-band (Fig. 6.10 c)) show clearly separated areas of high and low intensity, which can be correlated with the distribution of the substitutional atoms in the topographic image. Also in this case, there is an intensity inversion between the two dI/dV-maps. It was also possible to reproduce the measured dI/dV-maps with calculated probability density

dI/dV-map energy	$\Delta\epsilon$	t	E_{center}	E_{broad}
0.73 eV	0.6	0.47	-0.05	0.12
1.20 eV	0.4	-0.5	0.05	0.12

Table 6.3: Parameters used in the calculation of the probability density maps in Fig. 6.10 e) and f).

maps (Fig. 6.10 e) and f)). The respective parameters used in the simulation are compiled in table 6.3. As in case of the dI/dV-map at 1.06 eV for $Bi_{0.80}Pb_{0.20}/Ag(111)$, here for the dI/dV-map at 1.2 eV a negative t-parameter was necessary for a correct simulation. Again an especially good agreement between dI/dV-map and simulated probability density map was found for the $m_j = 3/2$-band.

From the respective states at the Γ-point in the simulation (the energetically highest state for the $m_j = 1/2$-band and the lowest state for the $m_j = 3/2$-band), the localization length ξ was determined (see Fig. 6.11). For the $m_j = 1/2$-band a stronger variation in the localization length of the first three states is found, with ξ ranging from 0.76 nm to 1.21 nm. To compensate for this, the first nine states were taken into account. The average localization length was found to be 0.94 nm with a standard deviation of 0.14 nm, somewhat smaller then the localizations length found for the $m_j = 3/2$-band

6.3.3 Histogram analysis

Theoretical considerations show that with the transition from extended states to localized states the distributions of fluctuations of quantities such as the local density of states or the current density change from a gaussian to a log-normal distribution [90, 91]. For the local density of states, this has been supported experimentally for impurity-localized states in $Ga_{1-x}Mn_xAs$ [92]. Fig. 6.12 shows comparison of the histograms of the experimentally measured dI/dV-maps and the simulated probability density maps that were shown in Fig. 6.8 and Fig. 6.10. In general, the simulated histograms show a wider distribution with higher values having a nonzero probability compared to the experimental histograms. The histograms of the simulated probability density maps show all a more or less distinct log-normal-like distribution except for the states inside the band (Fig. 6.12 b)) for which, as expected for extended states, a gauss-like distribution is found. The two histograms of the experimental dI/dV-maps in Fig. 6.12 c) and d) show a deviation from the log-normal distribution and from the corresponding simulated distribution. These distributions show a slightly negative skewness, a behavior that is not covered by the log-normal distribution.

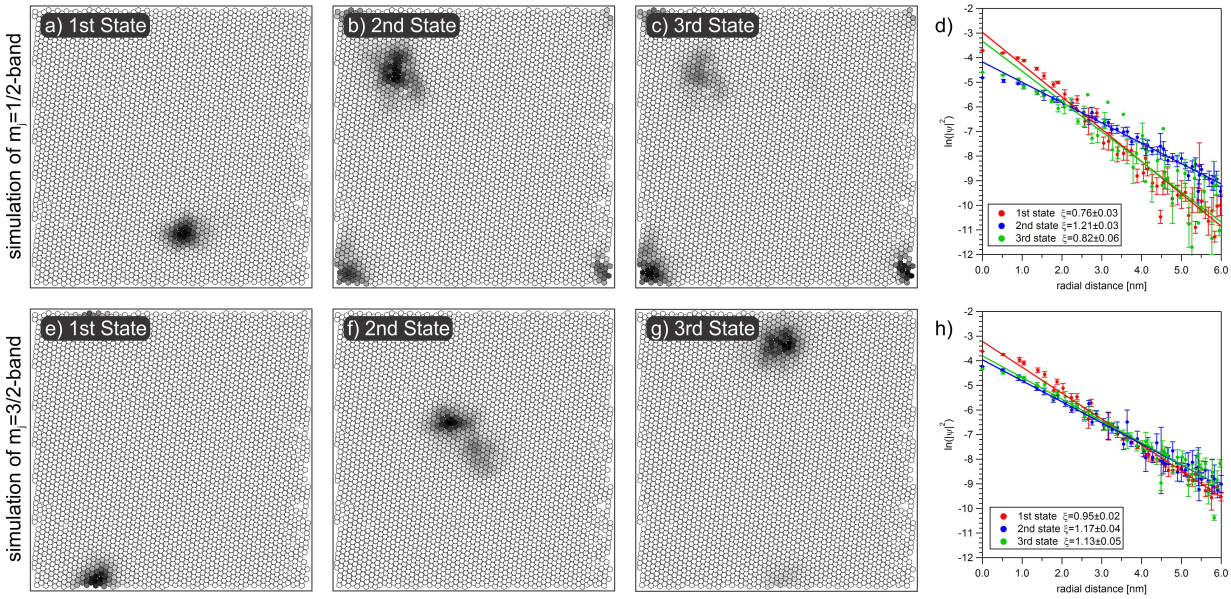

Figure 6.11: a)-c) The energetically highest three states (near the Γ-point) for the calculated $m_j = 1/2$-band of $Bi_{0.39}Sb_{0.61}/Ag(111)$. Black indicates a high and white a low probability density. d) Probability density plot as function of the radial distance from the point with highest density for the states displayed in a)-c). The energetically lowest three states (near the Γ-point) for the calculated $m_j = 3/2$-band. h) Probability density plot as function of the radial distance from the point with highest density for the states displayed in e)-g).

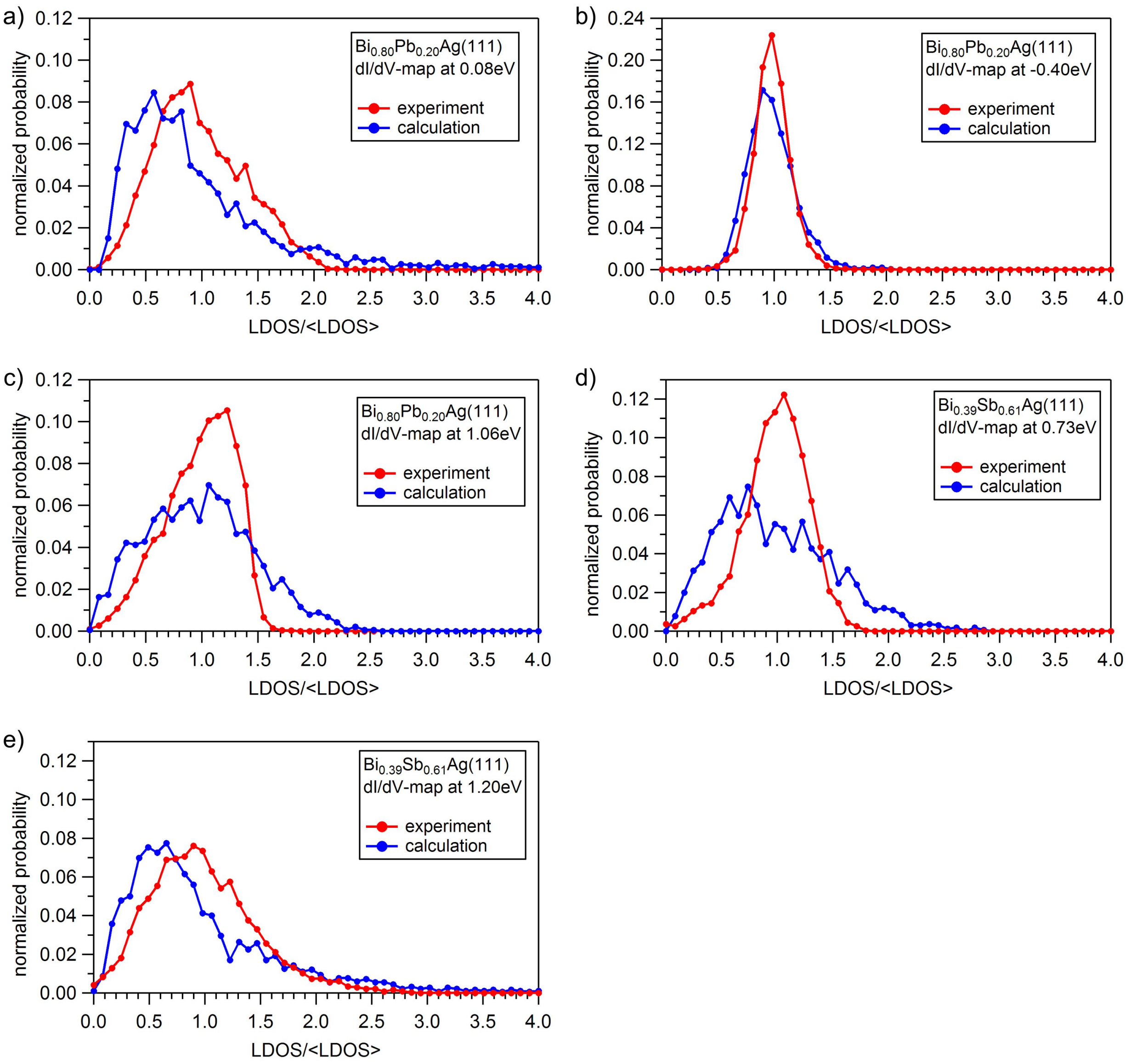

Figure 6.12: Comparison of the normalized histograms of the measured dI/dV-maps and the corresponding calculated probability density maps. Before calculating a histogram, the LDOS was normalized by scaling so that the average $\langle LDOS \rangle$ becomes 1. In addition, the area below the histogram curve has been normalized to 1. a)-c) Histograms for $Bi_{0.80}Pb_{0.20}$/Ag(111) (Fig. 6.8). d)-e) Histograms for $Bi_{0.39}Sb_{0.61}$/Ag(111) (Fig. 6.10).

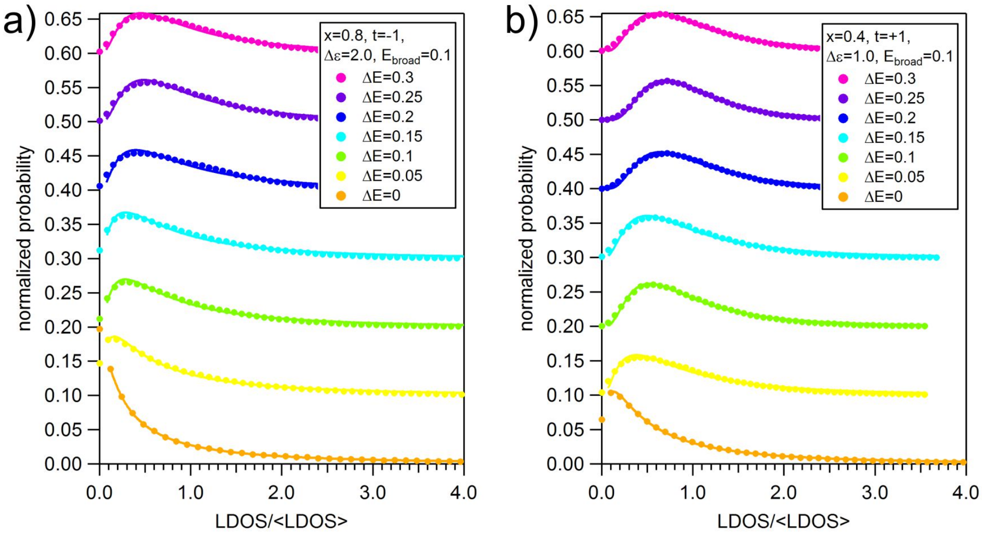

Figure 6.13: Example histograms of simulated probability densities at different energies near the band onset. For the histograms with $\Delta E = 0$, E_{center} is set to the band onset, and the positive ΔE values indicate a relative energy shift away from the band onset to the center of the band.

To see if this is an effect of Anderson localization, a series of histograms with a variety of parameter values were simulated. Each histogram is averaged over the results of random 100 configurations for different alloy concentrations. Tight-binding parameters were varied from $\Delta\epsilon = 0.1$ to $\Delta\epsilon = 5$ for $t = \pm 1$. Histograms were calculated from broadened states with $E_{broad} = 0.1$ for different energies near the band onset with an energy difference ΔE from the 1st state at the Γ-point ranging from 0 to 0.3. Fig. 6.13 shows results for tight binding parameters similar to those used in the simulation of the two dI/dV-maps with negative skewness. However, no set of parameters in this parameter space resulting in a distribution with negative skewness was found.

6.4 Discussion

The effect of the spatial localization of the surface alloy bands can be understood by the fact that the energy difference for environments with locally different chemically structure is too great for the electron wave function to propagate into such different regions [3]. The comparison of spatial electronic structure represented by the dI/dV-map Fig.6.5 b) with the local concentration implies that at every Bi atom a state is exponentially localized. Considering that due to the experimental broadening many states with in a certain energy range but localized at different positions are measured simultaneously, the correlation between state energy and local concentration gives rise to this agreement between the dI/dV-map and the local concentration map. However, if the experimental broadening becomes considerably smaller than the energy shift of the states, this oversimplified picture would not hold anymore. Instead, the more extensive Anderson tight-binding is used.

The statement of the localization in the disordered structures is limited to the examined area. Due to the periodic boundary conditions, a periodic structure is formed on a larger scale similar to the ordered alloy structure in Fig. 6.7 a) leading to an infinite expansion of the state. However limiting the view to the area inside the boundaries, the argument of exponential decay holds and one can speak of localized states. The study of the localization length as function of $\Delta\epsilon$ shows that for the system sizes ($L \approx 20\,\mathrm{nm}$) and the tight-binding parameters used in the simulations, the localization of the states can be viewed as disorder localization. The difference in the localization length as well as the offset for negative t can be attributed to the concentration asymmetry. In this case, the states are localized at the majority atoms for negative t, for which larger areas of uniform concentration without disorder inside exists. So the states can generally extend further and there is a lower length limit for the disorder localization corresponding to the radius of the areas with uniform concentration. For more balanced concentration this effect should become smaller and vanish completely in the case of x=0.5.

Considering that a simplified tight-binding model was used for the calculation neglecting $p-$orbitals and the Rashba splitting, the reproduction of the features seen in the dI/dV-maps is remarkable and demonstrate that these findings are indeed localized states that can be described by the Anderson model. Furthermore the almost complete loss of structural features in the dI/dV-map further inside the band at -0.40 eV demonstrates that also in the case of disorder localization there is a transition from localized states to extended states as predicted by theory [64].

The inversion of the intensity seen in the dI/dV-maps Fig. 6.8 b) and d) at the band onsets imply that in the case of the sp_z-band the states are localized at areas of a high Pb concentration, while for the $m_j = 3/2$-band the states are localized at areas of high Bi concentration. As the potential energy at the Bi atoms is lower than for Pb atoms, a localization of the states at the Γ-point in these areas is only possible, if the $m_j = 3/2$-band has a positive effective electron mass. This is also taken into account in the negative t parameter for this band in the tight binding calculations. This result of an $m_j = 3/2$-band with a positive effective electron mass stands in contrast to the theoretical calculations, which predict a negative effective electron mass for this band [60, 80]. On the other hand, the negative effective mass for the sp_z-band in $\mathrm{Bi}_{0.80}\mathrm{Pb}_{0.20}$/Ag(111) and the $m_j = 1/2$-band in $\mathrm{Bi}_{0.39}\mathrm{Sb}_{0.61}$/Ag(111) agrees with the theoretical calculations and the experimental data available from ARPES measurements [19, 20].

At a first glance, the larger localization length ξ for the $m_j = 3/2$-band in $\mathrm{Bi}_{0.80}\mathrm{Pb}_{0.20}$/Ag(111) compared to the sp_z-band seems to be out of place, as a stronger disorder potential was used in the calculation ($\frac{\Delta\epsilon}{|t|} \approx 1.70$ compared to ≈ 0.67) which should lead to a smaller ξ (compare Fig. 6.7 f)). This can be explained by the asymmetry of the substitutional atom concentrations and the localization inversion between the two bands as shown in Fig 6.7 f). For the $m_j = 3/2$-band the first states are localized in areas with high Bi concentration. As the general Bi concentration is high, these areas tend to be larger, allowing the states to extend further. At the other edge of the band at the $\overline{\mathrm{K}}$-point, the states of the $m_j = 3/2$-band are localized at the smaller areas of high Pb concentration. For this state, the localization length was found in the simulations to be $\xi_{last} = 0.19 \pm 0.02\,\mathrm{nm}$ compared to $\xi_{last} = 1.39 \pm 0.13\,\mathrm{nm}$ for the respective state of the sp_z-band localized in the larger areas of high Bi concentration. Only for a symmetric concentration, as it often assumed in theoretical calculations, this effect does not appear. Due to the broken translation invariance and the therefore missing momentum conservation it was not possible to analyze the dI/dV-maps for standing waves to determine the band structure (without the Rashba-splitting) as it was done for Bi/Ag(111) [59].

There are several possible explanation for the general trend of wider distribution observed for the simulated histograms in Fig. 6.12. One effect is spatial averaging in the experiment due to the limited resolution of the tip. Compared to the atomically resolved topographies measured at a tunneling bias of 3 mV, a loss in spatial resolution is observed at the higher bias voltages (ranging from 80 mV to 1.2 V) used in the measurement of the dI/dV-maps. Due to this effect, extreme intensities are damped to more a average value, resulting in a narrower distribution. In addition, the used tight-binding model in itself might be too simple to catch these finer details. The inclusion of p-orbitals and spin-orbit interaction ([56,93]) would improve the model further. However, the limited computational power available for this work and the large supercells needed for the simulations prevented such extensions of the model. Another step to improve simulations of the dI/dV-maps would be the inclusion of the tip by using the Tersoff-Hamann model (see section 2.2.2) with a d_{z^2} orbital as the tip wave function for the tungsten tip [94].

6.5 Conclusion

In this chapter the electronic structure of the mixed surface alloys $Bi_xPb_{1-x}/Ag(111)$ and $Bi_xSb_{1-x}/Ag(111)$ were presented. Using scanning tunneling spectroscopy, it was demonstrated that these systems show a variation of the electronic structure on a local scale which could not be examined before, as only non-local techniques like ARPES for measurements and the KKR coherent potential approximation for simulations were used. It was shown for $Bi_xPb_{1-x}/Ag(111)$ that the states localized in the disordered surface alloy layer are also localized spatially and that this localization can be correlated with the distribution of the substitutional atoms in the surface alloy layer. Using the Anderson tight-binding model it was possible to simulate the measured spatial distribution of the electronic states by using the corresponding topographic structure as a starting point for a supercell calculation.

This demonstrates the possibility of studying the localization of electronic wave functions on a local scale with the with the ability to directly correlate the distribution of the wave functions with the atomic structure of the disorder. The flexibility of the mixed surface alloys as material system - access to the full concentration range and the possibility to exchange the substitutional material or substrates - allows to study the effect of a variety of parameters such as spin-orbit interaction on Anderson localization.

Chapter 7

Other aspects of surface alloy properties

While the main focus of this work lies on the growth and electronic properties of the mixed surface alloys, some related aspects of the surface alloys were also studied, but to a lesser extent. This covers the growth of the Bi/Ag surface alloy on thin, heteroepitaxial films of Ag on Pt(111), a system for which results of LEED and ARPES measurements have been published recently [95]. The second topic of this chapter covers the dealloying of the mixed surface alloys and the formation of a monolayer phase. Similar to the growth of the surface alloys, this has been studied on a local scale only for the pure surface alloys Bi/Ag(111) [49, 74] and Pb/Ag(111) [50, 96].

7.1 Surface alloys on thin films

It has been shown, that structural parameters have great influence on the Rashba splitting found in the surface alloys [51]. One way to study the influence of these structural parameters is the variation of the substrate lattice constant. This can be most easily done by changing the substrate, for example, by switching the substrate from Ag to Cu [88]. Another way to change the lattice constant is to exploit pseudomorphic growth of thin films on a substrate with slightly different lattice constant. Thin films of Ag are known to grow pseudomorphically on a Pt(111) substrate after annealing [97, 98]. Both Pt and Ag have the same face-centered cubic structure, but Ag has a slightly higher lattice constant (409 pm) than Pt (392 pm). In the case of pseudomorphic growth, the Ag thin film assumes the Pt lattice constant, and the film growths under compressive stress. Recent non-local experiments of Bi/Ag/Pt(111) [95] however did not show signs of the expected surface alloy. Instead the published results indicate that Bi forms a p(2×2) reconstructed

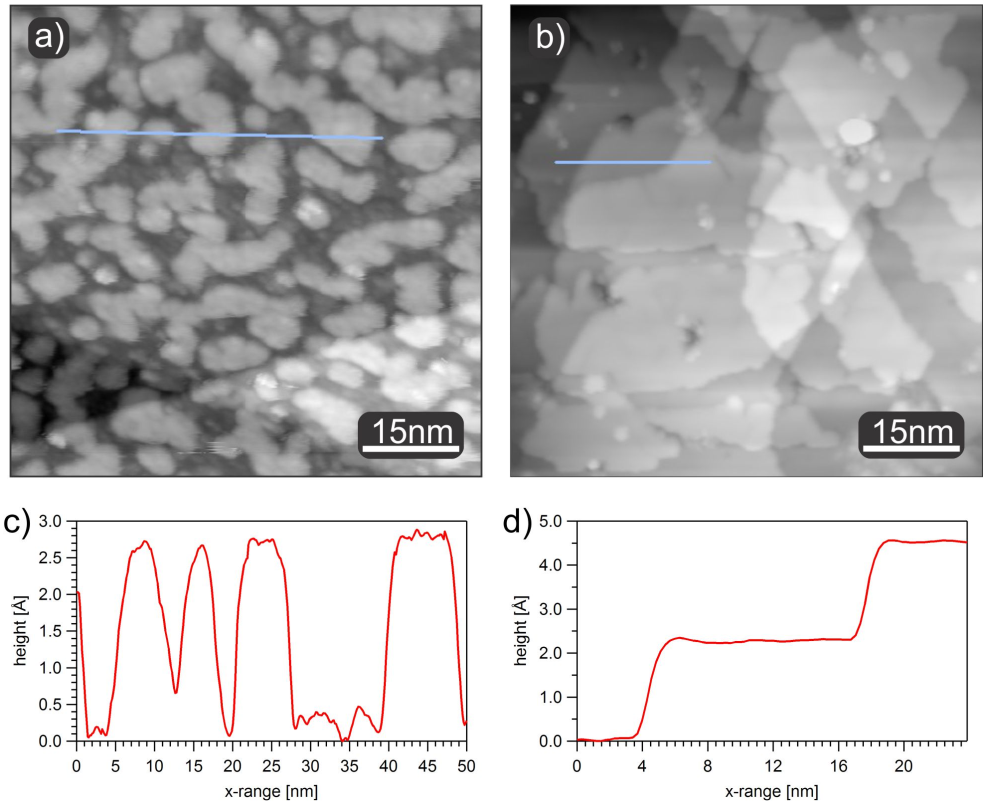

Figure 7.1: a) Topographic image of a submonolayer Ag evaporated on Pt(111) measured at 0.1 V, 0.1 nA. The coverage was estimated to be 0.67 ML. The Ag forms islands of monolayer height. b) Topographic image of the Ag thin film after the evaporation of 3.3 ML on Pt(111), measured at 1.0 V, 0.1 nA. c) Line profile of Ag islands as marked in a). The height of the islands is 2.5 Å. d) Line profile of the Ag terraces as marked in b). The height of the terraces is 2.2 Å.

layer on top of the Ag film. STM measurements might help to clarify the growth of Ag on Pt(111) in the presence of a submonolayer coeverage of Bi.

7.1.1 Growth of Bi/Ag/Pt(111)

Thin Ag films on Pt(111) were prepared as described in section 4.2.1. The topographic image 7.1 a) shows individual Ag islands of monoatomic step height, as can be seen from the corresponding line profile 7.1 c). From the area of the islands compared to the total area, the coverage was estimated to be approximately 0.67 ML and this was used as calibration for the evaporation. Even though the coverage is relatively high, the size of the islands is relatively small and in a range for which pseudomorphic growth was found [98].

For a higher coverage the Ag forms a continuous film with terraces as shown in the

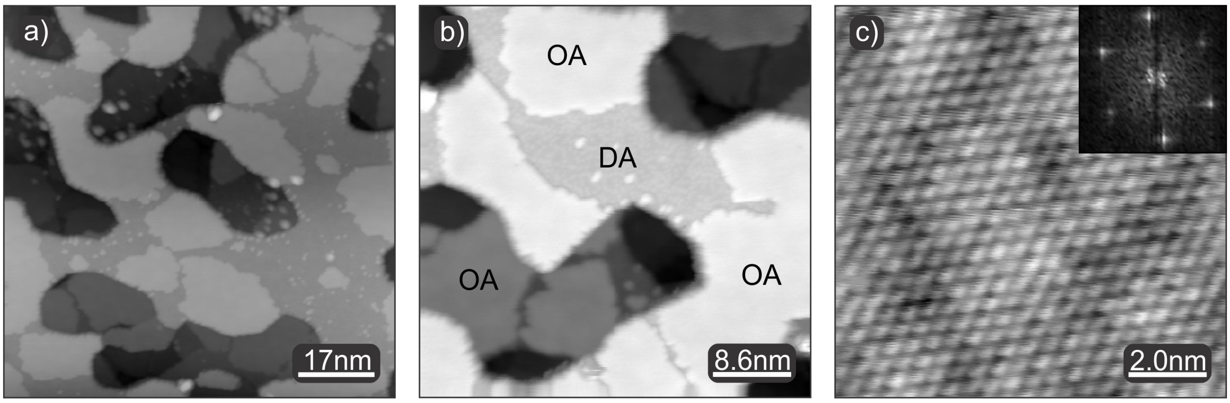

Figure 7.2: a) Topographic overview of Bi/Ag/Pt(111) for 0.16 ML of Bi on a 5 ML thin film of Ag/Pt(111) (measured at 1.0 V, 0.13 nA). Large gaps with a depth of 1 to 3 ML can be seen, while the remaining film is flat except for the apparent height difference of the ordered and disordered surface alloy. h b) Topographic image of the ordered (OA) and disordered Bi/Ag surface alloy (DA) measured at 0.1 V, 0.5 nA. c) Zoom into ordered surface alloy structure, measured at -0.1 V, 0.5 nA. The FFT image in the inset shows the hexagonal structure of the ordered surface alloy.

topographic image Fig. 7.1 b) for a coverage of 3.3 ML. The line profile Fig. 7.1 d) again reveals monoatomic steps but the height of the steps was found to be slightly smaller with 2.2 Å, compared to 2.5 Å in the case of the islands found for submonolayer coverage.

The growth of the film changes drastically if Bi is evaporated additionally. Fig. 7.2 a) shows overview image for a coverage of approximately 0.16 ML of Bi on a 5 ML thin film of Ag/Pt(111). Comparable results were also found for thinner Ag films or other Bi coverages below 1/3 ML. A continuous, flat film with either an ordered or disordered Bi/Ag surface alloy on top has formed (see Fig. 7.2 b)). The disordered surface alloy was found homogeneously distributed on the Ag surface, with the patches of the denser ordered surface alloy increasing with higher Bi coverage. Large holes with a depth of 1 to 3 ML have opened up in the film, and patches of the ordered surface alloy can be seen on the bottom of these holes. Fig. 7.2 c) shows the structure of the ordered surface alloy patches. They show a hexagonal structure with a lattice constant of 5.1 ± 0.2 , indicating the usual $\sqrt{3} \times \sqrt{3}$ reconstruction comparable with the Bi/Ag(111) surface alloy.

7.1.2 Discussion

The difference in the step height for islands in the case of submonolayer Ag coverage and the terraces in the case of higher coverages might be a result of the pseudomorphic growth found for small Ag islands ($\langle$20 nm) [98]. Consequently, for thicker films the structure of the top most layer seems to becomes more Ag-like. The closed film and terraces with monoatomic steps found for higher Ag coverages indicate layer-by-layer growth in agreement with previous results [97, 99].

With submonolayer coverages of Bi present, no sign of the $p(2 \times 2)$ reconstruction that was reported in in [95], was found. In contrast, patches of the ordered and unordered Bi/Ag(111) surface alloy had formed on the Ag film. However, some change in the growth of the Ag film was found when Bi is present, which seems to act as a surfactant similar to Sb. It is known for Sb to change the growth behavior of Ag in homoepitaxy from island to layer-by-layer growth [100, 101]. However the holes in the film (see Fig. 7.2 a) and b)) contradict a purely layer-by-layer growth of the Ag film. Their depths, which is smaller than the film thickness expected from the evaporation parameters indicates instead a growth behavior similar to layer-plus-island growth. While the first few monolayers form a continuous film, the later monolayer do not form islands but a film perforated with large gaps instead. The transition from the continuous to the perforated film might also mark the return from pseudomorphic growth to original Ag lattice structure as indicated by surface alloy on the topmost Ag layer with the $\sqrt{3} \times \sqrt{3}$ reconstruction and a 5 Å lattice constant as found on Bi/Ag(111).

7.2 Dealloying of mixed surface alloys

During the study of the mixed surface alloy, also the monolayer phases were observed. If there is an excess of substitutional atoms, dealloying of the substitutional atoms starts to take place and a monolayer on top of the pure Ag(111) substrate is formed.

For a coverage larger than 1/3 ML of Bi or Pb on Ag(111) this leads to the formation of different reconstructions. For Bi/Ag(111) a reconstruction in the form of stripes running along the Ag$[11\bar{2}]$ direction is found [49, 74]. Different models have been proposed for this structure with a $\sqrt{3}$ periodicity in the $[11\bar{2}]$ direction but either commensurate in the in the $[1\bar{1}0]$ direction with a $\left(\begin{smallmatrix} 3 & 0 \\ 1 & 2 \end{smallmatrix}\right)$ reconstruction [49] or incommensurate in that direction [74]. For Pb/Ag(111), a $(\sqrt{28} \times \sqrt{28})\mathrm{R}19.1^\circ$ reconstruction with respect to the Ag(111) substrate has been found [96]. Due to the development of these two completely different structures, the question arises, what in the presence of multiple substituents happens as dealloying takes place?

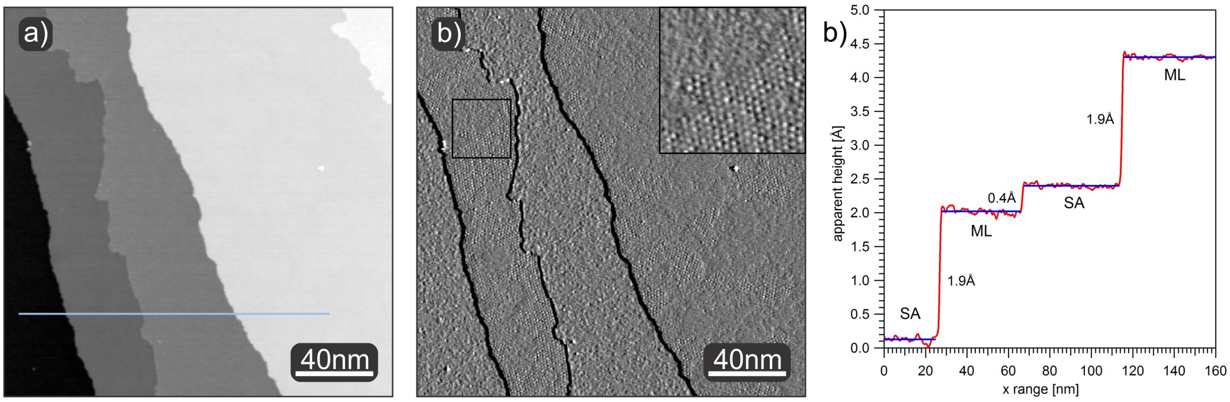

Figure 7.3: a) Overview image with terraces of the $Bi_{0.5}Pb_{0.5}$/Ag(111) surface alloy and of the monolayer phase measured at 1.0 V, 1.0 nA. b) Current image for a) which allows to identify the terraces with the surface alloy phase (1st and 3rd from left to right) and those with the monolayer phase (2nd and 4th). The inset shows an enhancement of the marked area, showing the presence of an ordered and an unordered phase in the monolayer. c) Lines profile of the marked line in a), displaying the different step heights for surface alloy (SA) and monolayer (ML) terraces.

7.2.1 The Monolayer phase for balanced Bi-Pb concentrations

Fig. 7.3 a) displays a overview image with several terraces for a sample with balanced Bi and Pb concentration. In the current image (Fig. 7.3 b)), which corresponds to the first derivative of the topography, the different, alternating surface structures of the terraces are visible. The terraces with the surface alloy can be identified by their rougher structure seen in the current image (first and third terrace from left to right), which arises from the inhomogeneous structure of the surface alloy and cannot be resolved atomically at these scales and tunneling parameters. The other terraces are formed by the monolayer phase which appears smoother. The inset shows that the monolayer itself contains two different phases, with one consisting of an ordered structure. The line profile in Fig. 7.3 c), shows terraces with two different apparent heights, 1.9 Å for the monolayer terraces and 0.4 Å for the surface alloy terraces.

Finer details of the monolayer phase are displayed in Fig. 7.4. On the left side, the surface alloy phase can be seen as a measure of the resolution of the tip. On the right side, the monolayer can be seen with patches of the ordered phase. The ordered phase consists of a hexagonal structure with an periodicity of 16.8 ± 0.4 Å, in good agreement with the pure Pb monolayer phase. The rest of the monolayer phase appears as a randomly distributed and inhomogeneous phase with areas of two different apparent heights. No

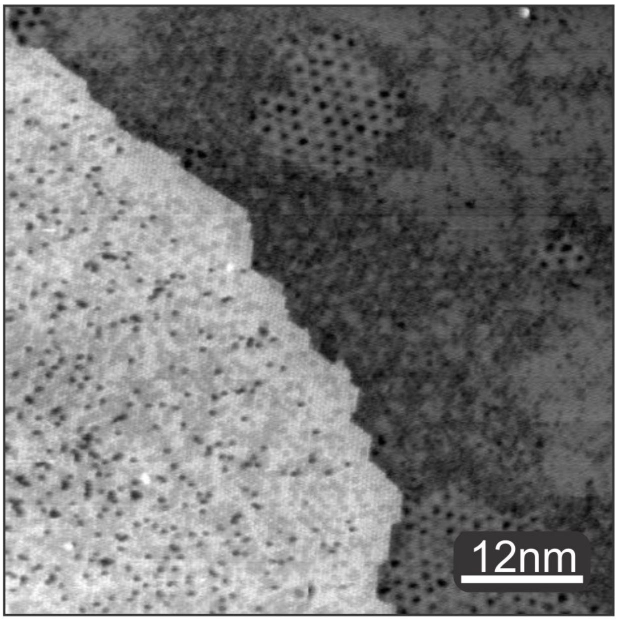

Figure 7.4: 60 × 60 nm topography measured at 5 mV, 9.0 nA, showing finer details of the monolayer structure. On the left terrace, the atomically and chemically resolved surface alloy can be seen. On the right terrace, different phases of the monolayer can be seen

atomic resolution was achieved on this part of the monolayer, and no sign of a striped structure, that would indicate a pure Bi monolayer, was found.

7.2.2 Monolayer phase for diluted Bi-Pb concentrations

For dilute alloy concentrations, the monolayer phase shows a different behavior. Fig. 7.5 shows topographies of the monolayer phase for dilute concentrations of $x \approx 0.9$ in Fig. 7.5 a) and b) and for $x \approx 0.1$ in Fig. 7.5 c) and d). In these cases only periodic structures corresponding to pure monolayer phases of the respective majority element of the substituents can be found. In the case of a high Bi concentration, a reconstruction of the surface forming long stripes can be seen, comparable to the reconstruction of the monolayer phase found after the evaporation of more then 1/3 ML of Bi onto Ag(111) [49,74] . It can be seen in Fig. 7.5 a) that the stripes of the reconstruction run parallel to the substitutional lattice of the surface alloy, which indeed corresponds to the $[11\bar{2}]$ direction.

The topography Fig. 7.5 d) shows atomically resolved monolayer for a high Pb concentration. It shows a superimposed modulation with a hexagonal moiré structure with the same periodicity as the ordered patches found in the monolayer phase for a balanced concentration (Fig. 7.4). The lattice constant for Pb atoms is $3.38 \pm 0.04\,\text{Å}$, the angle be-

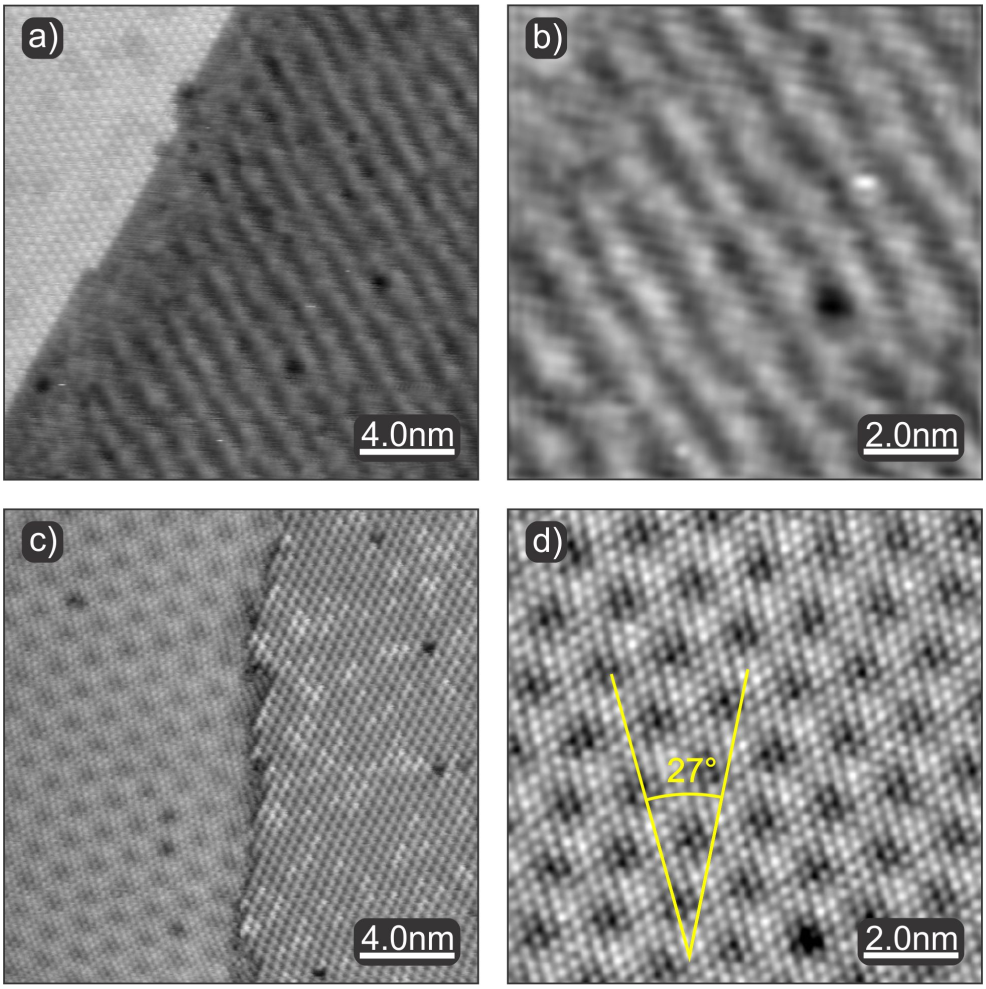

Figure 7.5: a) Topography of the mixed surface alloy $Bi_{0.92}Pb_{0.08}$/Ag(111) (left terrace) and Bi/Ag(111) monolayer phase (right terrace), measured at 5 mV, 5.0nA. b) Zoom into the Bi monolayer phase. c) Pb/Ag(111) monolayer phase (left terrave) and mixed surface alloy $Bi_{0.11}Pb_{0.89}$/Ag(111) (right terrace) measured at 5 mV, 1.0nA. d) Zoom into the Pb monolayer phase.

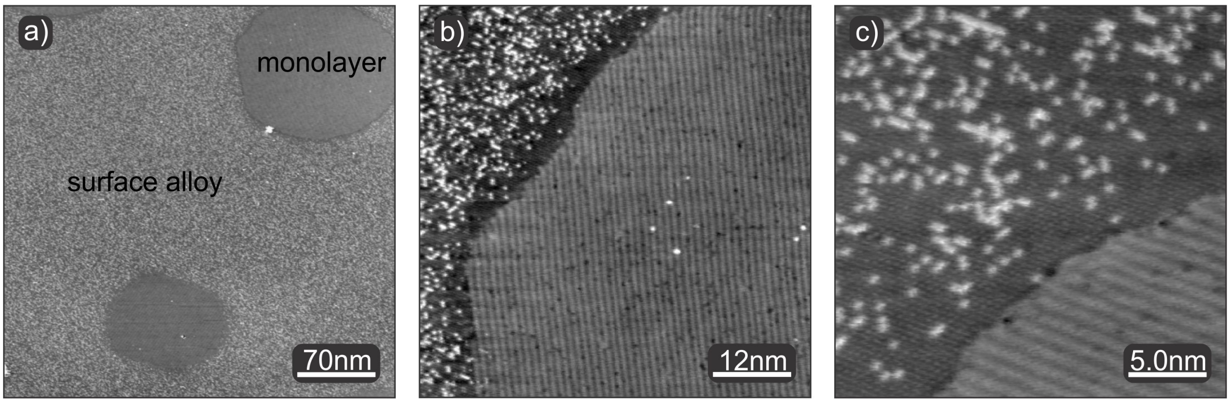

Figure 7.6: a) Overview image of the $Bi_{0.18}Sb_{0.82}$/Ag(111) and the corresponding monolayer phase, measured at 1.0 V, 1.0 nA. b)–c) Detailed images of the surface alloy and the monolayer measured at 3 mV, 7.0 nA.

tween the atomic lattice and the moiré structure is 27°. From the topography in Fig. 7.5 c), showing both the monolayer phase and the surface alloy, the angle between the atomic lattice of the monolayer and the Ag$[11\overline{2}]$ direction given by the surface alloy can be determined. This angle was also found to be 27°, indicating an angle of 3° between the atomic lattices of the monolayer and the Ag(111) crystal. These values are in good agreement to the structure found after evaporating more than 1/3 ML of Pb onto Ag(111) [50, 96].

7.2.3 The Monolayer phase for Bi-Sb

In contrast to the monolayer phase for Bi_xPb_{1-x}/Ag(111) which does form alternating terraces with the surface alloy, the monolayer phase in the case of Bi_xSb_{1-x}/Ag(111) is found to behave quite differently. Fig. 7.6 shows topographies of $Bi_{0.18}Sb_{0.82}$/Ag(111), prepared by evaporation of a 1/3 ML of Bi to form a pure Bi/Ag(111) surface alloy and successive subsequent evaporation of 0.4 ML of Sb. Here, the monolayer forms nearly circular islands in the surface alloy area, as can be seen in the overview image of Fig. 7.6 a). Fig. 7.6 shows that the monolayer phase here has again a striped structure, similar to the case of a high Bi concentration (compare with Fig. 7.5 a)). It can be also seen in Fig. 7.6 c), that the stripes are again parallel to the Ag$[11\overline{2}]$ direction given by the substitutional lattice of the $Bi_{0.18}Sb_{0.82}$/Ag(111) surface alloy

7.2.4 Discussion

From the fact, that only the combined height of a surface alloy and an monolayer terrace for $\mathrm{Bi}_x\mathrm{Pb}_{1-x}$/Ag(111) result in the Ag(111) step height of approximately 2.3 Å, it follows that both phases share the same terrace. The surface alloy phase starts at the lower edge of the next higher Ag(111) terrace (there covered with the monolayer phase) and the monolayer phase ends at edge to the next lower Ag(111) terrace. The monolayer fraction of a surface was found to vary from preparation to preparation in a range from over one half of the terraces to sporadic patches of about 20 nm in size at the terrace edge. It appears that during the sample preparation at 570 K surplus atoms can move freely around and accumulate at step edges where they start to form the monolayer. This fits to the growth process of the pure Pb monolayer on Ag(111) as described in [50]. It can be assumed, that the inhomogeneous structure of the monolayer for balanced concentrations is a result of the mixing of both Bi and Pb in the monolayer phase. The two different apparent heights that can be found in this mixed monolayer might be the result of different configurations for different local mixing ratios.

The agreement of the geometrical details of the monolayer phases found in the case of high concentration of one substituent, indicate that these are indeed pure monolayer phases consisting only of the majority substituent. However, it cannot be excluded, that there is a small amount of impurities from the other elements in the the pure monolayer phases, adapting to the prevailing reconstruction or leading to distortions too small to be recognized.

In the case of $\mathrm{Bi}_x\mathrm{Sb}_{1-x}$/Ag(111), which was prepared by additional evaporation of Sb atoms on a Bi/Ag(111) surface alloy, the formation of the monolayer phase is not determined by the mixing ratio of the substituents. Instead, for a balanced mixing ratio, a pure Bi monolayer phase is formed, while the surface alloy contains a high concentration Sb atoms. In this case, the monolayer phase is formed from Bi atoms that were displaced out of the surface alloy by the Sb atoms. This further supports the hypothesis that Sb is preferred as substituent in Ag(111) and can displace Bi out of the surface alloy instead of just filling vacancies that might be generated by desorbed Bi atoms (see section 5.2.2). If the rate of replacement for both substitutional atoms would be similar (meaning that it there is the same probability for exchanging a Bi atom of the surface alloy with a free Sb atom and the reversed case), such high Sb concentrations larger then 0.5 should not be possible with this preparation method. The finding of Sb as preferred substitutional atom, is in contrast to case of $\mathrm{Bi}_x\mathrm{Pb}_{1-x}$/Ag(111), for which no significant preference for one substituent was found.

7.3 Conclusion

For the trilayer system Bi/Ag/Pt(111), the formation of the ordered and unordered Bi/Ag surface alloy was found on top of the Ag/Pt(111) thin film. The STM measurements indicate that the additional presence of Bi changes the growth behavior of Ag on Pt(111) from a layer-by-layer growth to a growth similar to layer-plus-island growth, leading to a flat, continuous film with large gaps except for the first few monolayers. Comparative studies of this growth between the here shown heteroepitaxial growth of Ag/Pt(111) and homoepitaxial growth of Ag/Ag(111) in the presence of Bi might give further insight into what influence the the Ag-Pt interface and the resulting pseudomorphic growth have on the resulting Ag film.

For the process of dealloying of the mixed surface alloy $\mathrm{Bi}_x\mathrm{Pb}_{1-x}$/Ag(111), it was found that the presence of the two different substituents in the alloy gives rise to a inhomogeneously mixed monolayer phase, which was not observed so far. For higher concentration of one substituent, the formation of the respective pure monolayer phase was restored. The occurrence of a pure Bi monolayer phase for $\mathrm{Bi}_x\mathrm{Sb}_{1-x}$/Ag(111)with a high Sb concentration is a further proof of the preference of Sb as substitutent compared to Bi.

Chapter 8

Summary and outlook

For this thesis, a new UHV system for a variable temperature scanning tunneling microscopy was build. While it is now used mostly for scientific research, it has been (and still can be) used for testing different components for a related UHV compatible mK-STM system. Even though the VT-STM has proven its capability to study topographic and electronic structures on a local scale with high resolution, there is still room for improvement. The new flow cryostat is under construction, and first tests indicate that temperatures down to 4.2 K are possible. This will minimize the drift due to temperature variations and increase the energy resolution in spectroscopic measurements. Further improvements include an extension of the coarse motor for movement in at least one horizontal direction, giving access to a larger sample area.

In this thesis, localization of electronic states due to atomic disorder (Anderson localization) in the mixed surface alloys $\mathrm{Bi}_x\mathrm{Pb}_{1-x}$/Ag(111) and $\mathrm{Bi}_x\mathrm{Sb}_{1-x}$/Ag(111) has been demonstrated on a local scale. This has been achieved by a direct comparison of the local topographic and electronic structure of the surface alloys obtained from STM and STS measurements. The analysis of the topographic structure demonstrated, that in the mixed surface alloys the different substituents retain their individual relaxation, making STM measurements with chemical resolution and the extraction of the local disorder structure possible. Statistical analysis of the disordered structure and comparison with Monte-Carlo simulations revealed a small, attractive effective pair interaction between substitutional atoms of the same kind in both mixed surface alloys.

Measurements of the electronic structure of the two surface alloys revealed exponentially localized states, correlated with the local alloy concentration. Using a tight-binding model with the disordered structure obtained from the topographic measurements, the corresponding electronic structures have been directly reproduced. For different states, an inversion of the localization was found, which was attributed to different signs of the effective electron mass.

The growth of $\mathrm{Bi}_x\mathrm{Sb}_{1-x}$/Ag(111) by evaporating Sb on a Bi/Ag(111) surface alloy and the emergence of a Bi monolayer phase at high Sb concentrations demonstrated that Sb is preferred as substitutional element compared to Bi, while no such preference was found for Bi and Pb. For the growth of surface alloys on thin heteroepitaxial films, it has been demonstrated how the presence of the Bi change the growth of the film by acting as a surfactant.

The mixed surface alloys have opened up a unique opportunity to study Anderson localization of electronic waves on a local scale. With this system, it is now possible to study Anderson localization of electronic states on a local scale for a large variety of parameters, such as disorder potential strength, alloy concentration or Rashba energy. This could be even extended further, as there are other possible substituents such as Tl which is also known to form $\sqrt{3} \times \sqrt{3}\,\mathrm{R}30^\circ$ reconstructed surface alloy on Ag(111) [102]. Tl has two valence electrons less then Bi, leading to an even higher potential difference and a shorter localization length in the $\mathrm{Bi}_x\mathrm{Tl}_{1-x}\mathrm{Ag}(111)$ surface alloy. With this it might be possible to study the transition from disorder localization to impurity localization ($\xi < a/2$). Systematic theoretical studies of Anderson localization considering different concentrations and the structural influence of an effective pair interaction might give further insight into the electronic structure of real, disordered solids, that can be tested with the mixed surface alloys.

With the mixed surface alloy $\mathrm{Bi}_{0.80}\mathrm{Pb}_{0.20}$/Ag(111), as system has been found for which the difference between Fermi energy E_F and band onset E_0 is comparable to or smaller than the Rashba energy E_R. For such a system enhanced electron-phonon coupling [58] and increased superconducting critical temperature are predicted [103]. Measurements of this system at very low temperatures would be a test of these predictions. Furthermore, the local variations in the electronic structure due to the disorder allows to directly study the varying influence of the difference $E_0 - E_F$.

Appendix A

Automated Data Analysis for Surface Alloys

The knowledge of the exact distribution of all the substitutional atoms in an area of the mixed surface alloys allows a more extensive, quantitative analysis of the structure. Furthermore, measurements of the electronic structure can be compared directly with model calculations based on the same topographic structure. An analysis of the atomically and chemically resolved topography of the mixed surface alloys by hand (this means the manual determination of the position and type of each substitutional atom) is not practicable as there are approximately 1600 atoms in a 20 nm×20 nm area. However, an automatization of this analysis can be achieved with a simple algorithm. For the implementation *Igor Pro* is used, a program for data analysis and illustration, which includes its own programming language.

Position of the alloy atoms

For the automated data analysis, atoms are recognized as local two dimensional height maxima. To achieve best results for the atom recognition, all information in the image except for the lattice structure has to be filtered out as the height variations due to the chemical contrast can smear out the height maxima indicating an individual atom. Additionally, noise at higher frequencies can introduce false height maxima leading to a wrong identification of additional atoms. Such a filtering can be achieved using FFT filtering. For this, the Fourier transformed of the STM image is calculated, and only certain parts of it are used for an inverse Fourier transformation to create the new image. The effect for different filters is illustrated in Fig. A.1. To extract the lattice structure a band pass

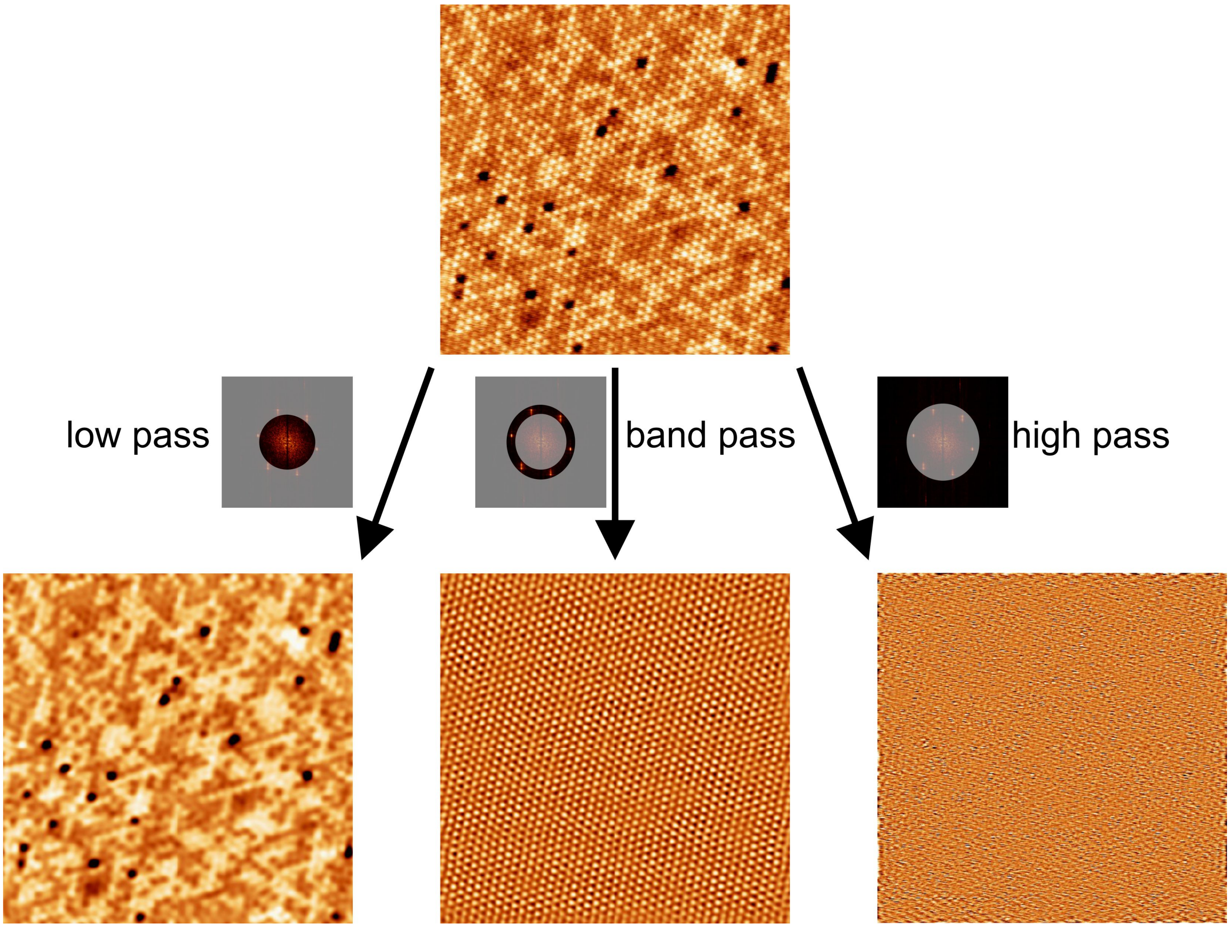

Figure A.1: FFT filtering for mixed surface alloys. The pure lattice structure of the substitutional atoms can be isolated using a band pass filter. Applying a low pass filter gives the height distribution of the substitutional atoms, while the high pass filter reveals the high frequency noise. An appropriate low pass filter can be used to remove this noise from STM images.

filter around a wavenumber equal to the inverse lattice constant is used. So far, this step is done manually but, in principle, can also be automated.

To identify the position of each individual atom, the lattice image gained from the FFT filtering is analyzed row by row, using first and second derivatives of these rows to find local maxima. At each maximum of the row, the corresponding column is analyzed the same way, and if there is a maximum in both directions, the position of an atom has been identified. The height of the atom is then extracted from the data point at the same position in the original image.

As each atom is identified individually, this algorithm can be used directly for any lattice structure, and it also works with lattices that are irregularly distorted (e.g. due to thermal drift). The algorithm does not work if the resolution is not good enough to resolve the atoms as clear maxima in the lattice image.

Atom type assignment

For surfaces with discrete height differences for different atoms in the surface layer, distinct peaks are expected in a histogram of the atom height. Usually, the peaks are smeared out, and might overlap if the height difference is small. So for a clear classification of the atoms by their height, the peaks are fitted with gauss functions and a boundary height z_b in between them is defined. To ensure universality of the algorithm for cases of either overlapping or not overlapping peaks, the boundary value is defined as follows:

$$z_b = \frac{1}{2}\left((z_{\text{low}} + \sigma_{\text{low}}) + (z_{\text{high}} - \sigma_{\text{high}})\right) \tag{A.1}$$

Here z_{low} (z_{high}) is position of the gauss peak for the low (high) atoms and σ_{low} (σ_{high}) is the respective standard deviation. So the boundary height is in the middle between the peak edges, with the edges defined by their standard deviation. Atoms with height $z > z_b$ are assigned as high atoms, and those with $z < z_b$ are assigned as low atoms. The alloy ratio is then simply given by $x = \frac{N_{high}}{N}$, with N_{high} as the number of high atoms and N as the total number of atoms.

There are $\sqrt{3} \times \sqrt{3}$ lattice sites that have a height far outside the lower side of the gauss distribution of the low atoms, so they can be identified easily and either be marked as vacancies or be dropped from the list of substitutional atoms.

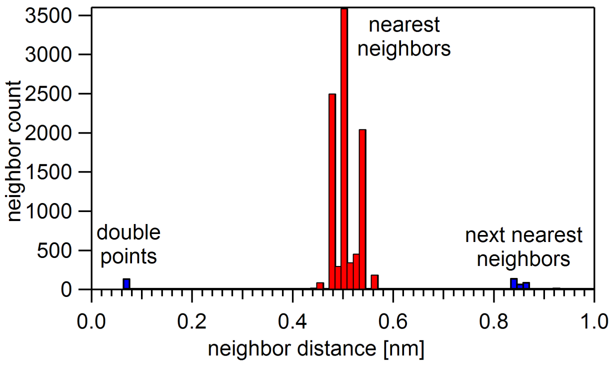

Figure A.2: Typical nearest neighbor distance histogram for a mixed surface alloy with lattice constant a=0.5 nm. The blue bars on the right side of the nearest neighbor distance distribution (red bars) indicate next nearest neighbors, which are removed from the list of nearest neighbors. The blue bars on the left side indicate that some atoms have been incorrectly identified as two atoms.

Nearest neighbor identification

For statistical analysis of the substitutional atom distribution as well as the tight-binding model calculation, the nearest neighbors for each atom have to be identified. This is done by measuring the distance of other substitutional atoms to the atom of interest. In a first run the six nearest atoms (for a hexagonal lattice) are chosen as nearest neighbors for each atom, but this list contains also next nearest neighbors when vacancies are present. In general (mostly due to thermal drift) the nearest neighbor distances are distributed around the lattice constant, and neighbors that are well outside this distribution (this means next nearest neighbors) are dropped from the list of nearest neighbors. Atoms that have been incorrectly identified as two atoms can also be identified and corrected in this step. Fig. A.2 shows a atom height histogram for an surface alloy with an hexagonal lattice and a lattice constant of 0.5 nm after such a first run. After this, a second run gives the correct list of nearest neighbors.

Bibliography

[1] Nørdheim, L. *Ann. Phys. Leipzig* **9**, 607 (1931).

[2] Soven, P. *Phys. Rev.* **156**, 809–813 Apr (1967).

[3] Anderson, P. W. *Phys. Rev.* **109**, 1492–1505 (1958).

[4] Weaver, R. L. *Wave Motion* **12**, 129 (1990).

[5] Hu, H., Strybulevych, A., Page, J. H., Skipetrov, S. E., and van Tiggelen, B. A. *Nature Phys.* **4**, 945 (2008).

[6] Dalichaouch, R., Armstrong, J. P., Schultz, S., Platzman, P. M., and McCall, S. L. *Nature* **354**, 53 (1991).

[7] Wiersma, D. S., Bartolini, P., Lagendijk, A., and Righini, R. *Nature* **390**, 671 (1997).

[8] Schwartz, T., Bartal, G., Fishman, S., and Segev, M. *Nature* **446**, 52 (2007).

[9] Billy, J., Josse, V., Zuo, Z., Bernard, A., Hambrecht, B., Lugan, P., Clément, D., Sanchez-Palencia, L., Bouyer, P., and Aspect, A. *Nature* **453**, 891 (2008).

[10] Roati, G., D'Errico, C., Fallani, L., Fattori, M., Fort, C., Zaccanti, M., Modugno, G., Modugno, M., and Inguscio, M. *Nature* **453**, 895 (2008).

[11] Kondow, S. S., McGehee, W. R., Zirbel, J. J., and DeMarco, B. *Science* **334**, 66 (2011).

[12] Kravchenko, S. V., Kravchenko, G. V., Furneaux, J. E., Pudalov, V. M., and D'Iorio, M. *Phys. Rev. B* **50**, 8039 (1994).

[13] Siegrist, T., Jost, P., Volker, H., Woda, M., Merkelbach, P., Schlockermann, C., and Wuttig, M. *Nature Mat.* **10**, 202 (2011).

[14] Binnig, G., Rohrer, H., Gerber, C., and Weibel, E. *Phys. Rev. Lett.* **50**, 120–123 Jan (1983).

[15] Nagl, C., Haller, O., Platzgummer, E., Schmid, M., and Varga, P. *Surface Science* **321**(3), 237 – 248 (1994).

[16] Sprunger, P. T., Lægsgaard, E., and Besenbacher, F. *Phys. Rev. B* **54**(11), 8163–8171 Sep (1996).

[17] Varga, P. and Schmid, M. *Appl. Surf. Sci* **141**, 287–293 (1999).

[18] Baratoff, A., Binnig, G., Fuchs, H., Salvan, F., and Stoll, E. *Surface Science* **168**, 734 – 743 (1986).

[19] Ast, C. R., Pacilé, D., Moreschini, L., Falub, M. C., Papagno, M., Kern, K., Grioni, M., Henk, J., Ernst, A., Ostanin, S., and Bruno, P. *Phys. Rev. B* **77**(8), 081407 Feb (2008).

[20] Gierz, I., Meier, F., Dil, J. H., Kern, K., and Ast, C. R. *Phys. Rev. B* **83**, 195122 May (2011).

[21] Ast, C. R., Henk, J., Ernst, A., Moreschini, L., Falub, M. C., Pacilé, D., Bruno, P., Kern, K., and Grioni, M. *Phys. Rev. Lett.* **98**, 186807 May (2007).

[22] Bychkov, Y. A. and Rashba, E. I. *JETP Lett.* **39**, 78 (1984).

[23] Bardeen, J. *Phys. Rev. Lett.* **6**, 57–59 Jan (1961).

[24] Giaever, I. *Phys. Rev. Lett.* **5**, 464–466 Nov (1960).

[25] Nicol, J., Shapiro, S., and Smith, P. H. *Phys. Rev. Lett.* **5**, 461–464 Nov (1960).

[26] Tersoff, J. and Hamann, D. R. *Phys. Rev. B* **31**, 805–813 (1985).

[27] Ast, C. R., Wittich, G., Wahl, P., Vogelgesang, R., Pacilé, D., Falub, M. C., Moreschini, L., Papagno, M., Grioni, M., and Kern, K. *Phys. Rev. B* **75**(20), 201401 May (2007).

[28] Wouda, P., Schmid, M., Nieuwenhuys, B., and Varga, P. *Surface Science* **417**(2-3), 292 – 300 (1998).

[29] Schmid, M., Stadler, H., and Varga, P. *Phys. Rev. Lett.* **70**, 1441 (1993).

[30] Pleth Nielsen, L., Besenbacher, F., Stensgaard, I., Lægsgaard, E., Engdahl, C., Stoltze, P., Jacobsen, K. W., and Nørskov, J. K. *Phys. Rev. Lett.* **71**(5), 754–757 Aug (1993).

[31] Klitsner, T., Becker, R. S., and Vickers, J. S. *Phys. Rev. B* **41**, 3837–3840 Feb (1990).

[32] Li, N., Zinke-Allmang, M., and Iwasaki, H. *Surface Science* **554**(2-3), 253 – 261 (2004).

[33] Lauhon, L. J. and Ho, W. *Review of Scientific Instruments* **72**(1), 216–223 (2001).

[34] Cowley, J. M. *Phys. Rev.* **77**, 669 (1950).

[35] Vegard, L. *Z. Phys.* **5**, 17–26 (1921).

[36] Vechten, J. A. V. and Bergstresser, T. K. *Phys. Rev. B* **1**, 3351 (1970).

[37] Cercellier, H., Didiot, C., Fagot-Revurat, Y., Kierren, B., Moreau, L., Malterre, D., and Reinert, F. *Phys. Rev. B* **73**, 195413 (2006).

[38] Cole, R. J., Brooks, N. J., and Weightman, P. *Phys. Rev. B* **78**, 3777 (1997).

[39] Magri, R., Wei, S.-H., and Zunger, A. *Phys. Rev. B* **42**, 11388 (1990).

[40] Cole, R. J. and Weightman, P. *J. Elec. Spec. Rel. Phenom.* **178**, 112 (2010).

[41] Woodruff, D. P., editor. *The chemical physics of solid surfaces Volume 10: Surface alloys and alloy surfaces.* Elsevier, (2002).

[42] Kaminski, D., Poodt, P., Aret, E., Radenovic, N., and Vlieg, E. *Surface Science* **575**, 233–246 (2005).

[43] Aufray, B., Giordano, H., and Seidman, D. *Surface Science* **447**(1-3), 180 – 186 (2000).

[44] Dalmas, J., Oughaddou, H., Léandri, C., Gay, J.-M., Le Lay, G., Tréglia, G., Aufray, B., Bunk, O., and Johnson, R. L. *Phys. Rev. B* **72**, 155424 Oct (2005).

[45] Noakes, T. C. Q., Hutt, D. A., and McConville, C. F. *Surface Science* **307**, 101–106 (1994).

[46] Tersoff, J. *Phys. Rev. Lett.* **74**, 434 (1995).

[47] Ibach, H. *Surface Science Reports* **29**, 193–263 (1997).

[48] Massalski, T. B., editor. *Binary alloy phase diagrams.* ASM International, (1996).

[49] Kato, C., Aoki, Y., and Hirayama, H. *Phys. Rev. B* **82**, 165407 (2010).

[50] Wittich, G. *Rastertunnelmikroskopie und Rastertunnelspektroskopie bei tiefen Temperaturen: Entwicklung eines 1 K-Instruments und lokale Charakterisierung heterogener Metallsysteme.* PhD thesis, (2005).

[51] Gierz, I., Stadtmüller, B., Vuorinen, J., Lindroos, M., Meier, F., Dil, J. H., Kern, K., and Ast, C. R. *Phys. Rev. B* **81**(24), 245430 Jun (2010).

[52] Nolting, W. *Grundkurs Theoretische Physik 5/2.* Springer-Verlag Berling Heidelberg New York, (2006).

[53] Stein, D., Klitzing, K. v., and Weimann, G. *Phys. Rev. Lett.* **51**, 130–133 Jul (1983).

[54] Stormer, H. L., Schlesinger, Z., Chang, A., Tsui, D. C., Gossard, A. C., and Wiegmann, W. *Phys. Rev. Lett.* **51**, 126–129 Jul (1983).

[55] LaShell, S., McDougall, B. A., and Jensen, E. *Phys. Rev. Lett.* **77**, 3419–3422 Oct (1996).

[56] Petersen, L. and Hedegård, P. *Surface Science* **459**, 49–56 (2000).

[57] Premper, J., Trautmann, M., Henk, J., and Bruno, P. *Phys. Rev. B* **76**, 073310 Aug (2007).

[58] Cappelluti, E., Grimaldi, C., and Marsiglio, F. *Phys. Rev. B* **76**, 085334 Aug (2007).

[59] Hirayama, H., Aoki, Y., and Kato, C. *Phys. Rev. Lett.* **107**, 027204 Jul (2011).

[60] Mirhosseini, H., Ernst, A., Ostanin, S., and Henk, J. *Journal of Physics: Condensed Matter* **22**(38), 385501 (2010).

[61] Edwards, J. T. and Thouless, D. J. *J. Phys. C: Solid State Phys.* **5**, 807 (1972).

[62] Lee, P. A. and Ramakrishnan, T. V. *Rev. Mod. Phys.* **57**, 287 (1985).

[63] Lindelof, P. E., Norregaard, J., and Hanberg, J. *Physica Scripta.* **T14**, 17 (1986).

[64] Mott, N. F. *Phil. Mag.* **17**, 1259 (1968).

[65] Metropolis, N., Rosenbluth, A. W., Rosenbluth, M. N., Teller, A. H., and Teller, E. *Journal of Chemical Physics* **21**, 1087–1092 (1953).

[66] Fosdick, L. D. *Phys. Rev.* **116**, 565–573 Nov (1959).

[67] Assig, M. *Development of a Millikelvin Scanning Tunneling Microscope for Applications in Ultra High Vacuum and High Magnetic Fields.* PhD thesis, (2011).

[68] Ibach, H. *Physics of surfaces and interfaces.* Springer-Verlag Berling Heidelberg, (2006).

[69] Ast, C. R., Assig, M., Ast, A., and Kern, K. *Review of Scientific Instruments* **79**(9), 093704 (2008).

[70] Athenstaedt, W. and Leisch, M. *Applied Surface Science* **94**, 403 – 408 (1996).

[71] Assig, M., Koch, A., Stiepany, W., Straßer, C., Ast, A., Kern, K., and Ast, C. R. *Review of Scientific Instruments* **83**(3), 033701 March (2012).

[72] Musket, R., McLean, W., Colmenares, C., Makowiecki, D., and Siekhaus, W. *Applications of Surface Science* **10**(2), 143 – 207 (1982).

[73] Ibe, J. P., Bey, P. P., Brandow, S. L., Brizzolara, R. A., Burnham, N. A., DiLella, D. P., Lee, K. P., Marrian, C. R. K., and Colton, R. J. *Journal of Vacuum Science & Technology A: Vacuum, Surfaces, and Films* **8**(4), 3570–3575 (1990).

[74] Zhang, K. H. L., McLeod, I. M., Lu, Y. H., Dhanak, V. R., Matilainen, A., Lahti, M., Pussi, K., Egdell, R. G., Wang, X.-S., Wee, A. T. S., and Chen, W. *Phys. Rev. B* **83**(23), 235418 Jun (2011).

[75] Soares, E. A., Bittencourt, C., Nascimento, V. B., de Carvalho, V. E., de Castilho, C. M. C., McConville, C. F., de Carvalho, A. V., and Woodruff, D. P. *Phys. Rev. B* **61**, 13983–13987 May (2000).

[76] Oppo, S., Fiorentini, V., and Scheffler, M. *Phys. Rev. Lett.* **71**, 2437 (1993).

[77] Gerold, V. and Kern, J. *Acta metall.* **35**, 393–399 (1987).

[78] Hoster, H. E., Filonenko, E., Richter, B., and Behm, R. J. *Phys. Rev. B* **73**, 165413 Apr (2006).

[79] Slater, J. *Journal of Chemical Physics* **41**, 3199–3204 (1964).

[80] Bihlmayer, G., Blügel, S., and Chulkov, E. V. *Phys. Rev. B* **75**(19), 195414 May (2007).

[81] Noakes, T., Hutt, D., McConville, C., and Woodruff, D. *Surface Science* **372**, 117 – 131 (1997).

[82] Bergbreiter, A., Alves, O. B., and Hoster, H. E. *ChemPhysChem* **11**(7), 1505–1512 (2010).

[83] Moreschini, L., Bendounan, A., Gierz, I., Ast, C. R., Mirhosseini, H., Höchst, H., Kern, K., Henk, J., Ernst, A., Ostanin, S., Reinert, F., and Grioni, M. *Phys. Rev. B* **79**, 075424 Feb (2009).

[84] Anderson, E., Bai, Z., Bischof, C., Blackford, S., Demmel, J., Dongarra, J., Croz, J. D., Greenbaum, A., Hammarling, S., McKenney, A., and Sorensen, D. *http://www.netlib.org/lapack/lug/lapack_lug.html.*

[85] Wöll, C., Chiang, S., Wilson, R. J., and Lippel, P. H. *Phys. Rev. B* **39**, 7988–7991 Apr (1989).

[86] Chen, W., Madhavan, V., Jamneala, T., and Crommie, M. F. *Phys. Rev. Lett.* **80**, 1469–1472 Feb (1998).

[87] Bürgi, L., Brune, H., and Kern, K. *Phys. Rev. Lett.* **89**, 176801 Oct (2002).

[88] Moreschini, L., Bendounan, A., Bentmann, H., Assig, M., Kern, K., Reinert, F., Henk, J., Ast, C. R., and Grioni, M. *Phys. Rev. B* **80**, 035438 (2009).

[89] Pacilé, D., Ast, C. R., Papagno, M., Silva, C. D., Moreschini, L., Falub, M., Seitsonen, A. P., and Grioni, M. *Phys Rev. B* **73**, 245429 (2006).

[90] Lerner, I. *Physics Letters A* **133**, 253 – 259 (1988).

[91] Altshuler, B., Kravtsov, V., and Lerner, I. *Physics Letters A* **134**, 488 – 492 (1989).

[92] Richardella, A., Roushan, P., Mack, S., Zhou, B., Huse, D. A., Awschalom, D. D., and Yazdani, A. *Science* **327**, 665 (2010).

[93] Ast, C. R. and Gierz, I. *to be published* .

[94] Chen, C. J. *Introduction into Scanning Tunneling Microscopy.* Oxford University Press, (2008).

[95] Frantzeskakis, E., Pons, S., Crepaldi, A., Brune, H., Kern, K., and Grioni, M. *Phys. Rev. B* **84**, 245443 Dec (2011).

[96] Ast, C. R., Pacilé, D., Papagno, M., Gloor, T., Mila, F., Fedrigo, S., Wittich, G., Kern, K., Brune, H., and Grioni, M. *Phys. Rev. B* **73**(24), 245428 Jun (2006).

[97] Härtel, T., Strüber, U., and Küppers, J. *Thin Solid Films* **229**, 163 (1993).

[98] Bromann, K., Brune, H., Giovannini, M., and Kern, K. *Surf. Sci.* **388**, L1107 (1997).

[99] Schmiedeskamp, B., Kessler, B., Vogt, B., and Heinzmann, U. *Surf. Sci.* , 465 (1989).

[100] van der Vegt, H. A., van Pinxteren, H. M., Lohmeier, M., Vlieg, E., and Thornton, J. M. C. *Phys. Rev. Lett.* **68**, 3335–3338 Jun (1992).

[101] Vrijmoeth, J., van der Vegt, H. A., Meyer, J. A., Vlieg, E., and Behm, R. J. *Phys. Rev. Lett.* **72**, 3843 (1994).

[102] Carnal, D., Oden, P., Müller, U., Schmidt, E., and Siegenthaler, H. *Electrochimica Acta* **40**, 1223 – 1235 (1995).

[103] Cappelluti, E., Grimaldi, C., and Marsiglio, F. *Phys. Rev. Lett.* **98**, 167002 Apr (2007).

Acknowledgements

In these past years that I worked on this thesis, I got to know many people, to whom I would like to express my gratitude:

- **Prof. Klaus Kern** for giving me the opportunity to work as a PHD student under such marvelous conditions that can be found in a Max-Planck-Institute.

- My supervisor **Dr. Christian Ast** for his guidance and friendship during this time and the many things I learned from him.

- **Dr. Maximillian Assig**, who build the STM unit and did the first tests in a predecessor of this UHV-system.

- **Dr. Maurits Haverkort** for fruitful discussions and suggestions about Anderson localization.

- **Wolfgang Stiepany**, **Peter Andler** and **Andreas Koch** for their technical support.

- All members of the department of Prof. Kern, especially the past and present members of the Emmy-Noether-Research-Group for the nice time we had together in Stuttgart.
- Last, I want to thank my parents and my siblings, for without them I wouldn't be where I am now.